Dissertation

submitted to the

Combined Faculties for the Natural Science and for Mathematics

of the Ruperto–Carola University of Heidelberg, Germany

for the degree of

Doctor of Natural Sciences

presented by

Licenciada en Fisica:	Maria Eugenia Toimil Molares
born in:	Las Palmas de Gran Canaria, Spain

Oral examination: 18th December, 2001

Fabrication and characterisation of copper nanowires electrochemically deposited in etched ion-track membranes

Referees: Prof. Dr. R. Neumann

Prof. Dr. G.K. Wolf

Zuzammenfassung

Poly- und einkristalline Kupfer-Nanodraehte wurden durch elektrochemische Abscheidung in geaetzten Ionenspuren-Membranen hergestellt. Polycarbonat-Folien von 30 μm Dicke wurden am UNILAC (GSI, Darmstadt) mit Au^{197}- und Pb^{208}-Ionen mit einer Energie von 1-2 GeV und Fluenzen zwischen 1 und 10^9 i/cm^2 bestrahlt. Mit Hilfe der Aetztechnik wurde das von den Ionen modifizierte Material chemisch herausgeloest, und es wurden Membranen mit Porendurchmessern zwischen 30 nm und μm hergestellt. Diese Membranen dienten als sog. Templat fuer das Wachstum von Kupferdraehten. Elektrochemische Abscheidung von Kupfer in Poren mit groβen (einige Hundert nm) und kleinen (einige Zehn nm) Durchmessern wurde mit einer Zwei-Elektroden- Zelle systematisch untersucht. Das Ziel der Untersuchung war es, die optimalen Abscheidungsparameter (Spannung, Temperatur und Zusammensetzung des Elektrolyts) herauszufinden, um einkristalline Nadeln herzustellen. Die Morphologie und Kristallinitaet der Nadeln wurde unter Verwendung von Rasterelektronenmikroskopie, Transmissionselektronenmikroskopie und Roentgenbeugung untersucht. Nadeln, die bei hohen Temperaturen (50 °C) und niedrigen Ueberspannungen (unter 60 mV) abgeschieden wurden, sind einkristallin. Polykristalline Nadeln wurden bei Raumtemperatur oder bei hoeheren Ueberspannungen hergestellt. Typische Defekte wie z.B. Zwillinge oder Versetzungen wurden beobachtet. Zwei verschiedene Techniken wurden getestet, um einzelne Nanodraehte zu kontaktieren.

Abstract

Poly- and single-crystalline copper nanowires have been created by electrochemical deposition of copper in etched ion-track membranes. 30 μm thick polycarbonate foils were irradiated at the UNILAC (GSI, Darmstadt) with Au^{197} and Pb^{208} ions of kinetic energy 1-2 GeV with fluences between 1 and 10^9 i/cm^2. The latent tracks generated by the heavy ions were chemically etched providing membranes with cylindrical pores of diameters between 30 nm and μm. These membranes were used as templates for the growth of copper. Potentiostatic deposition of copper in pores with large (several hundred nm) and small (several ten nm) diameter pores have been investigated using a two-electrode electrochemical cell. We present the results of a systematic study aimed at determination of the optimal deposition parameters (overvoltage, temperature, and electrolyte solution) required for single-crystalline growth. The morphology and crystallinity of the copper nanowires were studied by means of scanning electron microscopy, transmission electron microscopy and x-ray diffraction. Thus, from our results we can affirm that nanowires deposited at high temperatures (50 °C) and overvoltages lower than 60 mV possess a single-crystalline structure. Polycrystalline wires were obtained from depositions at room temperature or at higher overvoltages. Typical defects of single-crystals as twins and slips were also observed. Two different techniques were tested to contact nanoneedles for electrical transport measurements.

Contents

Chapter 1

Introduction

During the last decades, the fast technological development, promoted mainly by the microtechnology industry, has led to a progressive miniaturisation of electronic devices. The production techniques employed in this field are well established and comprise optical or electron-beam lithography, metallisation, implantation, and etching. While nowadays, the resolution limit is in the sub-micrometer range, new structuring techniques have to be developed when nanometer dimensions are required [1, 2]. Such new methods must also be able to create micro- and nanostructures of higher aspect ratios required, for example, for devices combining mechanical and microelectronic components (MEMS) [3, 4].

A technique suitable for structuring materials with small lateral dimensions and high aspect ratios, is the combination of heavy ion irradiation and chemical etching [3]. Compared to the broadly applied lithographic methods, the ion technique has the advantage that each projectile creates an individual damage trail of a few nanometers in diameter. The length of the resulting ion track is determined by the ion energy and can reach several hundred μm. By chemical etching, tracks can be enlarged to pores of different sizes and extremely large aspect ratios (up to 10^4) [5]. Besides, many materials can be structured as, for example, polymers, dielectric crystals or glasses. In chapter 3, we describe the track etching technique and the production of polymeric membranes with cylindrical pores.

Ion track membranes can be replicated by electrochemically depositing different materials into their pores. This is the basic idea of the so-called template method [6, 7]. We applied this technique to fabricate large-area arrays of identical micro- and nanowires. Though the electrochemical deposition in different types of templates has been employed for many years [8, 9, 10], a systematic study of the deposition process in

submicrometer pores had not been performed until now. Our aim was, to determine the optimal conditions for a homogeneous growth and, in addition, to find the deposition parameters (overvoltage, temperature and electrolyte solution) required for growth of single-crystalline copper nanowires. Details of the electrochemical experiments are described in chapter 4.

The large interest in nanowires [11, 12, 13, 14, 15] is based on their promising applications, for instance, as interconnects in future generations of nanometer-scale electronics [16], as emitters in field emission arrays [17, 18], or as constituents of magnetic storage devices [19]. At the same time, they are considered to be excellent objects to study fundamental physical phenomena such as electron transport, including superconductivity [20] and magnetoresistance [21], electron emission [18], or quantum-size effects [22]. For our needle growth, we selected copper as material because of its importance in the microelectronic industry. In recent years, the submicro-technology has started to replace aluminium by copper in microelectronic devices. Copper has a lower resistivity than aluminium, leading to faster devices, and it is also less vulnerable to electromigration, a phenomenon that produces voids in the wires ultimately causing their break. Common approaches to copper metallisation include chemical vapour deposition (CVD), selective electroless deposition, sputtering and electroplating. Electrochemical deposition of copper is the leading technology, since it has low costs, is fast, and is suitable for deposition in trenches of small dimensions and/or high aspect ratios [23, 24, 4].

Many efforts aim at measuring physical properties of nanostructures and, in particular, of electrodeposited nanowires. Since phenomena such as electron transport, magnetoresistance, or optical reflectivity, depend very much on their crystallinity and their morphology [25], a detailed characterisation of the structures is required. Chapter 5 presents the results concerning the characterisation of nanowires deposited under different electrochemical conditions. We employed scanning electron microscopy, transmission electron microscopy and x-ray diffraction, to determine experimentally the influence of the deposition parameters on the morphology and crystallinity of the wires. This enables us to produce single- and polycrystalline copper nanowires in a reproducible way.

The production of low-ohmic contacts between nanostructures and macroscopic electronics is a demanding and difficult challenge. In the case of nanowires, carbon nanotubes or molecules, several attempts have been already reported using, for example, the metal coated tip of a scanning force microscope [12] or using a mechanically controllable break-junction [26]. However, these techniques, though appropriate for

measuring for a limited period of time, are not stable and do not provide the possibility of integrating the wires in any electronic circuit. Chapter 6 presents two alternative contacting methods: (i) the production of contacts by lithographic techniques and (ii) the electrodeposition of an individual wire in a single-pore membrane. In both cases, their suitability is demonstrated.

Finally, a summary of the most important results achieved in this work is presented in chapter 7.

Part I

Production of copper nanowires by the template method

Chapter 2

Principle of the template method

In this first part of the work, results on the fabrication of copper nanowires by means of the template method are presented. This method is considered one of the most suitable techniques for the creation of nanowires and nanostructures and, as its own name suggests, consists in synthesizing material in the pores of a template.

The two mostly used templates are porous alumina [27] and track-etched membranes [3]:
Porous alumina membranes are prepared by anodic oxidation of aluminium in an acidic solution. These membranes contain cylindrical holes with diameters between 5 and 200 nm. The pores are arranged in a hexagonal way and the pore densities vary between 10^9 pores/cm^2 and 10^{12} pores/cm^2.
Track-etched membranes are produced by irradiating foils with nuclear fission fragments or, as in our case, with high-energetic heavy ions. The latent tracks created in the material are subsequently chemically etched into pores. With the present irradiation set-up at GSI, the pore density can be varied between 1 and 10^{12} pores/cm^2, and the tracks can be distributed both stochastically or as an ordered pattern. A preset regular arrangement is possible at GSI by using a microprobe [28]. Irradiated materials used as membranes are commonly polymers as, e.g., polyimide (PI), polystyrene terephthalate (PET) or polycarbonate (PC), inorganic crystals as e.g. mica, and glass. Other employed templates such as nanochannel array glass [29], or self-assembled diblock copolymers [30] have been also reported in the literature.

In most of the cases, the material adopts the shape and the size of the hosting hole. In this way, pores of various shapes can be fabricated, e.g., cylindrical, conical, biconical and funnel-shaped, as it is shown schematically in figure 2.1 [31]. Besides, depending on the material, the chemistry of the pore wall, and the employed techniques, the

resulting cylinders may be solid or hollow, forming wires or tubes, respectively [32, 33].

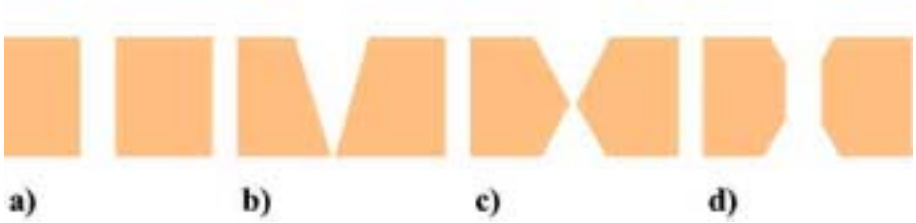

Figure 2.1: Schematic presentation of pores of various geometries, that can be created by etching heavy ion tracks in polymers. a) cylindrical, b) conical, c) biconical d) funnel-shaped.

Available techniques suitable for filling of the pores are electrochemical and electroless deposition, polymerisation reactions, sol-gel-template synthesis [34] and high-pressure injection of a melted material [35, 36]. Compared to the other techniques, electrochemical deposition is more suitable to create wires of high aspect ratio (length to diameter). If a conducting substrate is partly covered with a patterned insulating layer (in this case, the membrane), electrodeposition will take place only where the conductor is exposed, starting at the bottom of the pores and continuing until the pores are filled. By other techniques, the accumulation of material on the membrane surface, causes blocking of the pores. Additional advantages of the electrochemical methods are the avoidance of vacuum systems, its high flexibility and low costs, as well as its applicability to all substances suitable for deposition by electroplating.

The creation of nanowires by using the template method in combination with electrochemical deposition was pioneered by Possin. In 1970, he employed electrochemical deposition in etched fission tracks in mica to manufacture 40 nm diameter Sn wires [8]. Since then, experiments have been realised employing a large variety of materials and membranes. Metallic wires as well as tubes, e.g., copper [9, 37], silver [38], gold [39, 40, 41], platinum [42], nickel [43, 44], cobalt [43], iron [45], bismuth and cadmium [46] have been created either by electrochemical or by electroless deposition in both polymeric and porous alumina membranes, and studies about their optical [47, 48] and magnetic [43] properties have been reported. Multilayered structures formed by alternating layers of ferromagnetic/diamagnetic metals, e.g., Co/Cu, have been also produced to investigate their giant-magneto-resistive behaviour [49, 50].
Non-metallic materials as conductive polymers [51] and ionic crystals [52] have been also synthesized in the pores of commercially available polycarbonate membranes.

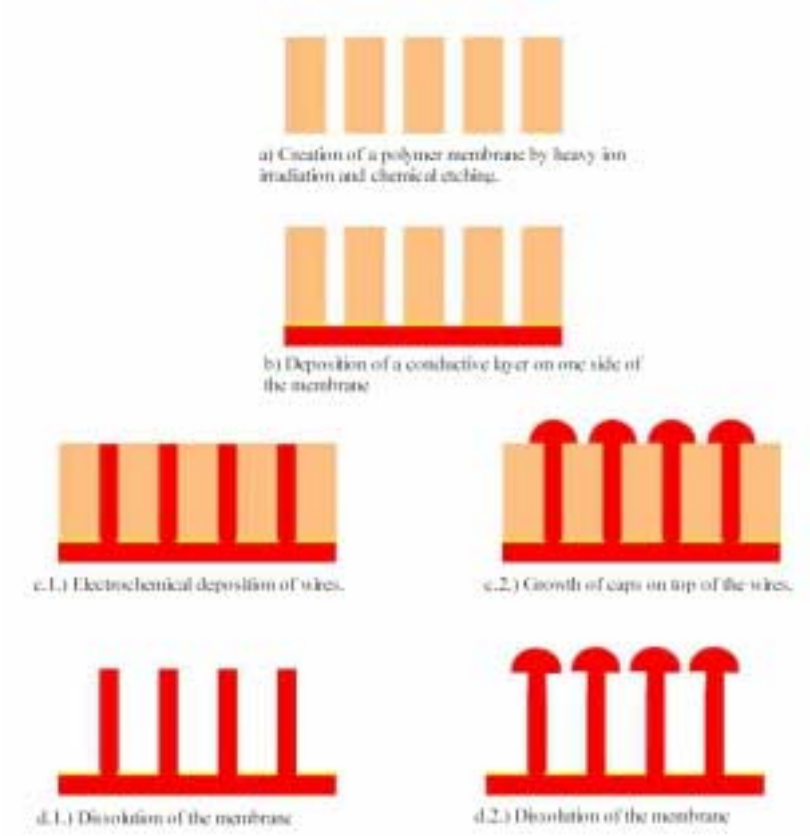

Figure 2.2: The template method.

A schematic of the template method, as employed in this work to create copper single- and polycrystalline nanowires in polycarbonate membranes, is illustrated in fig. 2.2. In a first step, the polymeric membrane is created by heavy-ion irradiation and chemical etching (2.2(a)). Then, a conductive layer is sputtered on one side of the membrane and reinforced by galvanostatic electroplating with copper (2.2(b)). This conductive layer provides a stable substrate for the growth of the wires and serves as cathode during the filling of the pores. The deposition process can be stopped during the growth of copper in the pores forming wires (2.2(c.1)), or it can be continued over a longer time forming then aditional caps on top of the wires (2.2(c.2)). For characterisation of the resulting structures by scanning electron microscopy (SEM) or by transmission electron microscopy (TEM), the polycarbonate is dissolved in a suitable solvent, e.g., dichloromethane (2.2(d)).

Chapter 3

Production of etched ion-track membranes

In recent years, etched ion-track membranes have been widely used as templates for the creation of nanowires and nanotubes. Two techniques are involved in the production of etch-track membranes, the formation of latent tracks by heavy-ion irradiation and the subsequent enlargement of the tracks to pores by chemical etching. Variation of the irradiation and etching conditions enables the production of suitable membranes with pores of different geometries, sizes and aspect ratios. Both techniques are presented in this chapter, and the experimental details of the production and characterisation of the membranes are discussed.

3.1 Formation of ion tracks in polymers

3.1.1 Heavy-ion irradiation

The irradiation facilities of GSI are schematically presented in Fig. 3.1. They consist of three main components: the universal linear accelerator UNILAC, the heavy-ion synchrotron SIS, and the experimental storage ring ESR.

All the polymer foils employed in this work were irradiated at the cave X0 located at the end of 120 m long UNILAC. Highly charged ions, from gaseous or from metallic elements, are produced in ion sources and accelerated by high-frequency fields to specific energies ranging from 1.4 MeV/nucleon to 11.4 MeV/nucleon, corresponding to 5 and 16 % of the velocity of light, respectively. Irradiations for this work were performed at this higher specific energy, i.e., 11.4 MeV/nucleon.

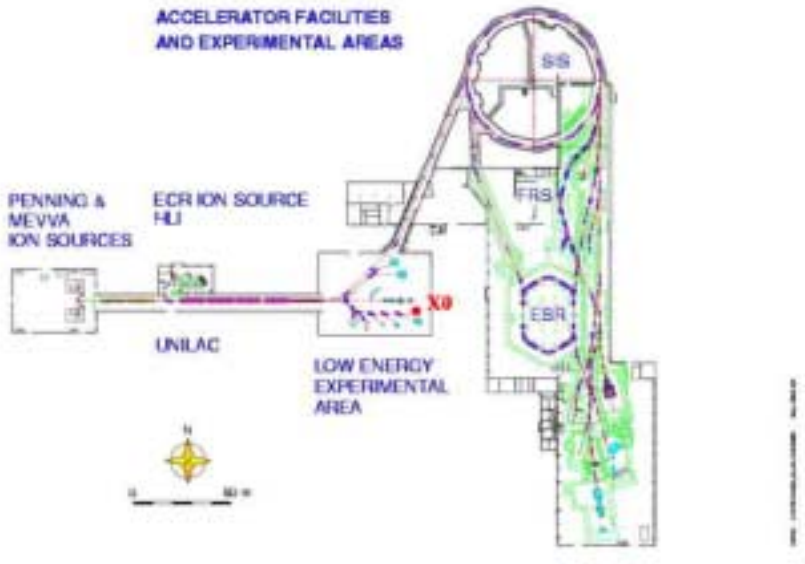

Figure 3.1: GSI accelerator facilities.

In addition, ions can be injected into the synchrotron SIS. In this latter case, the high-energy beams from the SIS (up to 1 GeV/nucleon) can finally be directed to the fragment separator FRS, to the ESR, or to the large target experimental hall, where mainly experiments in the fields of nuclear and atomic physics are performed.

3.1.2 Energy loss

When passing through matter, the ion loses energy by interaction with the electrons and atoms of the target. The energy loss per unit path length is called Stopping Power $\frac{\mathrm{dE}}{\mathrm{dx}}$. The main parameter governing the stopping power of ions in matter is the velocity of the ion, which determines the charge state of the projectile and the type of interaction between the ion and the target atoms [53, 5].
The total stopping power is usually expressed as the sum of the two contributions electronic stopping power and nuclear stopping power

$$\frac{dE}{dx} = \left(\frac{dE}{dx}\right)_{nuclear} + \left(\frac{dE}{dx}\right)_{electronic} \tag{3.1}$$

At high velocities, the energy transfer between ions and target electrons prevails (electronic stopping power). This latter interaction is responsible for the formation of etchable latent tracks. At low specific energies (i.e. low ion velocities), the energy of

the ion is transferred to the nuclei of the target atoms (nuclear stopping power). The qualitative relation of both energy losses as a function of the ion energy is presented in Fig. 3.2.

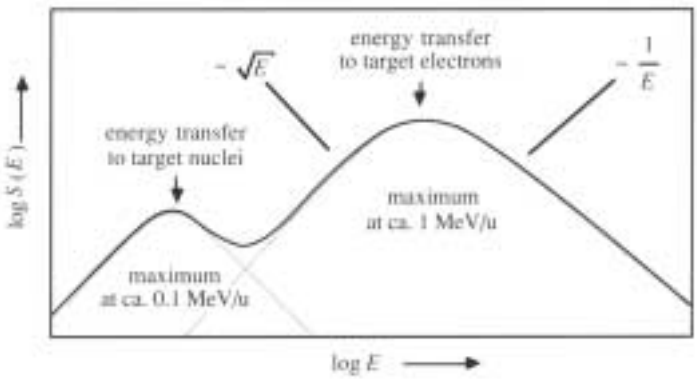

Figure 3.2: Energy loss.

Electronic energy loss At high velocities, the energy of the ions is transferred to the electrons of the target atoms. Target electrons are ejected along the ion trajectory and atoms are ionised. These electrons have a broad spectrum of kinetic energies and are able to produce further ionisations [5]. This electronic cascade (δ-electrons) spreads out rapidly in a radial range of up to 1 μm, carrying away energy and charge from the ion trajectory. In polymers, subsequent de-excitation processes can also lead to scissions of the long chain molecules and to free-radical production. The energy loss in this range of ion velocities is called electronic energy loss and is described by the Bethe-Bloch formula [54, 55]

$$\left(\frac{d\mathcal{E}}{dx}\right)_{electronic} = \frac{4\pi \cdot e^4 \cdot (Z^*)^2 \cdot Z^t \cdot N}{m_e \cdot v^2} \left[ln\left(\frac{2m_e \cdot c^2 \cdot \beta^2}{I}\right) - \beta^2 - \delta - U \right] \qquad (3.2)$$

Z^* being the effective charge of the ion, Z^t the nuclear charge of the target atoms, e the elementary charge of the electron, m_e the mass of the electron, N the number of target atoms per unit volume, v the ion velocity, I the average ionisation energy of the target atom, β the velocity of the ion relative to velocity of light c, and δ a relativistic correction term connected to the polarisability of the target, and U a correction term that takes into account that the electrons of the inner shells do not participate in the process.

The electronic energy loss is characterised by a maximum around 1 MeV/nucleon, the so-called Bragg peak. At higher ion energies (i.e., higher ion velocities), the interaction time between the ion and the target electrons diminishes, and therefore the transfer of energy is lower. At lower ion energies (i.e., lower ion velocities), the ion catches some electrons, thus diminishing its effective charge. In this way the energy loss decreases towards zero.

The positive effective charge Z^* of the ion, a consequence of its interaction on its way through the target, is given by

$$Z^* = Z \cdot \left(1 - e^{-\frac{130\beta}{Z^{\frac{2}{3}}}}\right) \tag{3.3}$$

β being the speed of the ion in units of the velocity of light and Z the atomic number.

Nuclear energy loss At low ion energies ($\leq$ 100 keV/nucleon), the interaction between projectile and atomic cores of the target is dominant. The elastic collisions produce direct displacements of atoms in the target, and thus vacancies and interstitials.

Penetration range The distance that the ion travels before coming to a full stop is called ion penetration range R

$$R = -\int_0^{E_o} \left(\frac{dE}{dx}\right)^{-1} dE \tag{3.4}$$

Penetration ranges can be calculated with different available codes as for example TRIM (TRansport of Ions in Matter). From calculations with this program we know that ions with an energy of 11.4 MeV/nucleon can travel 100 - 150 μm in polycarbonate before their energy reaches the nuclear stopping range.

3.1.3 The latent track

The latent track consists of a track core and a track halo. The track core has a diameter of less than 10 nm and is surrounded by the track halo, whose diameter is defined by the maximum range of the δ-electrons and may reach a size of up to 1000 nm.

The specific damage contained in the latent track depends on the kind of material. Amorphisation of crystalline targets, creation of defects, or outgasing processes, are some of the presently known irradiation effects. In the case of polymers, the track halo has a special relevance. Polymers are, together with for example alkali halides and biological objects, sensitive to radiolysis. For this reason, the δ-electrons may cause in these materials further direct damage in a similar way as under electron irradiation. In particular in polymers, chemically activated species may undergo secondary reactions on a time scale of milliseconds to hours. Reactions with light or the ambient air also take place within weeks or months.

The first ion tracks were observed in mica by Silk and Barnes [56] with a transmission electron microscope (TEM). Since then, tracks in different materials have been revealed with atomic resolution by employing different techniques. High resolution TEM images of latent tracks have been obtained for many different materials such as germanium sulfide [57], the high-Tc superconductor $Bi_2Sr_2CaCu_2O_8$ [58], and metals as Ti or $TiZr_2$ [59]. Scanning tunneling microscopy (STM) and atomic force microscopy (AFM), techniques invented by G. Binnig and H. Rohrer, and G. Binnig, Quate and Gerber, respectively, have provided high-resolution images of latent tracks in different materials as for example mica, graphite, and LiF at the sample surfaces and at surfaces exposed by cleavage [60]. Latent tracks in polymers have been also imaged by AFM [61].

Direct TEM observation of tracks in the case of polymers is very difficult, since the latent tracks easily fade away during observation due to their radiation sensitivity with respect to the electron beam. More information can be obtained by other techniques, which provide average information over many tracks. For example, ensembles of oriented tracks can be investigated by small-angle X-ray or neutron scattering. The results of these experiments describe the track as a cylindric region, whose radius and reduced density depend on the energy loss of the ions. Infra-red spectroscopy and electron spin resonance spectroscopy provide information about the chemical modification in the tracks and the creation and decay of radicals, respectively. Latent tracks in different polymers including polycarbonate (polymer used in this work) were investigated by both small-angle X-ray scattering and infra-red spectroscopy [62]. This work showed that many functional groups created by classical radiation degradation effects were also produced by heavy-ion irradiation. Besides, some special features, e.g., creation of alkines, were found exclusively in the case of heavy-ion irradiation. These alkines would form, together with larger defects, part of the track core of ~ 3 nm in diameter. The core is typically surrounded by a larger halo, which contains mainly classical defects.

3.2 Chemical etching of ion tracks

Under suitable conditions, the chemically modified material along the ion track of the polymer is dissolved at a faster rate than the non-irradiated bulk material. Consequently, two different etching rates are defined: a fast etch rate along the track, V_t, which depends on the damage density in the track, and the isotropic etch rate of the undamaged bulk material, V_b. The ratio between both rates is called selectivity S and depends on the irradiated material and on the etching conditions, namely, concentration and temperature of the etching solution

$$S = \frac{V_t}{V_b} \tag{3.5}$$

The etching process occurring along the ion track in a polymer is illustrated in Fig. 3.3.

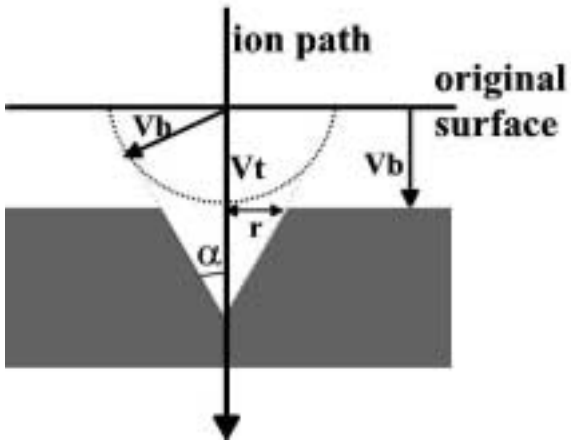

Figure 3.3: Schematic of the etching process.

The opening angle of the pore is given by

$$\alpha = \arcsin \frac{V_b}{V_t} \tag{3.6}$$

Thus, pores of different geometries can be produced by varying the selectivity: an extremely high ratio of $\frac{V_t}{V_b}$ leads to a cylindrical pore geometry ($\alpha \sim 0$), while $\frac{V_t}{V_b} \geq 2$ results in biconical-shaped pores ($\alpha > 0$). Conical pores have been also created by etching foils only from one single side [63, 64]. By performing several successive etchings as, e.g., creating a cylindrical pore and then producing a conical shape or vice versa, funnel-shaped pores and other pore geometries can be produced [31].

In general, the most suitable conditions for each individual etching procedure, concerning a specific material and aiming at certain pore characteristics as, for example, shape and size, have to be found in an empirical way, trying different sets of parameters. Etching conditions for different polymers can be found in [65].

Threshold for ion track formation A significant property of track etching is the etch-threshold, defined as the minimum energy loss required for the formation of an etchable track [5]. This etch-threshold depends on the composition of the irradiated material, and is explained by the model of extended defects. This model describes the morphology of the track as a function of the energy loss and of the spatial distribution of the deposited energy. Below the threshold, the damage in the track is not sufficient to allow selective etching. Slightly above the threshold, defects agglomerate to extended regions, but the defect density is not homogeneous. The tracks are etched in a discontinuous way and the resulting pores have consequently a wide pore size distribution [66]. Significantly above the threshold, a critical energy loss is surpassed throughout the full length of the ion trajectory and homogeneous etching is possible, all pores having about the same size.

Sensitization Etch properties depend on the environmental conditions before, during, and after irradiation. For example, oxygen present during or after irradiation, reacts with the defects, and stabilises the track. Additionally, the tracks can be sensitized by exposing the samples to UV-light before etching. It is presumed that the energy deposited by the UV light breaks additional chemical bonds along the track, thus increasing the track-etch rate V_t and the selectivity S (3.5) by a factor of up to 10 [5]. This is a convenient technique in order to create pores of small diameter and high aspect ratio. This treatment is also used, for example, to obtain uniform etching after irradiation with light ions.

Applications Etching is a complementary technique to study radiation effects in polymers. It allows us to obtain information about the sensitivity and registration properties of the material. Besides, the creation of ion-track membranes by chemical etching of latent tracks has opened a door to many technological applications in different fields as biotechnology, medicine or microtechnology. For example, ion-track membranes offer advantages over conventional separation filters (e.g. porous foams, bonded fibers) since ion-track membranes have few well defined parameters (pore length, pore diameter, and areal density of the tracks), which can be varied in a controllable manner over several orders of magnitude [67]. Membranes with switchable pores have been

created by grafting a responsive hydrogel onto the surface of a single-pore membrane. It was demonstrated that the flow of electrolyte through the modified pore can be controlled by varying the temperature or the pH-value [68]. Another example are the investigations on the deformability of red blood cells. This cell property was studied via the flow of individual cells through a pore of an ion-track membrane of slightly smaller size than the cell. An insufficient deformability of blood cells is an indication for certain diseases of the circulatory system [67].

3.3 Template Production

3.3.1 Material

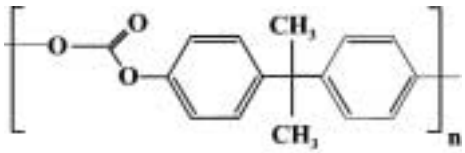

Figure 3.4: Structure of PC.

For this work, we employed 30 μm thick polycarbonate foils (Makrofol N) from the company Bayer Leverkusen. They possess high mechanical strength and toughness, and are resistant to break. Due to the production process, one of the sides is smooth and the other rough. We chose polycarbonate for several reasons: under suitable conditions, homogeneous cylindrical pores can be created. Furthermore,the material is very easy to dissolve (necessary to characterise the wires after their deposition), and to handle (not brittle as for instance mica). Polycarbonate has found applications in numerous fields as, e.g., optical data carriers (Audio CDs, CD-ROMs, CD-Rs, CD-RWs, DVDs), household goods, or automobiles.

3.3.2 Irradiation

The irradiations of all samples employed for this work were performed at the X0 beamline of the UNILAC, in the experimental hall (see Fig. 3.1).
The ion flux is determined by measuring the electric current passing through a 1 cm^2 aperture inserted into the beam with a Faraday cup. During sample irradiation, depending on the intended fluences, different detectors can be used, which are, in each case, calibrated by means of the current measured in the Faraday cup. For fluences

in the middle range (between 10^5 and 10^9 ions/cm^2), a three-foil detector is usually employed.
For irradiations with middle fluences below $\sim 10^7$ i/cm^2, an additional check of the calibration is possible. For this purpose, a glass plate is irradiated and etched a few seconds in HF. The fluence is checked by counting the etch pits under an optical microscope. In this way, both the validity of the calibration and the homogeneity of the fluence on the whole sample surface are controlled.
In this work, stacks of three polycarbonate foils (thickness 30 μm, diameter 50 mm) were irradiated with Au and Pb ions of 11.4 MeV/u at normal incidence. Under these conditions, the penetration range of the ions in the polycarbonate was larger than the total thickness of the stack (≤ 90 μm), and the energy loss of the ions in the polymer was well above the threshold required for homogeneous etching. Fluences between 10^6 and 10^9 i/cm^2 were applied.

3.3.3 Etching

For a given set of membrane parameters (e.g., membrane thickness and diameter, areal density, geometry and diameter of the pores), membrane thickness and diameter, and the pore density are fixed before and during irradiation, while pore diameter and geometry can be controlled by the etching conditions. In order to assign a correct dE/dx value to each foil in every irradiated stack, the foils were numbered, starting from the side reached first by the ions. To prepare identical membranes, only foils with the same stack position irradiated under the same conditions were used.
One of the foils was used for an etching test or calibration. We divided the foil in several pieces, and exposed them to the etchant over time periods of different length. In order to produce cylindrical pores, we employed a 6N NaOH solution, containing 10 Vol. % of methanol, at 50 or 60 °C. The solution was prepared with deionized water and p.a. grade chemicals from Merck company, and the temperature was kept constant with a thermostatic bath. After etching, the samples were carefully rinsed with deionised water. In the case of small pores double-distillated water was employed.
Two pieces of each sample were placed on a sample holder, a thin gold layer was sputtered on both surfaces, and the etched samples were characterised by scanning electron microscopy (SEM).
For each piece, the pore diameter and density were carefully determined. Since the resulting pore diameter increases linearly with the etching time, the obtained linear relation served as a reference to determine the etching time necessary to provide a certain pore diameter for the series of identical membranes, which were then etched

under the same conditions.
To produce a series of identical membranes, several polycarbonate foils were placed onto a sample holder. Four samples were fixed, perpendicular to the holder base, keeping a distance between adjacent samples of approximately 2 cm. This distribution of the samples in the bath, together with an effective stirring of the solution provided an homogeneous solvent concentration in the bath during the process. After careful rinsing, the membranes were ready for being used as templates.

3.4 Membrane characterisation

3.4.1 Etching rate, pore diameter and pore density

First, we present the results obtained for 30 μm thick polycarbonate foils irradiated with Au ions of 11.4 MeV/u energy. The applied fluence was $1.1 \pm 0.1 \cdot 10^6$ $ions/cm^2$. The pore diameter of the etched tracks measured at the membrane surface, d_p, is plotted as a function of the etching time in Fig. 3.5.

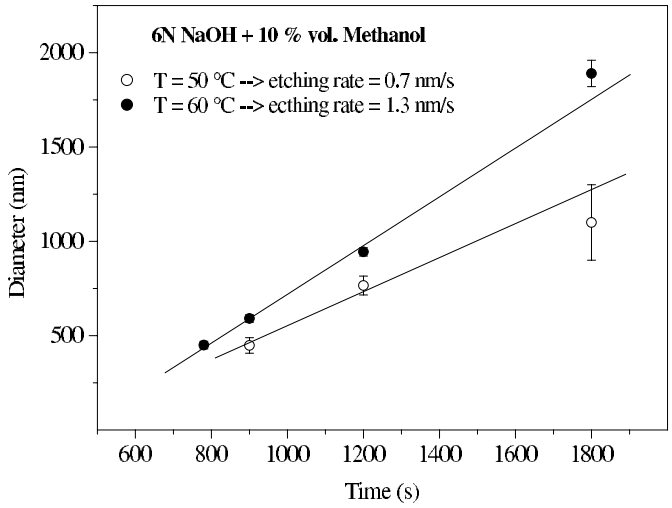

Figure 3.5: Pore diameter as a function of the etching time for 30 μm thick polycarbonate at 50 and 60 °C. The foils were irradiated with Au ions. The specific energy was 11.4 MeV/u, the fluence was $1.1 \cdot 10^6$i/cm^2.

As expected for an homogeneous etching, the diameter increases linearly with the etching time, the slope providing an etching rate of 1.3 nm/s. Mean pore diameters were obtained by calculating the arithmetic average of the diameters of 20 pores. The

error bars give the standard deviation of the mean value. Etching was performed at T = 50 or 60 °C. As typical for chemical reactions, an increase in temperature of 10 °C corresponds to roughly doubling the etching rate. In both cases, cylindrical pores were obtained, as will be discussed in section 3.4.3.

To obtain a more accurate value of the fluence applied during irradiation and to simultaneously check the homogeneity of the beam on the whole foil area, 10 SEM pictures similar to the one shown in Fig. 3.8 (right) were taken at different places. The 10 fluence values obtained from the pictures were averaged, resulting in a fluence of f $= 1.1 \pm 0.1 \cdot 10^6$ $ions/cm^2$.

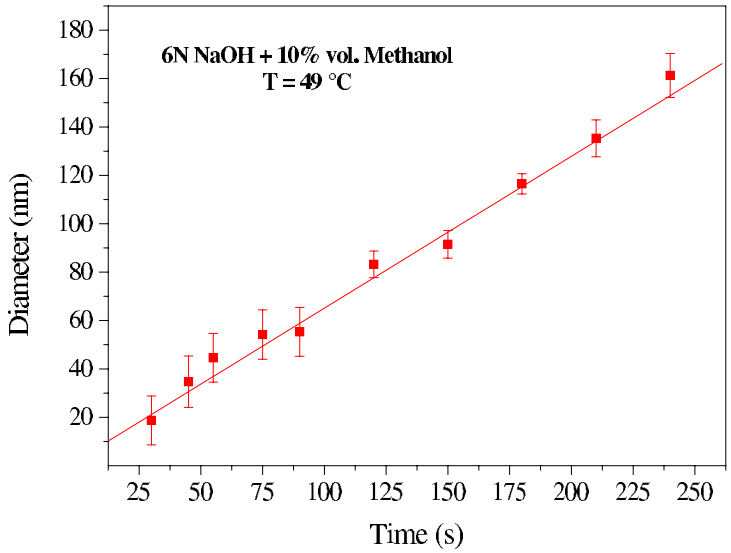

Figure 3.6: Pore diameter as a function of the etching time for a 30 μm thick polycarbonate sample. The foil stack was irradiated with Pb ions (11.4 MeV/u energy, $4.6 \cdot 10^8$ ions/cm^2).

In order to obtain pores of smaller radius r_p, shorter etching times were employed. Higher fluences were then applied in order to avoid too low porosity values. The porosity of the membrane is defined as:

$$P = f \cdot \pi \cdot {r_p}^2 \tag{3.7}$$

The correspondent etching curve for polycarbonate foils irradiated with Pb ions (11.4 MeV/u energy, f $= 4.6 \cdot 10^8 \pm 0.4 \cdot 10^8$ ions/cm^2) is presented in Fig. 3.6. Figure 3.7 shows two images of the polymer surface of a membrane with 45 nm pore diameter obtained after an etching time of 60 s.

Several series of 8 membranes each were etched during 12 and 15 min at T = 60 °C in order to obtain membranes with pore diameters 400 and 500 nm, respectively. With

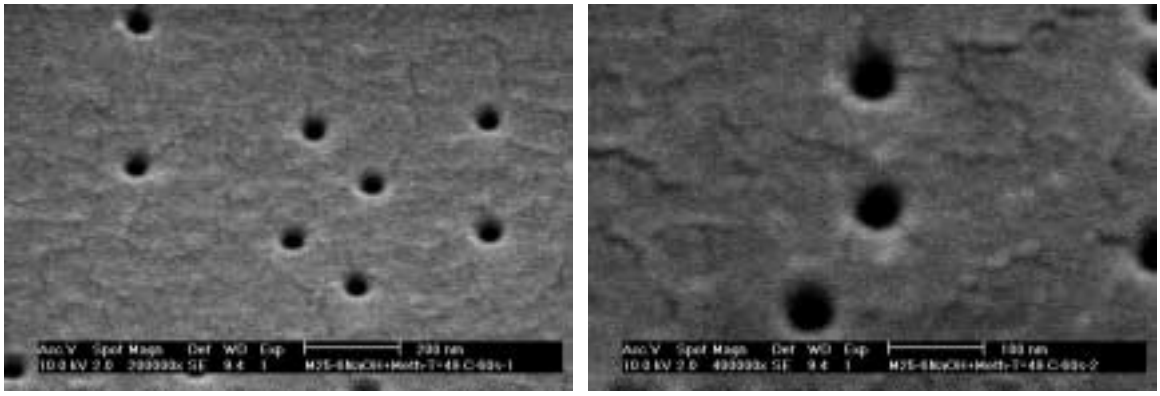

Figure 3.7: SEM images of the surface of a polymeric membrane, with mean pore diameter 45 nm at two different magnifications.

these membranes, experiments presented in section 4.3.2 were performed. Similarly, several foils were etched during 2 min at T = 50 °C, the resulting membranes being employed for experiments discussed in section 4.3.3. Other membranes (pore diameter 100 nm, 180 nm and 300 nm) were prepared under similar conditions.

3.4.2 Membrane surfaces

Fig. 3.8 shows the two sides of a polycarbonate membrane. The front side is smooth and the backside is rough. We can also distinguish them with the naked eye: the front side is bright and shiny while the back side is opaque. The different morphology arises during the fabrication process of the polymer foils and is relevant because the rough side possesses a much better adhesion to gold. For this reason, this backside will be used to create the cathode in the two-electrode electrochemical cell (section 4.2.1).

3.4.3 Geometry of the pores

To understand the electrodeposition process and to analyse the recorded curves, which are presented in the next chapter, one must know the current density j, under which the deposition took place:

$$j = \frac{i}{P \cdot A} = \frac{i}{S_{eff}} \tag{3.8}$$

i is the current flowing through the cell and S_{eff} denotes the effective surface, which is equal to the porosity of the membrane P (eq. 3.7) multiplied by the area A of the foil in contact with the electrolyte. We need therefore to know the diameter of the pore

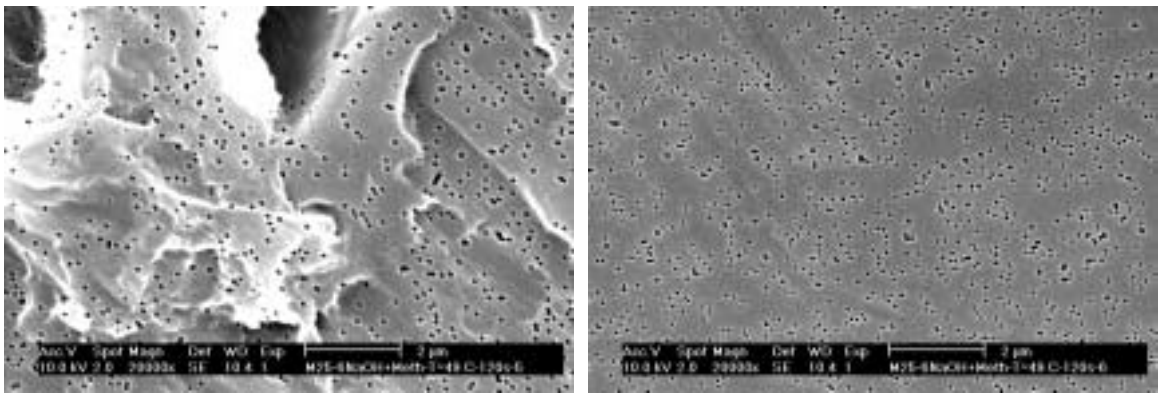

Figure 3.8: Rough (left) and smooth (right) side of the polycarbonate membrane after 2 minutes etching. (Pb, 11.4 MeV/u, f = $4.6 \cdot 10^8$ ions/cm^2. Etching was performed with 6N NaOH, adding a 10 vol. methanol, at T = 50 °C).

over its whole length, that means its geometry. Since the pores are replicated with metal, the best way of looking at their shapes and sizes is by measuring the dimensions of the resulting wires. The geometry of a wire with diameter 500 nm is depicted in Fig. 3.9. The wire is cylindrical with the exception of the last 3 μm at each end, where the diameter increases from 500 to 600 nm. For wires with diameters smaller than 100 nm and, consequently, with aspect ratios higher than 300, the geometry of the pores is biconical rather than cylindrical. With such high aspect ratios and small diameters, the diffusion of the etchant into the pores, as well as of the products from the pores back into the solution is more difficult. The resulting geometry is schematically presented in Fig. 3.10. With the data shown in Figs. 3.9 and 3.10, effective surfaces as well as volumes were calculated.

By replicating the pores we also observed that their inner surface is very smooth and homogeneous [69]. It should be also emphasized that needles with cigar-like shapes as discussed by several authors [44], have been never observed. Such an effect is linked either to special properties of the polymer [70] or caused by additives to the etchant solution (e.g. surfactants). In the latter case, the influence of the surfactant is eliminated by etching at high temperatures [71].

Concerning the characterisation of the membranes, X-ray analysis measurements, which will be shown in section 5.3.2.3, gave evidence for a good alignment of the pores normal to the membrane surface. This property of our templates can be of great im-

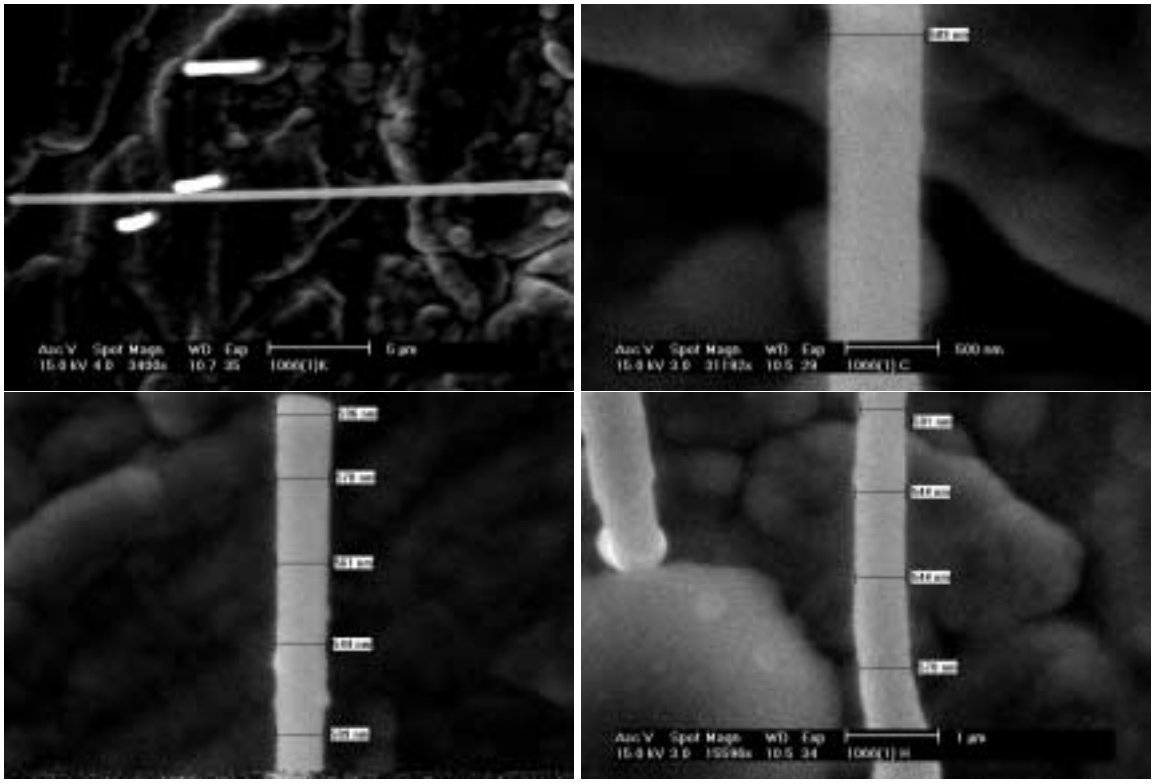

Figure 3.9: Picture of a wire revealing the geometry of the etched pore. Top left: view of a wire lying on the substrate, length 25 μm; top right: detail of a wire with diameter 509 nm; bottom left: upper end of the wire, the diameter increasing over the last 3 μm to 600 nm, (same scale-bar as bottom right); bottom right: basis of the wire exhibiting also a variation of the diameter.

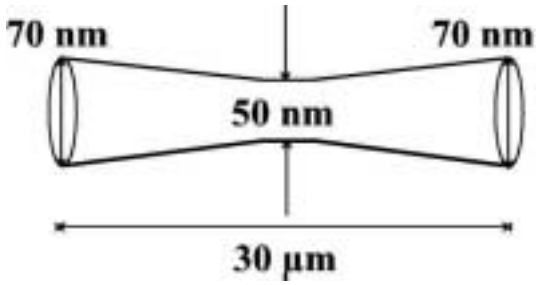

Figure 3.10: Schematic of the geometry of the small pores. The diameter varies between 70 nm at the surface and 50 nm at the center of the foil.

portance, if homogeneous needle growth is required. Problems due to large angular distributions with tilt angles of more than 30° in commercially available membranes have been reported by other authors [72].

Chapter 4

Electrodeposition of copper nanowires

In this chapter, we first explain the basic concepts necessary to understand the electrochemical deposition in membranes. Then, the results of a systematic study of the potentiostatic deposition of copper in pores with large (several hundred nm) and small (several ten nm) diameter pores are discussed. This study aimed at determining the optimal conditions for the homogeneous growth of large arrays of copper nanowires. Besides, in combination with the results presented in chapter 5, the optimal deposition parameters required for single-crystalline growth are determined.

4.1 Electrochemical metal deposition

4.1.1 Basic concepts

When a piece of metal is immersed into a solution containing its ions, the potential difference between both phases gives rise to an arrangement of the charges at the interface, that is known as electrochemical double layer. At this interface, some of the metal ions in the electrolyte can be adsorbed at the metal surface, retaining some charge of the ionic state and some ligands, usually water, and being subsequently incorporated into the growing lattice. This process constitutes a cathodic partial current density j_c. Simultaneously, lattice atoms partly coordinate with water molecules, move to the ionic side of the double layer as hydrated ions, and then enter the solution. This process produces an anodic or dissolution partial current j_a. If no external potential is applied, the so-called equilibrium potential E_{eq} is established after some time at the

interface electrode/electrolyte. At this potential, both partial current densities, anodic and cathodic have the same value, which is called exchange current density. The sum of both partial currents is zero in this case.

For a copper electrode in a copper sulfate bath, the process taking place is represented by:

$$\mathrm{Cu}^{+2} + 2\mathrm{e}^{-} \Longleftrightarrow \mathrm{Cu} \tag{4.1}$$

and the equilibrium potential at the copper electrode E_{eq}, which depends on the temperature and on the activity of the ions in the solution, is given by the Nernst equation:

$$E_{eq} = E^{\ominus} + \frac{RT}{zF} \cdot \ln \frac{a_{\mathrm{Me}^{z+}}}{a_{\mathrm{Me}}} \tag{4.2}$$

$E^{\ominus}$ being the standard potential, R the constant of the ideal gas, z the number of transferred electrons, F the Faraday constant, and $a_{\mathrm{Me}^{z+}}$ and a_{Me} the activities of the metal ions in the solution and metal atoms in the electrode, respectively. In the case of a pure metal electrode, $a_{\mathrm{Me}} = 1$. The activity of the ions in the solution represents the deviation from the ideal behaviour of an electrolytic solution. In practice, instead of activities, concentration values are introduced in (4.2).

E_{eq} of an electrode can not be directly measured, because there is no way to make an electrical connection to the solution phase without setting up another electrode with its potential. Consequently, electrode potentials are always measured against a reference electrode, whose well known potential should be established fast and reproducibly. When a potential E is applied to the electrode, a net current flows and the potential at the electrode reaches a value E different from E_{eq}. The shift in the potential is called overvoltage η, negative for cathodic reactions and positive for anodic reactions:

$$\text{cathodic}: \quad \eta_c = E_c - E_{eq} < 0 \tag{4.3}$$

$$\text{anodic}: \quad \eta_a = E_a - E_{eq} > 0 \tag{4.4}$$

So far, the description of the overvoltage has been restricted to a process occurring at one electrode/electrolyte interface. For electroplating in an electrochemical cell, we immersed two electrodes in the electrolyte. The cell potential measured between them when no current flows is called rest potential or open-circuit potential, $E_{o.c.}$. When they are connected to an external circuit, and a current flows through the cell, the cell potential is defined as

$$E = \eta_c - \eta_a + I \cdot R_s = E_c - E_a + I \cdot R_s \tag{4.5}$$

R_s being the resistance of the electrolyte solution and I the current flowing through the cell. The difference between the potential acquired during deposition and the open-circuit potential is called cell overvoltage

$$\eta = E - E_{o.c.} \tag{4.6}$$

The anode may serve, additionally, as reference electrode. This is possible if its area is much larger than that of the cathode, and therefore its overvoltage is small compared to that of the cathode.

Metal deposition can take place either galvanostatically or potentiostatically. In galvanostatic processes, the current flowing between anode and cathode is constant. In this case, the cathode potential and consequently the chemical reaction occurring at the electrode may vary, giving rise to undesirable reactions as for instance hydrogen evolution. In potentiostatic deposition, the potential between the cathode and a reference electrode is kept constant. In the case of a two-electrode cell, the potential between cathode and anode is fixed. In this way, the applied potential determines which reactions can take place, and the current density can vary with time. In both cases, Faraday's law specifies the charge Q required to deposit a certain mass of material. The deposited mass m is given by:

$$m = \frac{M}{zF} \cdot \int_0^t I \cdot dt = \frac{M}{zF} \cdot Q \tag{4.7}$$

M being the molar mass of the deposited metal, I the current passing through the cell during a certain time t, z the valence of the metal, and F the Faraday constant. The current flowing through the chemical cell I divided by the effective cathode surface S_{eff} is called current density j. The ratio of the actual deposited amount of metal to that given by Faraday's law is called current efficiency. As an example, if during copper deposition the current efficiency is 96 %, it means that 4 % of the current was employed in another reaction, which could be, e.g., hydrogen evolution. The references [73] and [74], for example, provide a more extended and detailed explanation of the concepts presented in this section.

4.1.2 Electrode overvoltage

The total reaction taking place at the interface electrode/electrolyte is formed by different reaction steps. They include e.g., the transport of electroactive species towards the electrode, the stripping of the hydration shell or complexing agents, the adsorption of the species and charge transfer at the electrode, as well as secundary chemical reactions, or the formation of new phases or crystallisation if the reduced species is a metal (e.g., Cu). If the reduced species is another ion (as e.g., in the case of $Fe^{3+} \longrightarrow Fe^{2+}$), the desorption of the products of the electrode reaction, the creation of a hydration shell or complex formation, and the transport of the products towards the bulk solution should be included.

When deposition is occurring at the cathode, at least one of these steps is delayed, slowing down the global process. Consequently, the electrode potential is shifted away from its equilibrium potential, and an overvoltage is produced. The overall reaction rate is determined by the slowest reaction step and, depending on which is slowest, charge transfer-, diffusion-, reaction-, and crystallisation overvoltage can be defined. In this section, a short description is given for each of them. Further information can be found in [75].

Charge transfer overvoltage Charge transfer overvoltage is established at the electrode when the process is delayed due to the finite velocity of the transfer of metal ions through the interface electrode-electrolyte. In this process, electrons are transferred from the conduction band of the metal electrode to an ion adsorbed at the electrode surface or to an ion in the electrolyte, and vice versa. The charge transfer rate depends on several factors as, for instance, the composition and concentration of the electrolyte and the electrode properties.

Diffusion overvoltage At the beginning of the deposition (t = 0), the Cu^{2+} ions are homogeneously distributed in the electrochemical cell. The concentration of metal ions at the cathode is exactly the concentration of ions in the bulk solution. Nevertheless, when the deposition starts, the concentration of ions at the cathode C_e decreases immediately. This change in concentration is in accordance with the Nernst equation 4.2. If the diffusion of the ions from the bulk solution to the electrode is the slowest step, a diffusion overvoltage is created.

Reaction overvoltage It occurs if besides the electrode reaction (reduction or oxidation) another chemical reaction takes place, slowing down the global process and

controlling its velocity.

Concentration overvoltage The diffusion and the reaction polarisation are related to the concentration of species at the interface. Both can be considered in a combined term called concentration polarisation.

Crystallisation overvoltage Electrocrystallisation is the process describing the build-up (deposition) or destruction (dissolution) of the crystal lattice at the electrode surface. In this case, parallel to the charge transfer, a matter transfer occurs. Crystallisation, in particular the diffusion of ad-atoms to favourable sites at the cathode and the integration of the adsorbed atom in the crystal structure, can also retard the total process. In this case, a crystallisation overvoltage is created.

Resistance overvoltage The flow of current through the electrolyte requires aditional voltage, which is called ohmic or resistance overvoltage.

4.1.3 Transport processes

So that electrodeposition takes place, the ions must be transported from the bulk solution to the electrode interface. If all other electrolytic reactions are fast enough, mass transport becomes the slowest step, limiting the reaction rate. The transport of ions in a solution occurs either because of a gradient in the ionic concentration (diffusion), due to the movement of ions in an electric field (migration) or by convection. The total current between anode and cathode is described as a sum of these three contributions.

Diffusion Diffusion refers to the movement of ions or neutral molecules due to a concentration gradient. When a potential is applied, depletion of Cu^{+2} ions takes place at the cathode surface. This depletion results in a movement of ions from the bulk solution towards the cathode surface. The concentration of ions at the cathode surface is given by the Nernst equation (4.2), and the contribution of the diffusion of ions to the total current density $j_{i,d}$ is given by the Fick's law:

$$j_{i,d} = -z_i F D_i \cdot \frac{\partial c_i}{\partial x} \tag{4.8}$$

D_i being the diffusion coefficient of the species in the solution and $\frac{\partial c_i}{\partial x}$ the concentration gradient. The region close to the electrode, in which the concentration of ions differs from the bulk concentration, is called diffusion layer. The thickness of this layer, δ_N, increases steadily with time, as the concentration profile in this region becomes smoother (Fig. 4.1). In practice, the expansion of the layer is limited by the natural convection, and a constant diffusion layer thickness is reached after some time. Nernst estimated the size of the layer by extrapolating the linear region close to the electrode until it reaches the bulk concentration. If convection (stirring) is present during deposition, the diffusion layer thickness decreases. The thickness of the diffusion layer depends also on the temperature.

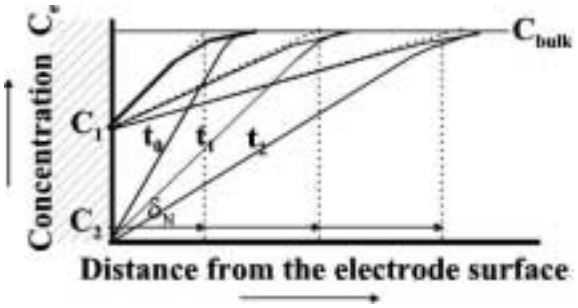

Figure 4.1: Concentration distribution at different times (t_0 before, and t_1, t_2 after applying any potential) for two different overvoltages η_1 and η_2.

Migration Ionic migration is the movement of ions in an electrolytic solution towards or from the electrode as a response to an electric field stablished in the bath. The current density due to migration of the species is given by:

$$j_{i,m} = -D_i c_i \frac{z_i^2 F^2}{RT} \cdot \frac{\partial \phi}{\partial x} \tag{4.9}$$

$\frac{\partial \phi}{\partial x}$ being the potential gradient in the solution. Ionic migration can only supply a fraction of the depositing metal. The remaining fraction will be provided at the electrode by diffusion. The contribution of migration to the measured current density can be minimized by adding an excess electrolyte, for example, sulfuric acid to a copper sulfate bath. Calculations have shown that aproximately 100 times the concentration of background electrolyte relative to that of the reactant is required to obtain a contribution of migration to the current of less than 1% [73].

Convection This form of transport corresponds to the movement of the species relative to the electrode. Movement can be produced by stratification in the bath (natural convection) or can be induced by agitation, e.g., stirring, bubbling air through the electrolyte or moving of the cathode (forced convection).

4.2 Experimental set-up

4.2.1 Deposition of a conductive layer as cathode

To start the growth of micro- and nanowires in a template, a conductive layer has to be deposited on one side of the membrane (Fig. 2.2 (b)). This layer provides a stable substrate for the homogeneous growth of the wires and serves as cathode in the above described electrochemical cell. For that purpose, the deposited layer must close the pores completely and has to be stable, in order to provide contact with the whole surface of the steel support, when placed onto the cell bottom. This was reached in two steps. First, we sputtered a thin gold layer (thickness $\sim$ 100 nm) with an *Edwards Sputter Coater S*150 *B* on one side of the membrane. Then, the film was reinforced by a thicker copper layer (thickness $\sim$ 20 μm). Dissolution of the thin Au layer during the electrochemical deposition of the thicker Cu layer was avoided by choosing as basis a metal nobler than copper, i.e. gold.
Good adhesion between the polymer foil and the metal layer was found to be essential to avoid that the electrolyte slipped between the conductive layer and the polymer surface during the electrodeposition of the wires. Therefore, several factors were taken into account. First, the deposition of the layer was performed on the rough side of the foil instead of on the shiny, achieving much better adhesion. Second, a suitable thickness of the gold layer had to be chosen. If it is too thin, the layer will not conduct, and it will not be possible to reinforce it with copper. If it is too thick, stress is induced and both surfaces, polymer and gold, will separate. Best results were obtained when the gold layer had a resistance of $\sim$ 30 Ω.
To reinforce the film, the membrane was introduced into the cell, with the gold layer facing the electrolyte. Copper was deposited galvanostatically at j = 50 mA/cm^2 and room temperature. Both a commercial Cupatierbad electrolyte (Riedel company) and a simple-salt electolyte formed by 238 g/l $CuSO_4 \cdot 5\ H_2O$ and 21 g/l sulfuric acid were employed. Under those conditions the resulting copper layer was polycrystalline and homogeneously covered the pore entrances. Moreover, the fact that the substrate and the wires consist of the same metal (copper), avoids possible stress and misfitting due to different lattice constants.

4.2.2 Instrumentation and electrochemical cell

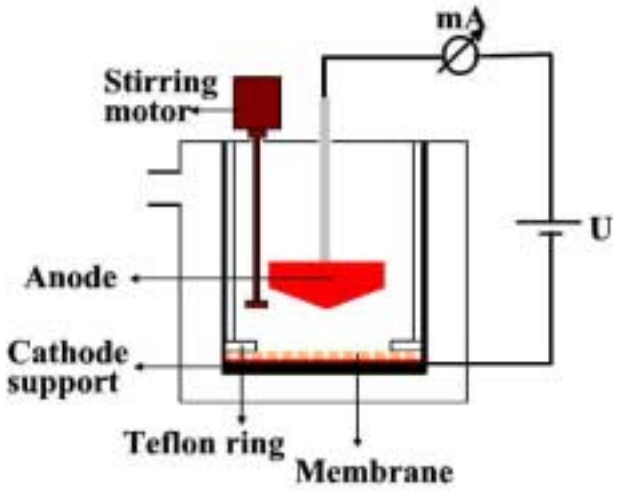

Figure 4.2: Schematic of the electrochemical cell employed in this work.

A schematic of the electrochemical cell employed in this work is shown in Fig. 4.2 [76]. It consists of two electrodes: a working electrode or cathode, and a counter electrode or anode. The conductive Cu layer deposited on one side of the membrane, acted as cathode, and a conical copper piece containing 0.04 % phosphorus functioned as anode. It is known that for flat anodes the metal is deposited preferentially at the outer border areas of the cathode [77]. This effect was avoided by using a conical anode, leading to a more homogeneous copper deposition over the whole cathode surface. The area of the anode is also much larger than the cathode effective area. For this reason, during the growth of the needles, the anode overvoltage is small compared to the cathode overvoltage, and the anode can be used at the same time as reference electrode.

The membrane is placed at the cell bottom, the pore openings facing towards the electrolyte. This cell bottom (made of stainless steel) also provides the contact between the cathode and the exterior circuit. This design allows one also to vary (if desired) the distance between anode and cathode, d_{a-c}. For all experiments presented here, the distance between the electrodes d_{a-c} was 1.5 cm. The area of the template membrane in contact with the electrolyte was limited by a teflon ring of area 8.04 or 3.8 cm^2 placed on top of the polymer foil. To calculate the effective surface, this area is multiplied by the porosity of the membrane (eq. 3.7). During deposition, the solution was mechanically stirred using a small motor. The cell was connected to a thermostatic bath to keep the temperature constant. The employed geometry influences positively the transport of Cu ions in the pores by convection and, in the case that bubbles are present in the

solution, it facilitates that they come out to the surface.
For potentiostatic experiments, the potential was supplied by a voltage source $Typ\ PN$ 300 *Grundig*. For galvanostatic experiments, we used a voltage source connected to a voltage/current converter. Both the potential applied to the cell and the current flowing between cathode and anode were measured with two digital multimeters $Type\ M4460A$ (*ConradElectronic*). During the measurements, the data (voltage and current) were continuously recorded by a standard PC.

4.2.3 Conditions for electrodeposition of Cu wires

For electrodeposition of copper micro- and nanowires, two different solutions were tested: a commercial electrolytic copper bath Cupatierbad, Riedel Company, and a simple-salt electrolyte that consisted of an aqueous solution containing 238 g/l $CuSO_4 \cdot 5\ H_2O$ and 21 g/l sulfuric acid. The commercial electrolyte consists of an acidic copper solution containing specific additives, for instance brightening substances. Usually, these special agents are adsorbed at the cathode surface, increasing the electrode polarisation and subsequently decreasing the grain size of the deposit.
A high concentration of $CuSO_4 \cdot 5\ H_2O$ was used to supply a sufficiently large number of ions inside the pores during deposition. The concentration of copper sulfate is not particularly critical except that for copper sulfate concentrations above 250 g/l, the cathode overvoltage increases slightly [78].
Sulfuric acid was added to increase the conductivity of the solution and to lower the cathode overvoltage. It is known that the cathode polarisation decreases by adding a small amount of sulfuric acid, reaching a minimum at around 30 g/l and increasing again at higher acid concentrations [78].
In order to avoid that the pores could be blocked by air bubbles, 40 ml of electrolyte were placed in an ultrasound bath and pumped out during some minutes before starting the deposition. Then, the solution was carefully passed into the cell to avoid new bubbles. This resulted in a considerable decrease of the air content in the solution. Before applying a potential, we waited until the open-circuit potential was reached. Both steps turned out to be crucial for the simultaneous growth of the wires.
Most electrodepositions were performed potentiostatically at temperatures between 25 and 70 °C. The applied voltages were low, avoiding side reactions such as hydrogen evolution.

4.3 Results and discussion

4.3.1 Current-vs-time curves

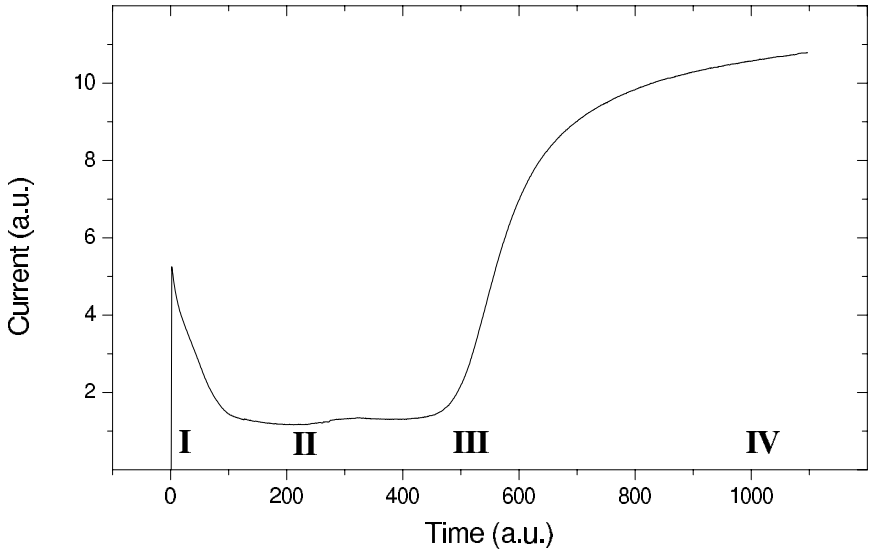

Figure 4.3: A typical current-vs-time curve for deposition of copper wires in poycarbonate templates.

A typical current-vs-electrodeposition time curve is shown in Fig. 4.3. Four different zones I to IV can be distinguished. When applying a potential, the current exhibits a peak (I) that is ascribed in part to the charge of the electrical double layer. Also the reduction of Cu^{2+} ions directly located at the cathode surface creates, during the first seconds, a concentration gradient that causes a flux of ions towards the cathode. In this process, the decrease of current indicates the formation of the diffusion layer. Stage II corresponds to the growth of the copper needles in the pores. The current remains nearly constant until the wires reach the polymer surface. Diffusion transport is presumably the rate-determining process. Then, caps start to grow on top of the needles, and due to the enlarged surface the current increases rapidly (III). The process continues with the macroscopic growth of copper on the whole surface (IV).
The process can be stopped during zone II or III, to obtain only wires or wires with caps, respectively.

4.3.2 Electrodeposition of copper in large pores

All measurements presented in this section were performed with membranes of similar characteristics. They were irradiated with Au ions of energy 11.4 MeV/u, applying a fluence of $9.7 \cdot 10^5 \pm 0.6 \cdot 10^5$ ions/cm^2. The samples employed in section 4.3.2.1 were simultaneously etched in a solution of 6N NaOH containing 10 Vol. % of methanol at 60 °C during 15 minutes. Under these conditions, the pore diameter was about 500 nm. For experiments performed at 70 and 30 °C (sections 4.3.2.2 and 4.3.2.3), the foils were also simultaneously introduced in the same etching solution during 12 min, the resulting pores being 400 nm in diameter.
For the measurements presented in this as well as in the next section, we have employed a simple salt electrolyte in order to avoid the influence of additives contained in the commercial electrolytes. These additives are usually not provided by the company and mostly used to obtain fine-grain bright deposits.
A detailed list of the data extracted from the current-vs-time curves are presented in Tables 4.1, 4.2 and 4.3. Note that current densities are given only for homogeneous depositions. If the deposition is inhomogeneous, or if the ratio between the experimental and theoretical charges is larger than 100 %, the current densities are not presented and, therefore, the measurements do not appear in the current-vs-voltage curve.

4.3.2.1 Electrodeposition at 50 °C

Fig. 4.4 shows the current-vs-time curves for different overvoltages (eq. 4.6) at T = 50 °C. All curves show the four zones described in section 4.3.1. It can be observed that the higher the overvoltage, the larger is the current density, and in agreement with Faraday's law, the shorter are the deposition times to reach stage III. In addition, the slope in region III is bigger for higher overvoltages.

Homogeneity and current efficiency The data extracted from the curves of Fig. 4.4 are presented in Table 4.1. $|\eta|$ is the overvoltage, at which the growth of the wires took place, d_p is the pore diameter considered for calculating the current density j, v_{eff} is the volume corresponding to the total number of deposited copper wires employed to calculate the total charge necessary to fill up all the pores, Q_{theo} is given by Faraday's law (4.7), Q_{exp} is the integral of the current-vs-time curves between the beginning of the deposition and the transition to zone III (increase of the current) and j is the current density, calculated by dividing the current in zone II by the total effective surface.

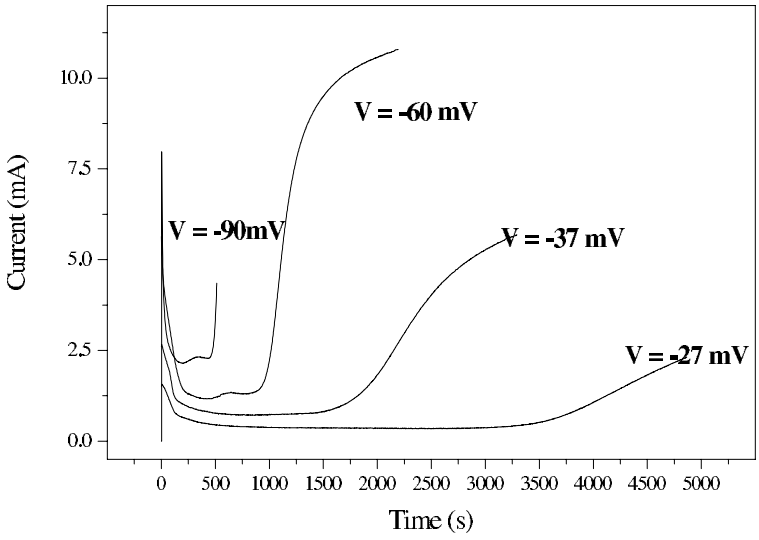

Figure 4.4: Current-vs-time curves for different overvoltages applied at 50 °C.

Probe	$\|\eta\|$ [mV]	d_p [nm]	v_{eff} cm^3	Q_{theo} [C]	Q_{exp} [C]	Q_{exp}/Q_{theo} [%]	j $[\frac{mA}{cm^2}]$
1064(1)	17.5	500	$4.9 \cdot 10^{-5}$	$1.33 \pm 0,4$	2.43	182	
1063(1)	27.0	500	$4.9 \cdot 10^{-5}$	1.33 ± 0.4	1.30	97	22.8
1065(1)	37.0	500	$4.9 \cdot 10^{-5}$	1.33 ± 0.4	1.44	105	45.6
1066(1)	60.0	500	$4.9 \cdot 10^{-5}$	1.33 ± 0.4	1.50	112	76.0
1069(1)	90,0	500	$4.9 \cdot 10^{-5}$	1.33 ± 0.4	1.30	97	117.0
1062(1)	110.0	500	$4.9 \cdot 10^{-5}$	1.33 ± 0.4	0.8	60	

Table 4.1: Data extracted from the current-vs-time curves measured at T = 50 °C for deposition of 500 nm diameter Cu wires.

To calculate the total volume to be filled with copper, v_{eff}, each pore was assumed to be a cylinder, except for both end sections, where a slight conical shape was included (see figure 3.9). The total pore volume times the density of copper ($8,9\ g/cm^2$) gives us the amount of copper, m_{eff}, that should be deposited if the copper grows homogeneously in all the pores. Then we calculated the theoretical charge Q_{theo} necessary to deposit m_{eff}. The error of Q_{theo} is basically given by the error of the effective volume to be filled, which in turn is determined by the uncertainties of membrane surface and

diameter, density, and length of the pores. We obtain:

$$\frac{\triangle(Q_{theo})}{Q_{theo}} = \frac{\triangle(v_{eff})}{v_{eff}} = 0.3 \tag{4.10}$$

The error of Q_{exp} is mainly determined by the time, at which we assumed the current starts increasing. It varies depending on the shape of the curve and the overvoltage, for example, the beginning of zone III being certainly better defined for depositions at higher overvoltages, since the transition is faster and the slope is higher. From the analysis of the curves, we consider

$$\frac{\triangle(Q_{exp})}{Q_{exp}} \leq 0.1 \tag{4.11}$$

Table 4.1 also includes the ratio of Q_{exp} to Q_{theo} for different applied voltages.
Note that for depositions at overvoltages between $|\eta|$= 27 and $|\eta|$= 90 mV, the theoretical and the experimental values are in good agreement within the experimental errors. This means that the deposition took place homogeneously, i.e., 100 % of the pores were filled, and that all the wires grew at the same rate. This also confirms the assumption of a 100 % current efficiency under these conditions.
For $|\eta|$ = 110 mV and certainly also for higher overvoltages, the ratio Q_{exp}/Q_{exp} decreases. Since the current increase occurs as soon as the first wires reach the pore surface, a lower ratio indicates that the growth is inhomogeneous at high deposition rates. We assume that the growth rate varies, and the wires do not reach the membrane surface simultaneously. As a result, when the process is stopped after the current increase, only part of the pores are filled. A similar effect was discussed in [79].
For $|\eta|$ = 17.5 mV, Q_{exp} is higher than the theoretical value Q_{theo}. This could be due to a leakage in the cell, which seems rather unlikely because the experimental set-up is identical for all the measurements, and moreover we did not observe any copper deposition at other places rather than in the pores. More plausible seems the possibility that, at low overvoltages, a parallel reaction occurs. It is well known that the reduction of Cu^{+2} ions takes place in two steps, namely $Cu^{+2} + e^- \Longrightarrow Cu^{+1}$ and $Cu^{+1} + e^- \Longrightarrow Cu$ [73]. At low overvoltages, the concentration of Cu^{+1} ions in the solution may be higher, and part of the Cu^{+1} ions can be oxidised by the air contained in the electrolyte, thereby producing again Cu^{+2} ions [80]. This process consumes current but does not lead to any deposit. Only when Cu^{+1} ions are further reduced to Cu, copper growth takes place. Besides, the Cu^{+2} and Cu^{+1} concentrations could be different for each individual pore, explaining the observed differences in growth rate for different wires.

SEM images of the wires supported this assumption. While an overvoltage of $|\eta|$ = 37 mV produces needles of identical height (Fig. 4.5 (left)), the length variation for $|\eta|$

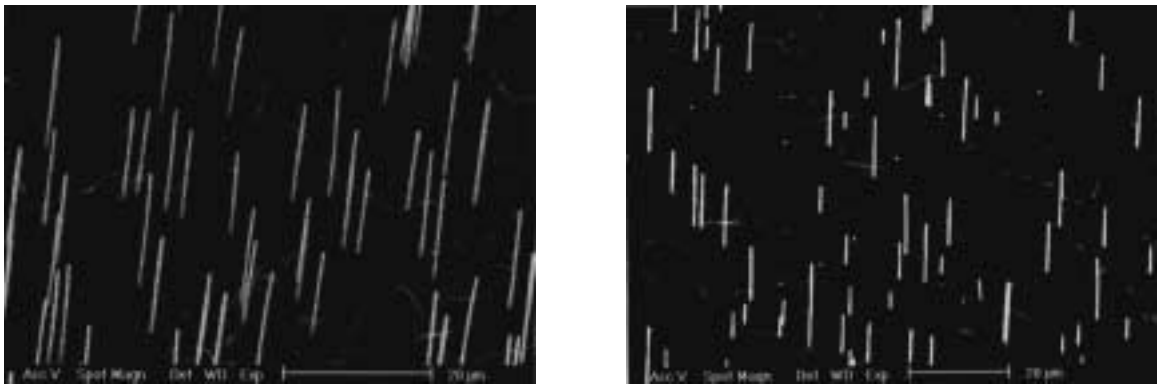

Figure 4.5: SEM images of Cu wires with a diameter of 500 nm. The left side shows homogeneous wire growth at $/\eta/ = 37$ mV; on the right side, the wires deposited at $/\eta/ = 17{,}5$ mV have different heights and are not filling the pores completely inspite of Q_{exp}/Q_{theo}= 182 %.

= 17.5 mV is enormous, although a large amount of charge was recorded during the deposition. This is an indication that a second reaction took place during this time.

Current density In Fig. 4.6, the current density for the homogeneous wire growth (region II) is plotted as a function of the overvoltage (27 mV $\leq |\eta| \leq$ 90 mV). As discussed above, the deposition was homogeneous in this voltage range. Moreover, we consider this range as suitable for the studies on the growth of single-crystals (this will be discussed in the next chapter).

We assume that, after creation of the diffusion layer in the first seconds, the transport of Cu ions towards the cathode becomes slower than the charge-transfer reaction, thus controlling the rate at which the whole process takes place (see section 4.1.2). This means that the deposition process in region II is diffusion controlled. The increase of current in Fig. 4.6 assures that, at the applied overvoltages, the process is not in the diffusion limited region, but still below. This means that the concentration of ions at the cathode decreases from the concentration in the bulk when applying a voltage to the cathode, but is not zero. This is important, since the quality of the deposits is known to decrease dramatically when the current reaches its limiting value [81].

For the concentrations of $CuSO_4$ and H_2SO_4 employed here, we can make a rough calculation to which extent a migration process contributes at room temperature to the total measured current. Considering $\triangle$c = c_{CuSO_4} = 0.95 mol/l, and $\triangle$x = $\delta_N \approx$ 0.01 cm, we obtain $\frac{\partial c_i}{\partial x} \approx 0.095$ mol/cm^4. The potential gradient can be calculated

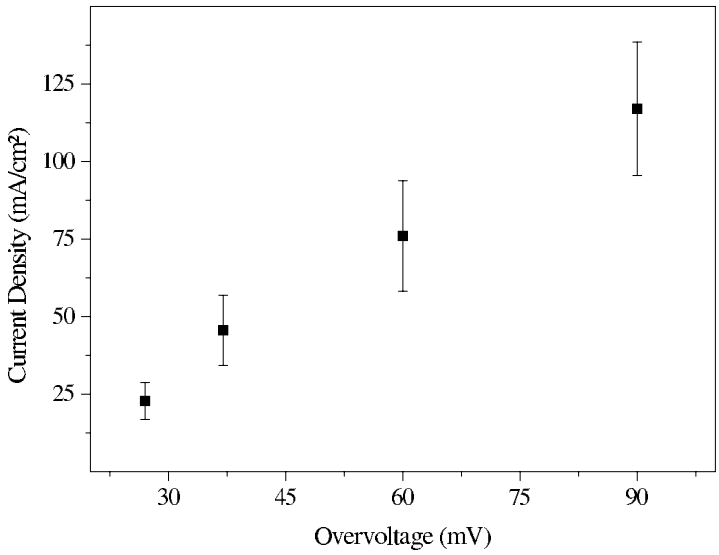

Figure 4.6: Current density as a function of the overvoltage for depositions at T = 50 °C.

from $|j|/\sigma$. Thus, as an example, for a current density $|j| = 50$ mA/cm^2, and $\sigma \approx 0.1\ \Omega^{-1}cm^{-1}$ (taken from [82] for this electrolyte concentration), $\frac{\partial\phi}{\partial x} \approx 0.5$ V/cm. Substituting the correspondent values in equations 4.8 and 4.9, a ratio $\frac{j_{migr}}{j_{migr}+j_{diff}} \sim 36$ % reveals a strong influence of the migration in the whole process.

It is known that the interplay of migration and electrodeposition in any electrochemical reaction gives rise to complex physical transport processes which are, generally, hard to interpret [83]. For example, a charge transfer process occurring at any electrode surface changes the local concentration of ionic species of the electrode and results in a change of the electric potential in the solution, thus altering also the electric field near the electrode, $(\frac{\partial\phi}{\partial x})$. This, in turn, causes a change in the migration contribution (4.9), and the rate of mass transport makes the interpretation of experimental data very difficult.

With the electrolyte concentrations employed here, the measured current should be the sum of three different contributions: charge transfer, diffusion and migration. The conditions chosen for the creation of single-crystalline wires provide a complicated scenario for the study of the kinetic of the process. Though different authors have tried to model the diffusion processes to ultra-microelectrodes (electrodes with, at least, one dimension smaller than 1 μm) [84, 85], they always assume simplified deposition conditions as., e.g., the total neglect of migration, or the absence of forced convection (stirring). To compare quantitatively these theories with electrodeposition in ion-track

membranes, the deposition parameters would have to be changed in order to minimize the contribution of migration transport. Besides, a third electrode, functioning as a reference electrode, would have to be introduced in the cell, to be able to control the cathode overvoltage individually. A comparison with the existing theories is made, and a model for the kinetic of the electrodeposition of copper in 500 nm pores has been presented in [79].

4.3.2.2 Electrodeposition at 70 °C

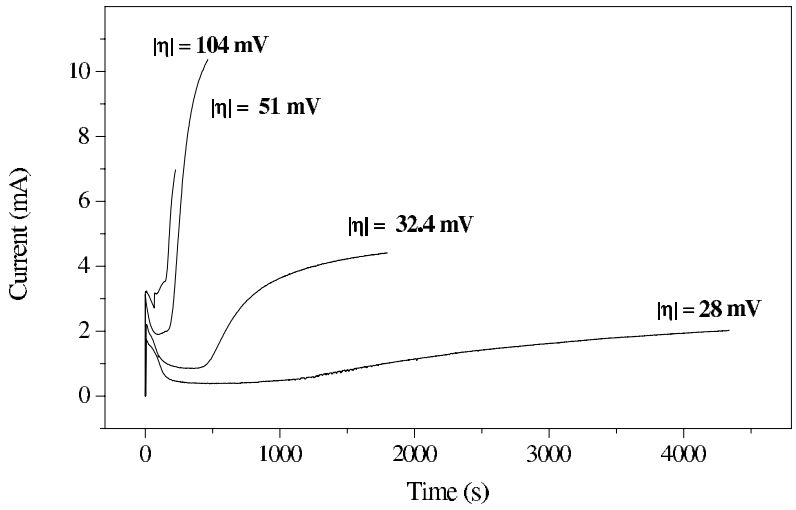

Figure 4.7: Current-vs-time curves for different overvoltages applied at 70 °C.

Homogeneity and current efficiency Figure 4.7 shows the current-vs-time curves for the depositions performed at T = 70 °C. The corresponding data are presented in Table 4.2. The same error calculations as in 4.3.2.1 have been performed, resulting in $\frac{\triangle(Q_(theo))}{Q_(theo)} = 0.3$ and $\frac{\triangle(Q_(exp))}{Q_(exp)} \leq 0.1$. At T = 70 °C the experimental and the theoretical charge coincide within the experimental errors for depositions at voltages between $|\eta|$ = 28 and $|\eta|$ = 104 mV. Nevertheless, the charges that were measured differ for the different experiments, varying between 57 and 86 %, while at 50 °C (Table 4.1) the charges were very similar for all samples. This may point to nonhomogeneities related to effects appearing at 70 °C. A possible reason is that part of the air dissolved in the electrolyte at room temperature, is released at this temperature and blocks some of the pores. This may occur because the ultrasonic degasing treatment of the electrolyte was performed before starting the deposition at room temperature. When heating up the electrolyte the remaining air may outgas and block some of the pores.

Probe	$\|\eta\|$ [mV]	d_p [nm]	v_{eff} cm^3	Q_{theo} [C]	Q_{exp} [C]	Q_{exp}/Q_{theo} [%]	j $[\frac{mA}{cm^2}]$
1071(1)	28	400	$3.0 \cdot 10^{-5}$	0.7 ± 0.3	0.54	68	39
1078(1)	32.4	400	$3.0 \cdot 10^{-5}$	0.7 ± 0.3	0.6	86	87
1077(1)	51.0	400	$3.0 \cdot 10^{-5}$	0.7 ± 0.3	0.4	57	193
1059(2)	104.0	400	$3.0 \cdot 10^{-5}$	0.7 ± 0.3	0.5	71	
1073(1)	263.0	400	$3.0 \cdot 10^{-5}$	0.7 ± 0.3	0.34	48	

Table 4.2: Data extracted from the current-vs-time curves measured at T = 70 °C for deposition of 400 nm wires

Again at higher overvoltages ($|\eta| \geq 100$ mV), a nonhomogeneous filling of the pores is indicated by a lower Q_{exp}/Q_{theo} ratio. At these overvoltages, experimental and theoretical charge do not coincide within the experimental errors.

Current density In Fig. 4.8, the current density is plotted as a function of the overvoltage. As in Fig. 4.6, the current density increases with the overvoltage in the voltage range considered here. The same explanations as for 50 °C are valid here.

4.3.2.3 Electrodeposition at 30 °C

The data extracted from the current-vs-time curves measured at T = 30 °C are presented in Table 4.3.

Probe	$\|\eta\|$ [mV]	d_p [nm]	v_{eff} cm^3	Q_{theo} [C]	Q_{exp} [C]	Q_{exp}/Q_{theo} [%]
1075(1)	22	400	$3.0 \cdot 10^{-5}$	0.7 ± 0.3	2	288
1073(2)	40	400	$3.0 \cdot 10^{-5}$	0.7 ± 0.3	5.1	728
1075(1)	56	400	$3.0 \cdot 10^{-5}$	0.7 ± 0.3	1.9	271
1078(2)	110	400	$3.0 \cdot 10^{-5}$	0.7 ± 0.3	0.65	93

Table 4.3: Data extracted from the current-vs-time curves measured at T = 30 °C for the deposition of 400 nm diameter wires.

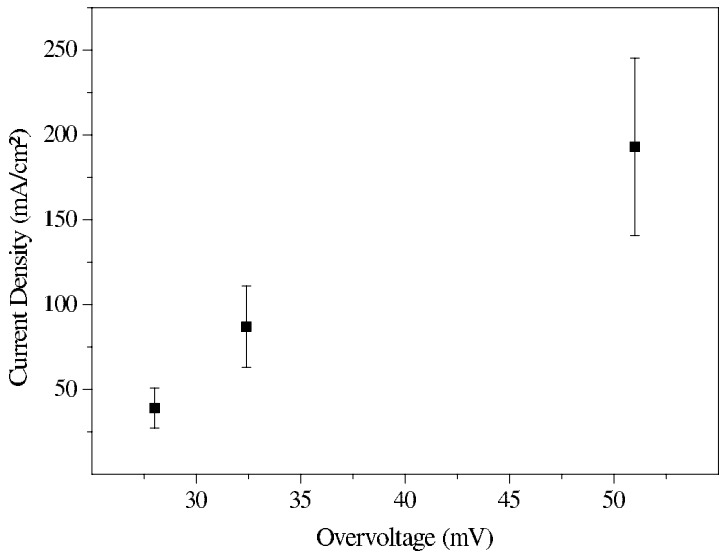

Figure 4.8: Current density as a function of the overvoltage for depositions at 70 °C.

For depositions performed at $|\eta| \leq 110$ mV, the ratio $Q_{exp}/Q_{theo} \gg 100$. This suggests that, as happened for $|\eta| = 17{,}5$ mV at T = 50 °C, the voltage applied was not high enough to allow an effective deposition of Cu. At T = 30 °C, this observation is made for a larger voltage range, namely up to at least $|\eta| = 60$ mV. The Nernst equation (4.2) gives the functional relation between the equilibrium potential of the cathode $E_{c,eq}$ and the temperature T. It shows that the higher the temperature, the larger is this $E_{c,eq}$, and consequently the lower is the cathode overvoltage η_c (eq. 4.3). This means that for a certain current I to flow through the cell, higher voltages are required at lower temperatures. This is the reason why at T = 30 °C only the experiments performed at $|\eta| \geq 110$ mV lead to homogeneous wire growth.

4.3.3 Electrodeposition of copper in small pores at 50 °C

Electrodepositions were also performed in membranes with a mean pore diameter smaller than 500 nm, namely 300, 180, 110, 80, 50, and 30 nm. Here we present a series of current-vs-time curves obtained for membranes irradiated with Pb ions, with an energy of 11.4 MeV/u. Their thickness is 30 μm, the pore density is $(5.8 \pm 0.4) \cdot 10^8$ cm^{-2}. The etching was performed in 6N NaOH at 50 °C. The resulting pores have a diameter of about 50 nm. Their geometry, studied by SEM, is schematically drawn in Fig. 3.10.

Homogeneity After the experiments performed with membranes of larger pores, we considered T = 50 °C the optimal temperature for the depositions regarding both an homogeneous growth of the wires and the quality of the resulting wires (discussed in the next chapter). Therefore, all depositions in small pores were performed at this temperature. The current-vs-time curves for 50 nm diameter pores and the corresponding data are shown in Fig. 4.9 and Table 4.4, respectively.

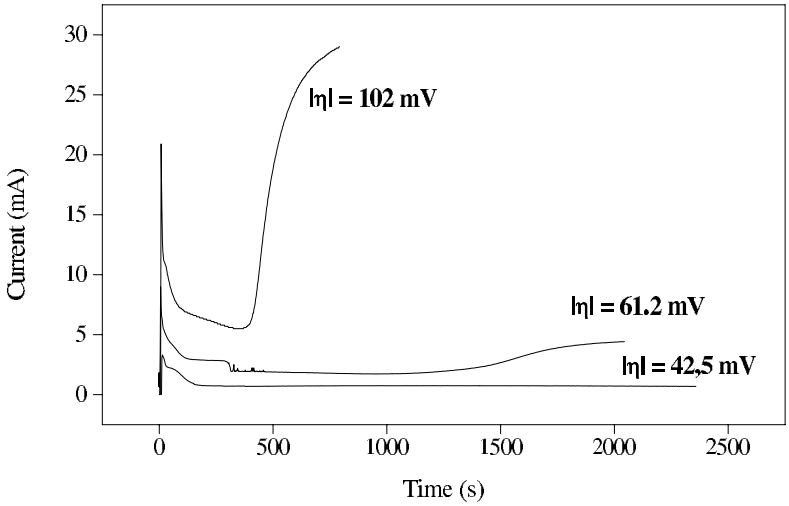

Figure 4.9: Current-vs-time curves for deposition in 50 nm diameter pores at different overvoltages applied at 50 °C.

Probe	$\|\eta\|$ [mV]	d_p [nm]	v_{eff} cm^3	Q_{theo} [C]	Q_{exp} [C]	Q_{exp}/Q_{theo} [%]	j $[\frac{mA}{cm^2}]$
95(3)	42,5	70-50	$1.6 \cdot 10^{-4}$	4.3 ± 0.3	2.7	63	19.0
95(1)	45.0	70-50	$1.6 \cdot 10^{-4}$	4.3 ± 0.3	2.6	60	
96(3)	61.2	70-50	$1.6 \cdot 10^{-4}$	4.3 ± 0.3	2.6	60	42.5
98(3)	102.0	70-50	$1.6 \cdot 10^{-4}$	4.3 ± 0.3	2.6	60	137.5
yyy*	110.0	70-50	$1.6 \cdot 10^{-4}$	4.3 ± 0.3	3.2	74	18.7

Table 4.4: Data extracted from the current-vs-time curves measured at T = 50 °C for deposition of 50 nm diameter wires. * Deposition at room temperature.

During these experiments, we observed that the time needed for the potential to reach the open-circuit potential of -9,5 mV was significantly larger than in the case of 500 nm diameter pores. This effect is most likely related to the difficulty of wetting such small pores [44].

Note that deposition *yyy* took place at room temperature at overvoltages above 100 mV in order to avoid a low deposition efficiency due to parallel reactions, as explained for larger pores in the preceding section. The resulting deposits will be commented in section 5.3.2.3. For all experiments at T = 50 °C, Q_{exp}/Q_{theo} = 60 %, indicating good reproducibility of the filling process in the potential range chosen. Since the error calculated for Q_{theo} contains already uncertainties in pore diameter, pore length, membrane surface and fluence, we assume that only 60% of the pores are filled, while 40% remain empty. This is in agreement with other groups, which reported a decrease in filling effectivity for the smallest pores [44]. The current efficiency at T = 50 °C is assumed to be 100%, the value obtained for deposition in 500 nm pores. The current density as a function of the voltage is presented in figure 4.10.

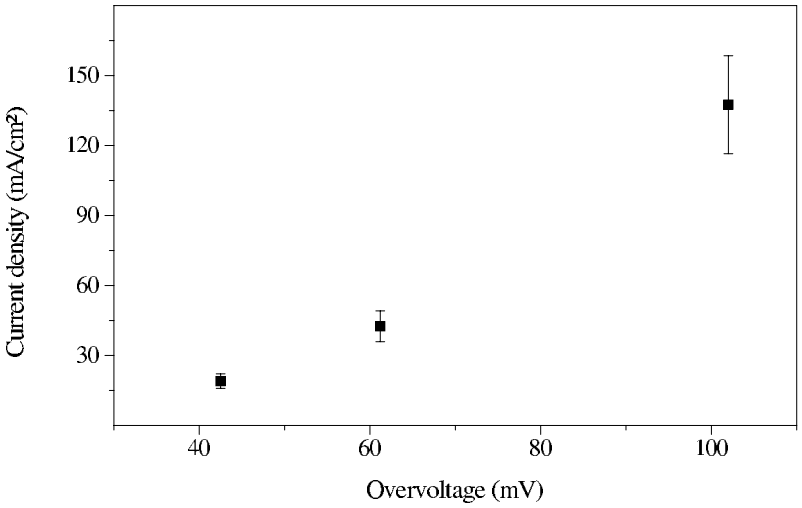

Figure 4.10: Current density as a function of the overvoltage for depositions in 50 nm diameter pores at T = 50 °C.

Part II

Characterisation of copper nanowires

Chapter 5

Morphological and structural analysis

Many efforts are made to measure physical properties of nanostructures and, in particular, also of electrodeposited nanowires. Since these properties, such as electron transport, magnetoresistance, or optical reflectivity, depend very much on their crystallinity and morphology, a detailed characterisation of the structures is required. We have performed a detailed study of the dependency of the morphology and crystallinity of copper micro- and nanowires on the electrodeposition parameters. We have investigated systematically the morphology of the resulting nanowires by scanning electron microscopy (SEM). Transmission electron microscopy (TEM) and electron diffraction (ED) were used to characterise the wires on the atomic scale, i.e., to observe their crystallographic structure and to confirm the morphology of the thinnest wires. Finally, we analysed the texture of the wires by X-ray diffraction (XRD).

5.1 Electrocrystallisation

Electrocrystallisation is the process controlling the build-up or dissolution of the crystal lattice at the electrode surface. The overall reaction of the Cu/Cu^{+2} electrode during formation of the bulk phase is given by

$$\mathrm{Cu}^{+2} + 2\mathrm{e}^{-} \Longleftrightarrow \mathrm{Cu} \tag{5.1}$$

Deposition of Cu on the electrode proceeds at negative overvoltages by incorporation of the atoms at the *kink site* positions (Fig. 5.1) as a final step of the reaction 5.1. Since a solid metal electrode surface is very complex, possessing crystallites with

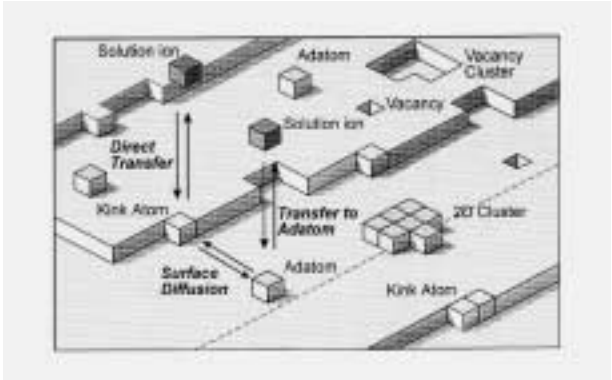

Figure 5.1: Schematic of the basic steps ocurring during metal deposition.

several orientations, grain boundaries, steps, dislocations, adsorbed molecules, oxides, etc., we will consider a simplified model to discuss the growth of a crystal by electrochemical deposition [86]. In Fig. 5.1 the two alternatives of this model for the creation of monoatomic layers (2D) are illustrated.
In the first one, the metal ions are partially discharged in the double layer and become adsorbed at the cathode on a flat surface of the growing crystal (transfer to the adatom in Fig. 5.1). In this process, the ions lose some of the water or other ligands, which were previously attached to them, in order to form bonds with the cathode surface, with partial or total neutralisation of the charge. Then, these adsorbed atoms diffuse over the surface to kinks, edges, steps, or other irregularities, where they, finally, incorporate to the metal lattice.
The second possibility is that the ions are directly discharged from the double layer into a fixed position in the metal lattice (direct transfer in Fig. 5.1).

The so created monolayers grow as long as the process is favoured. They stop growing if, for example, there are too few growth sites at the surface, or if the diffusion of the atoms on the surface is hindered by adsorbed impurities. When this occurs, a new layer or a new grain is formed. Generally, we distinguish two processes: the growth of already existing crystals and the creation of new grains, also called nucleation. These two processes are in competition with each other and are influenced by several parameters: surface diffusion, density of atoms adsorbed at the cathode surface, and overvoltage. Thus, a high surface diffusion, low density of ad-atoms and low overvoltages favour the growth of existing crystals, while the opposite conditions increase the nucleation rate [77]. The competition between crystal growth and nucleation determines the granularity of the deposit. The lower the nucleation rate during deposition, the bigger are the crystal grains. Therefore, in order to grow single-crystals, the growth of existing

crystals should dominate.

In order to understand the influence of the deposition parameters (η, T and electrolyte) on the crystallinity of the deposit, it is important to know how each of them affects the surface diffusion and density of ad-atoms.

Surface diffusion is the process through which the atoms adsorbed at the cathode surface, diffuse towards certain places on the surface, on which it is energetically favourable to incorporate to the metal lattice (mainly edge- and kink positions). The surface diffusion rate increases by increasing the temperature [86]. The dependence on the overvoltage is rather complicated being a function of the relation between the mean displacement of ad-atoms and the distance between steps [86]. At low overvoltages, the surface diffusion rate is directly proportional to the overvoltage.

The ad-atom concentration for a certain overvoltage η = E - E_{Eq} is given by eq. 5.2 [86]

$$\frac{c_{ads}}{c_{o,ads}} = e^{\frac{-zF\eta}{RT}} \tag{5.2}$$

c_{ads} being the concentration of ad-atoms at a certain voltage E, and $c_{o,ads}$ the concentration of ad-atoms at the equilibrium voltage E_{eq}. Thus, for a certain overvoltage η, the higher the temperature, the lower is the concentration of ad-atoms, and for a certain temperature T, the higher the overvoltage the higher is c_{ads}.

Besides, in section 4.1.1, the overvoltage η was defined as the difference between the potential applied E and the equilibrium potential E_{eq}. The Nernst equation (4.2) provides the dependence of the equilibrium potential with the temperature.

$$\eta = E - E_{eq} = E - E^{\ominus} - \frac{RT}{zF} \cdot \ln \frac{a_{\mathrm{Me}^{z+}}}{a_{\mathrm{Me}}} \tag{5.3}$$

Note that the higher the temperature, the higher is the equilibrium potential and, consequently, the lower is the overvoltage for a given applied voltage E. Since the overvoltage decreases at higher temperatures, the grain size should increase.

In conclusion, depositions at higher temperatures favour the growth of existing crystals over the creation of new grains, since at high T the surface diffusion is higher, the overvoltage is lower and the concentration of ad-atoms is lower. Low overvoltages also favour the growth of already existing crystals, not only due to their own influence on the process but also due to the decrease of the concentration of ad-atoms.

In the next paragraph, we discuss the influence of the electrolytes employed in this work on the crystallisation process. We employed two different electrolytes: a

simple-salt electrolyte and an electrolyte named Cupatierbad from Riedel Company.

The simple-salt electrolyte consisted of 238 g/l copper sulfate and 21 g/l sulfuric acid. To understand the influence of these electrolyte concentrations on the morphology of our deposits, we have to discuss the dependency of the overvoltage on these concentrations. On the one hand, as shortly mentioned in section 4.2.3, the concentration of copper sulfate is not particularly critical except that for copper sulfate concentrations above 250 g/l, the cathode overvoltage increases slightly [78]. On the other hand, it is known that the cathode polarisation decreases by adding a small amount of sulfuric acid, reaching a minimum at a concentration of around 30 g/l and increasing again at higher acid concentrations [78]. It was also found [87] that the addition of an excess amount of sulfuric acid drastically increases the cathodic overpotential and decreases the levelling ratio of electrodeposits, resulting in roundish precipitates. In those experiments [87], the authors compared SEM images of copper deposited from a pure copper sulfate and from an acidic copper sulfate electrolyte. They observed that, at relatively high overvoltages, much finer grains were created when the electrolyte contained an excess of acid, and they attributed this effect to three-dimensional nucleation processes, which take place at the larger surface overvoltages appearing when adding an excess of acid (surface overvoltage was defined by them as the difference between the total overvoltage imposed to the cathode and the concentration overvoltage). We can affirm that the electrolyte concentrations employed minimised the cathode overvoltage, thus diminishing the nucleation rate and favouring the growth of existing crystals, as is necessary for the growth of single-crystals.

The commercial bath Cupatierbad (Riedel Company) is formed by copper sulfate, sulfuric acid and chloride, as well as by some additives. These additional substances include brightening agents, and their composition is not disclosed by the company.
These additives, employed usually as brigtening or levelling agents, are usually adsorbed at the cathode, inhibiting growth of crystals through several mechanisms [78]. First, they negatively affect the diffusion of copper ions from the flat surface to the kink or edge positions, at which they finally constitute the growing crystal. When the growing layer encounters such adsorbed material, lateral growth may be stopped and continued growth is transferred to a new layer. Second, the adsorption of additives at the cathode surface also reduces the area available for electron transfer. This increases the effective current density and, in consequence, produces an increase of the cathode overvoltage. Finally, they can also block the growth at a step, thus increasing the concentration of ad-ions and consequently the polarisation. All these factors favour the process of nucleation and, consequently, the growth of polycrystalline structures.

5.2 Characterisation techniques

5.2.1 Scanning electron microscopy

The SEM can reveal topographic details of a surface with great clarity and detail. It can resolve morphologic details of less than 5 nm and possesses a depth of focus more than 500 times higher than that of the optical microscope at equivalent magnifications. Typical resolutions for SEM are around 10 nm. The combination of higher magnification, larger depth of focus, greater resolution, and ease of sample observation makes the SEM one of the most frequently used instruments in materials research today.

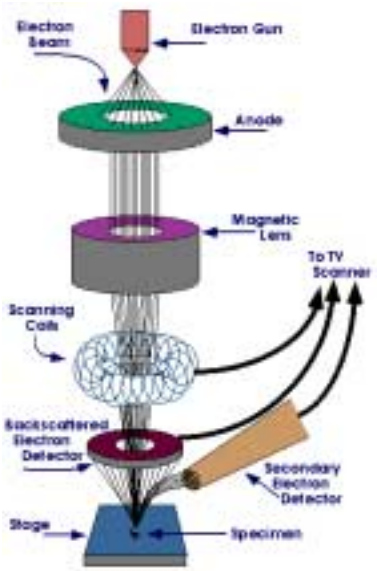

Figure 5.2: Schematic diagram of a scanning electron microscope.

The operation of a SEM is schematically depicted in Fig. 5.2. A beam of electrons is generated by an electron gun located at the top of the beam column. This beam is accelerated to the anode, condensed with a condenser lens, and focused to a very fine spot on the sample by the objective lens. The scan coils, by varying the voltage produced by the scan generator, create a magnetic field, which deflects the beam back and forth in a controlled pattern. The varying voltage is also applied to the coils around the neck of the cathode-ray tube (CRT) (TV in Fig. 5.2), which produces a pattern of light deflected back and forth on the CRT. In this way, the pattern of deflection of the electron beam is the same as the pattern of deflection of the spot of light on the CRT. SEM images can be generated by any signal produced by the interaction of a finely focused primary beam of electrons as it is scanned over the sample surface. This

interaction produces secondary and backscattered electrons, photons, Auger electrons, and X-rays characteristic of the sample under study (Fig. 5.3).

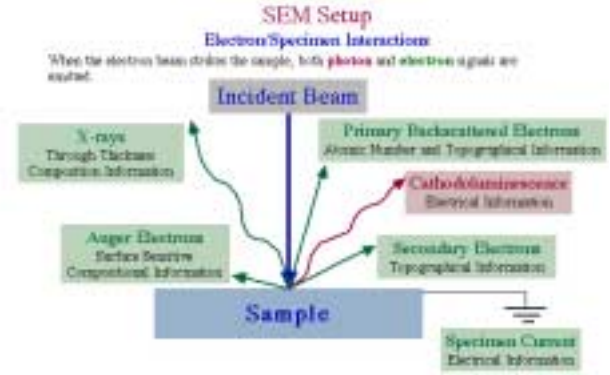

Figure 5.3: Illustration of the signal produced by an incident electron beam and the specimen.

For all measurements, we used a secondary electron detector (SED). Since secondary electrons are low-energetic, only the electrons from a very thin surface layer (some nm thick) reach the detector. Thus, we obtain information exclusively from this superficial layer. SEM observations are suitable to study the morphology of the wires while for further information about the crystallographic structure, electron diffraction analysis and high-resolution images are necessary. In this work, we employed a SEM Philips XL30.

Sample preparation The only requisite to observe the samples by SEM is that they have to be electrically conductive. Metallic samples as, e.g., our wires, can be placed directly into the SEM; nonmetallic samples, for example the polycarbonate foils, should be previously coated with a metal layer. In order to observe the wires, electrodeposition was stopped during the growth of the wires (region II in Fig. 4.3). A piece of the metal-filled membrane was placed on a SEM sample-holder and subsequently inmersed in a glass containing dichloromethane. The solution was exchanged several times to completely free the wires of polymer. Once they were clean, we took the sample out of the solution, the dichloromethane evaporated, and the samples were directly transferred to the microscope. The same procedure was used to look at the caps growing on top of the thicker wires. In the case of the thinner wires, the caps fall down under their own weight when the polymer was dissolved, and the wires lie over each other like "spaghetti" (Fig. 5.24). To observe the caps in these cases, the wires were kept in the membrane, and a conductive layer was sputtered on the surface.

5.2.2 Transmission electron microscopy

In transmission electron microscopy, the samples must have a thickness such that the electrons can pass through the sample, similar to how light is transmitted through the materials in conventional optical microscopy. Because the wavelength of the electrons is much smaller than that of light, a resolution higher by several orders of magnitude is attainable. Electrons can traverse the sample without any interaction (unscattered electrons) or can be scattered, elastically or inelastically, on their way (scattered electrons).

There are two modes of operation for TEM: forming electron diffractions and imaging.
Elastically scattered electrons do not loose energy during the interaction. Thus, all incident electrons scattered by the same atomic plane will be deflected under the same angle. The electrons can be collected using magnetic lenses to form a pattern of spots, the electron diffraction pattern, which is projected onto a viewing screen.
By readjusting the lens system, it is possible to form images by TEM. There are two main imaging modes. In bright-field imaging, the image is formed exclusively by the unscattered electrons. Contrast in these images is due entirely to thickness and density variations in the sample. Dark-field imaging, on the other hand, uses a single diffracted beam to form the image. This causes all regions of the specimen, which possess a different crystal structure or orientation than the sample zone producing the diffracted beam, to appear dark.

A more detailed description can be found in [88].

Sample preparation for TEM We employed two different methods to prepare the samples for TEM observations. The first procedure was similar to the one employed to prepare the samples for SEM. The polymer membrane was dissolved completely by exchanging the solvent several times. After this procedure, the wires stayed fixed to the copper bottom and the sample was carefully folded such that we could look at the wires standing at the edge (Fig. 5.4). The sample was then placed on a double TEM grid.

In the second approach, the first step was also the dissolution of the membrane in dichloromethane. Once the wires were completely free of polymer, they were separated from the bottom by using ultrasonic agitation. In a last step, several drops of clean solvent containing the wires were brought with a pipette onto the TEM grid.
We employed in most cases the first method. Measurements were performed with a

Figure 5.4: Image showing the profile of a sample prepared for TEM observations.

Philips CM20 Ultra Twin at the University of Technology of Darmstadt (Germany), and with a Philips 200 kV at the Max-Plank- Institute for Microstructure Physics in Halle (Germany).

5.2.3 Four-circle x-ray diffractometry

If we consider parallel lattice planes at a distance d, the path length difference for rays reflected from adjacent planes is $2d \sin\theta$, where θ is the angle formed between the plane and the incident beam. When the path length difference is an integer number of wavelengths λ, the reflected waves are in phase and constructive interference occurs [89].

$$2d \sin\theta = n\lambda \tag{5.4}$$

Therefore, to observe a particular diffraction maximum, the appropriate sets of planes must be oriented in space such that the angle between the incident beam (fixed in space) and the set of planes in the crystal is made equal to the angle θ given by the Bragg equation (5.4).

We will first consider a poly-crystalline powder sample, composed by many small grains with all possible orientations. The angle between the x-ray source and the de-

tector is defined as 2θ. A diffraction experiment consists then in rotating the detector about the sample. Given a wavelength λ, the diffracted rays will be detected at certain angles coming from individual crystallites that happen to be oriented with planes forming an incident angle θ with the original beam satisfying the Bragg law (see Fig. 5.5). If we now consider a single-crystal, it can be thought as consisting of numerous sets of planes. If we want to know which orientation our crystal has, two conditions have to be verified: the reflection must be specular (i.e. $\theta_{in} = \theta_{out}$) and the angle is given by the Bragg law for a certain set of planes. Therefore, a $\theta - 2\theta$ scan is performed by rotating sample and detector, increasing 2θ and keeping $\theta_{in} = \theta_{out}$ (see Fig. 5.6).

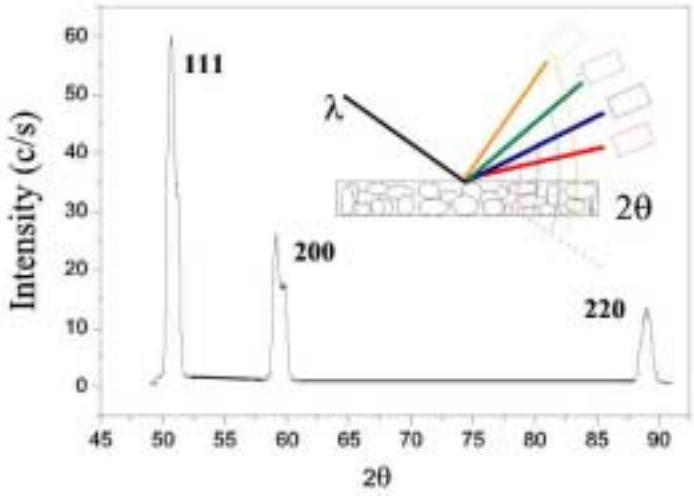

Figure 5.5: Schematic of the diffraction of an incident x-ray beam from a polycrystalline sample.

A schematic of the geometrical orientations of the apparatus is shown in Fig. 5.7. ω (also θ and 2θ) defines the rotation about the vertical axes of the diffractometer, χ is the angle of inclination about a horizontal axis through the center of the circle, and ϕ defines the rotation about the axis of the goniometer head (sample holder). The counter moves only in the horizontal plane and the crystal is rotated about the incident beam direction until the normal to the diffraction plane lies in the horizontal plane. All that then remains is to position the counter at an angle θ to the plane, and hence at an angle 2θ to the incident beam. By rotating the detector around the vertical axes of the diffractometer (ω), we perform the above mentioned θ-2θ scan, equivalent to the poly-cystalline powder diffractogram. We will obtain a reflection at angles at which the Bragg condition is satisfied.

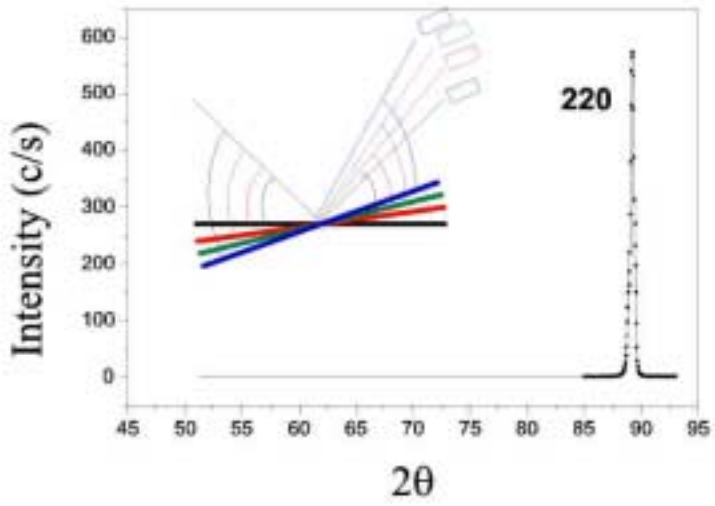

Figure 5.6: Schematic of the diffraction of an incident x-ray beam from a single-crystalline sample.

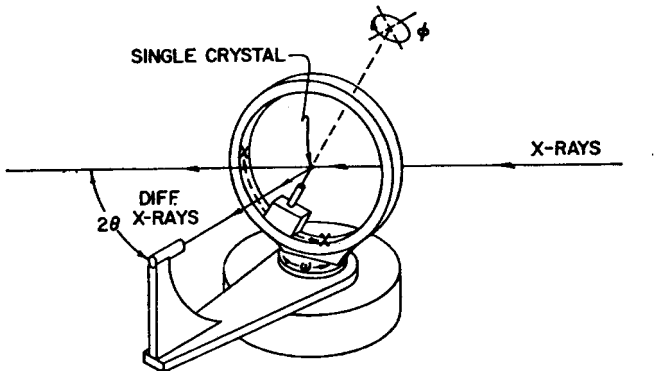

Figure 5.7: Schematic showing the different angles in a four-circle x-ray diffractometer.

The preferred orientation of the deposit is expressed in terms of the texture coefficient, TC, which is defined as

$$TC_{(h_1,k_1,l_1)} = \frac{I(h_1,k_1,l_1)/I_o(h_1,k_1,l_1)}{(1/n)\cdot\sum I(h_n,k_n,l_n)/I_o(h_n,k_n,l_n)} \tag{5.5}$$

where $I(h_1,k_1,l_1)$ and $I_o(h_1,k_1,l_1)$ are the integrated intensities of (h_1,k_1,l_1) reflections measured for the sample of interest and a standard powder sample respectively, and n is the total number of considered reflection planes. If the TC of any (hkl) plane is larger than unity, a preferred orientation exists in which grains are oriented with

their (hkl) planes parallel to the surface. The larger the value of TC, the greater is the degree of preferred orientation. The integrated intensities can be also replaced by the maximal intensity of the reflection, always that the width measured for each of the peaks is similar.

A so-called rocking curve consists then in positioning the detector for a certain reflection θ_1 and subsequently rotating the sample in either ω or χ. This is schematically illustrated in Fig. 5.8. In this way, we obtain information about the texture of the sample. A narrow peak indicates a high degree of orientation, i.e., all planes are oriented in a certain direction within several degrees so that the Bragg condition is only satisfied within a narrow angle distribution. A broad peak means the opposite, the Bragg condition is satisfied within a broad range of degrees. The width of the peak is defined as Full Width Half Maximum (FMWH).

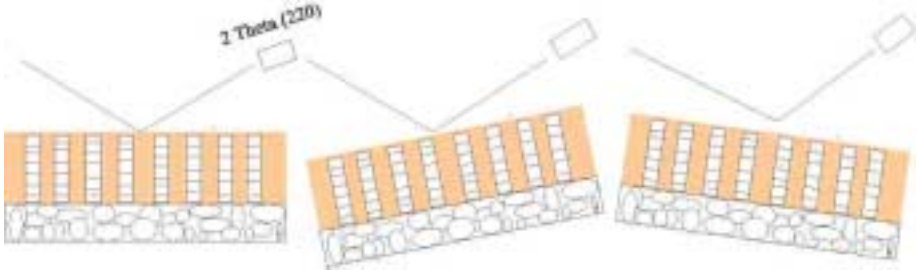

Figure 5.8: Rotation of the sample in χ or ω.

5.3 Microscopic analysis

In this section, we present our studies on the dependency of morphology and crystallographic structure of electrodeposited copper nanowires on the deposition parameters: overvoltage, temperature and electrolyte. For the characterisation of the needles, the electrodeposition process was stopped during phase II (cf. Fig. 4.3).

5.3.1 Morphology

Figure 5.9 shows two SEM overviews at different magnifications of 50 nm diameter wires after dissolution of the polymer membrane. The smoothness of the contour and the uniformity along their length can be clearly seen for all the wires.

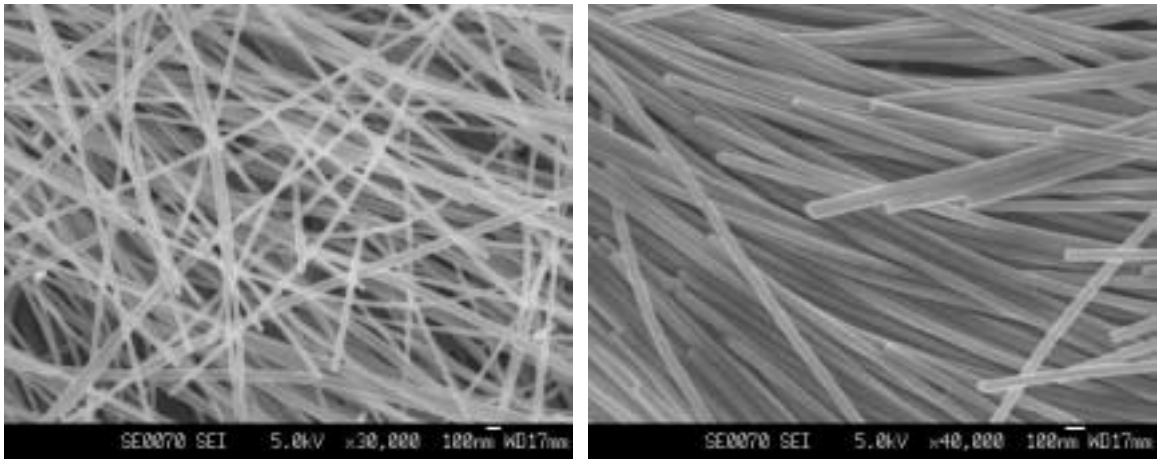

Figure 5.9: SEM overviews of 50 nm diameter wires after dissolution of the polymer membrane at two different magnifications.

The geometry of the wires depends, as discussed in section 3.4.3, on the irradiation and etching conditions. However, the surface smoothness of the wires depends on several factors such as the quality of the polymer and the etching process. Our observations strongly indicate that, besides these factors, also the conditions during electrodeposition play an important role.

TEM images of two copper nanowires created under different conditions are shown in Fig. 5.10. In the case of Fig. 5.10 (left), the wire was deposited at 50 °C and an overvoltage of $|\eta| = 50$ mV, from the simple-salt electrolyte. The needle possesses cylindrical geometry and a smooth contour over the entire length. The contour of the

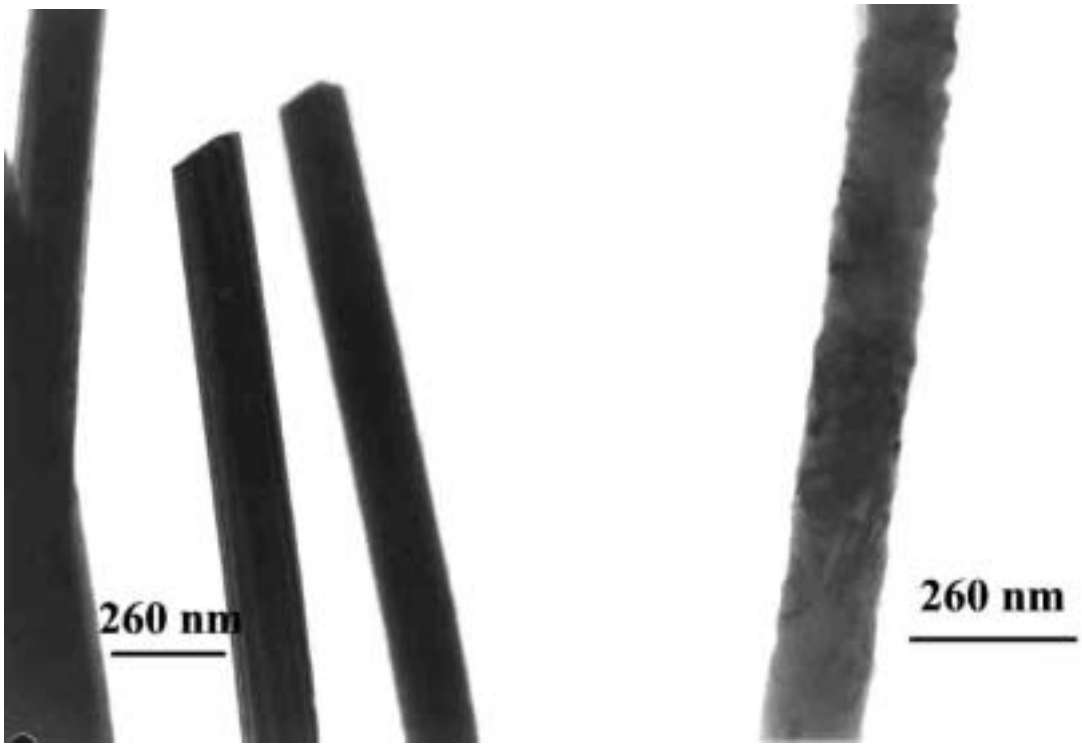

Figure 5.10: TEM images of wires fabricated under different deposition conditions showing their different morphologies. (left) T = 50 °C and $|\eta|$ = 50 mV, (right) RT and $|\eta| \approx 1$ V.

wire in Fig. 5.10 (right) is clearly rougher. In this case, the deposition took place at room temperature and at much higher voltages ($|\eta| \approx 1$ V), employing the commercial electrolyte Cupatierbad [90]. This rather large roughness of the wire surface, already mentioned by other authors, is caused by the presence of air bubbles in the pores, hydrogen evolution during depositions at too high overvoltages, or bad quality of the deposited metal at too high current densities. When grown at high temperatures and lower overvoltages, employing the same electrolyte, the wires possess very homogeneous and smooth surfaces [69].

In Fig. 5.11, the image of a copper nanowire of aspect ratio 1000 (length 30 μm and diameter 30 nm) is depicted. The wire, created at 50 °C and $|\eta|$ = 60 mV, exhibits a smooth and homogeneous contour along its whole length.

Figure 5.12 shows the images of the tips of three different microwires obtained after the dissolution of the polymer membrane in CH_2Cl_2 [91]. This series of images is a clear example of different morphologies obtained under different deposition conditions, which

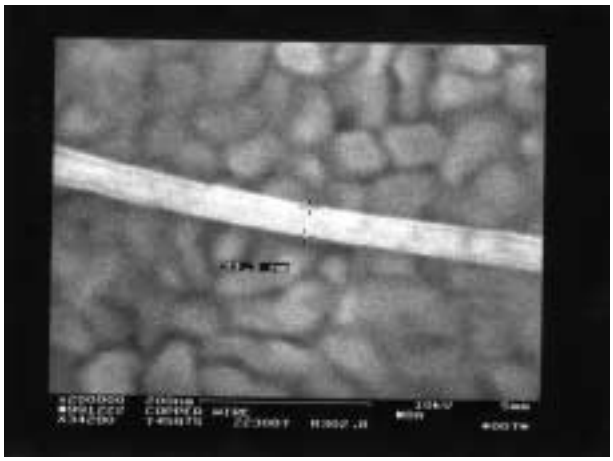

Figure 5.11: SEM image of a copper nanowire with aspect ratio 1000 (length 30 μm and diameter 30 nm) showing a smooth and homogeneous contour.

indicate, in addition, a variation in the crystallinity of the wires. The three samples were deposited galvanostatically at nearly the same current density, j = 15 mA/cm^2, but at different temperatures of the commercial electrolyte (Cupatierbad). At room temperature (Fig. 5.12(a)) fine-grained polycrystalline wires were created. At 40 °C (Fig. 5.12(b)) the wires were still polycrystalline, but with larger grains. Finally, at 60 °C (Fig. 5.12(c)) the facets correspondent to the fcc (face centered cubic) structure of Cu can be clearly observed at the tip of the wire, indicating a single-crystalline structure. Our results show a clear increase of the grain size of the deposits at higher temperatures. As discussed in section 5.1, the increased temperature leads to a decrease of the cathode polarisation, a lower density of ad-atoms and an increase of the surface diffusion. These three factors favour the growth of pre-existing nuclei, and therefore the deposition of single-crystals. At higher overvoltages or at T $\leq$ 50 °C, the wires exhibit a polycrystalline morphology.

The SEM image of several Cu needles deposited galvanostatically from the simple-salt electrolyte at T = 60 °C also show both the facetted tips of the wires and a homogeneous smooth contour of the wire (Fig. 5.13).

Fig. 5.14 shows some examples of different wire morphologies indicating a single-crystalline structure. Though the SEM images, give us an indication for the crystallinity of the wires, the internal structure should be further investigated in order to confirm the single-crystallinity of the needles.

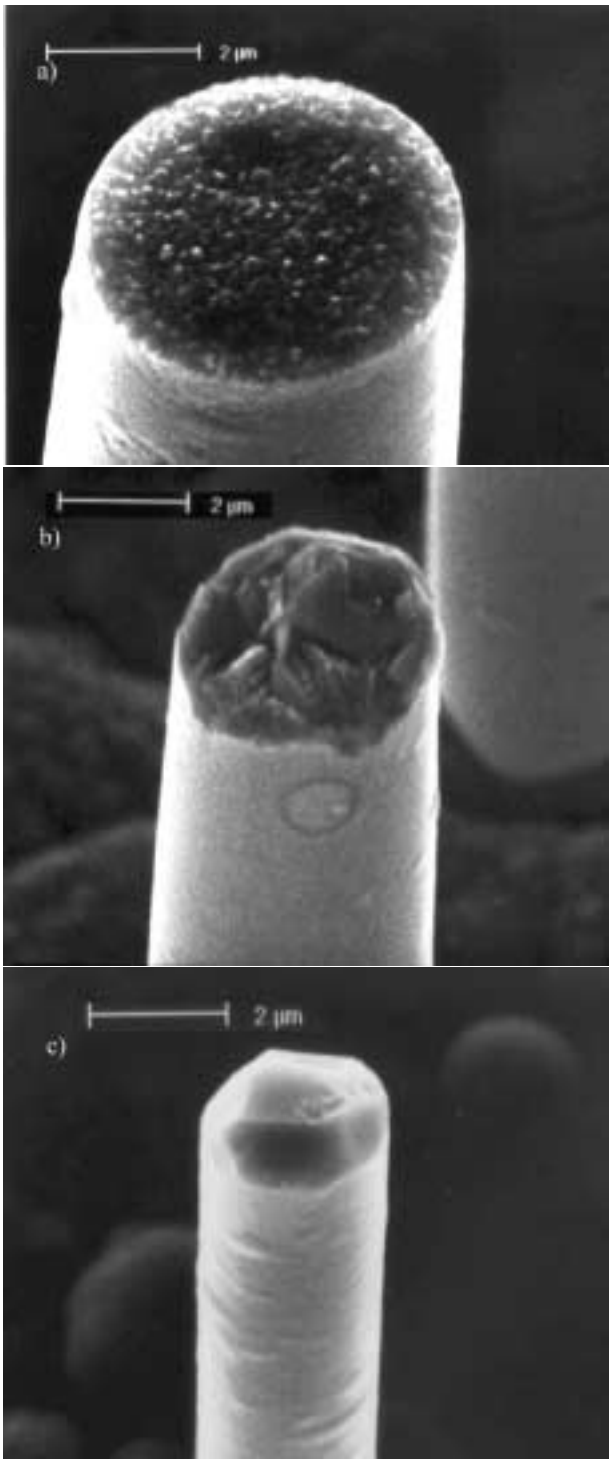

Figure 5.12: Copper needles grown at a current density of $\sim$ 15 mA/cm^2. Different morphologies were obtained at different temperatures: a) Polycrystalline needles at room temperature, b) larger grain sizes at T = 40 °C, c) Single-crystalline morphology at T = 60 °C. Scale bars: 2 μm.

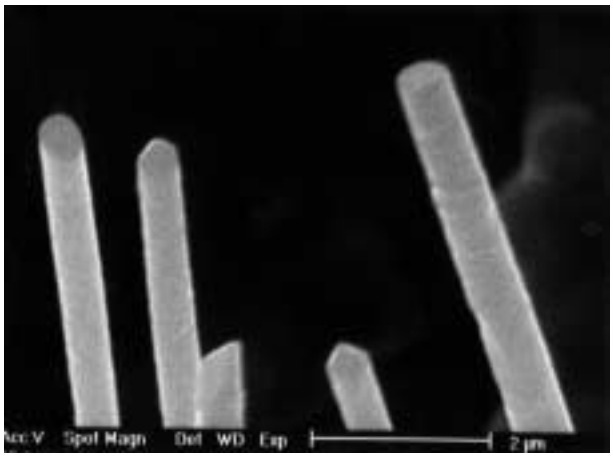

Figure 5.13: SEM image of several 500 nm diameter copper wires.

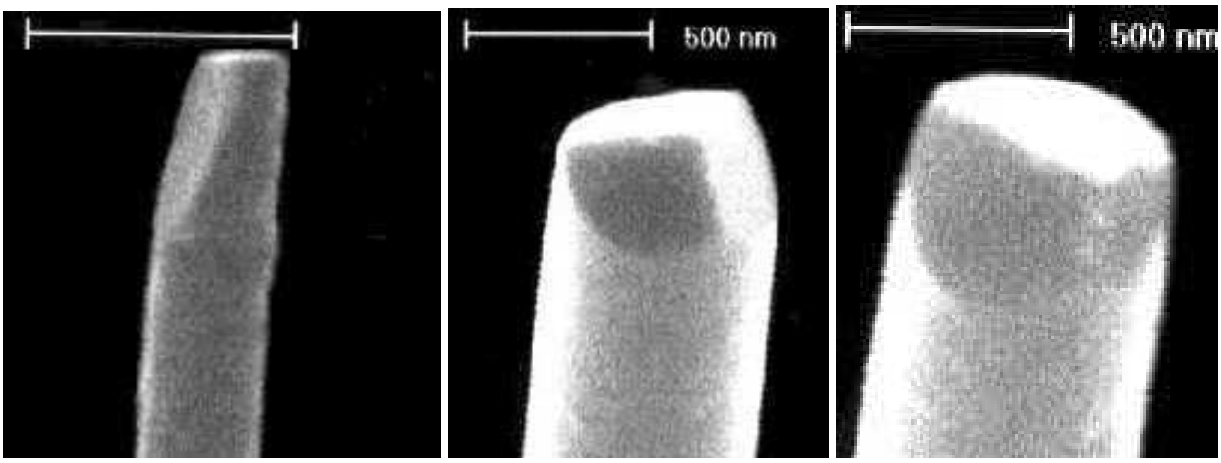

Figure 5.14: SEM images of copper wires indicating a single-crystalline structure. Scale bars: (left) 1 μm, (center) 500 nm, (right) 500 nm.

5.3.2 Crystallinity

The thinnest wires (diameter $\leq$ 200 nm) were also characterised by TEM. Selected-area electron diffraction (SAED) patterns and bright- and dark-field imaging revealed the kind of crystallinity of the needles. A TEM image of both a single- and a poly-crystalline wire is shown in Fig. 5.15. At the left side, the picture of a single-crystalline wire, deposited at 50 °C and $|\eta| = 50$ mV is shown. The contrast is constant along the needle, and the facets at the tips of the needle, shown earlier in SEM images

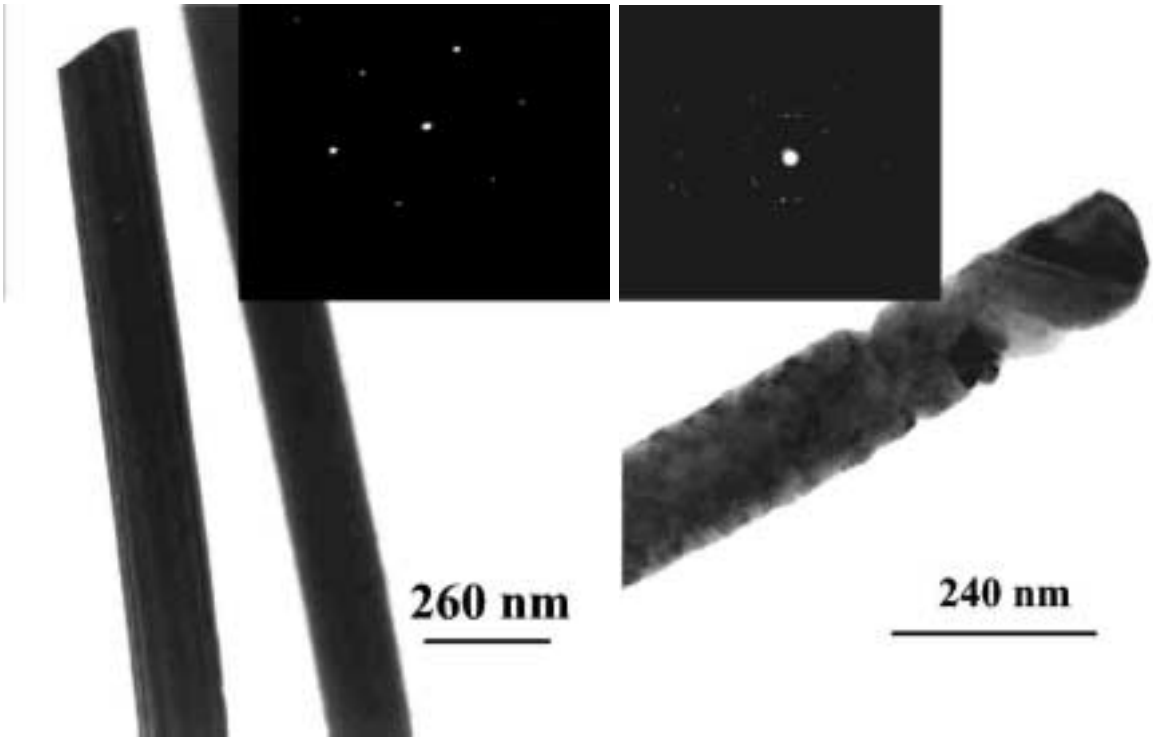

Figure 5.15: TEM images of (left) a single- and (right) a poly-crystalline wire. The insets show SAED patterns, respectively confirming the single- and poly-crystalline structure.

(Fig. 5.14), can be also observed in this image. The ED pattern confirms its single-crystallinity. At the right, an image of a poly-crystalline wire, formed by many different grains (zones of different brightness along the wire), is shown [90]. It was deposited at room temperature and $|\eta| \approx 1$ V. The diffraction pattern confirms its poly-crystalline character. It can be observed that the rings are made up of discrete spots, rather than forming a continuous line pattern. This indicates that the wire is formed by large grains [88].

Fig. 5.16 shows a bright-field image of a 60 nm diameter wire, which was deposited at 50 °C applying an overvoltage of $|\eta| = 45$ mV. The high magnification image, exhibiting the undisturbed lattice at atomic resolution, proves the single-crystallinity of the wire. No defects are observed on this wire section.

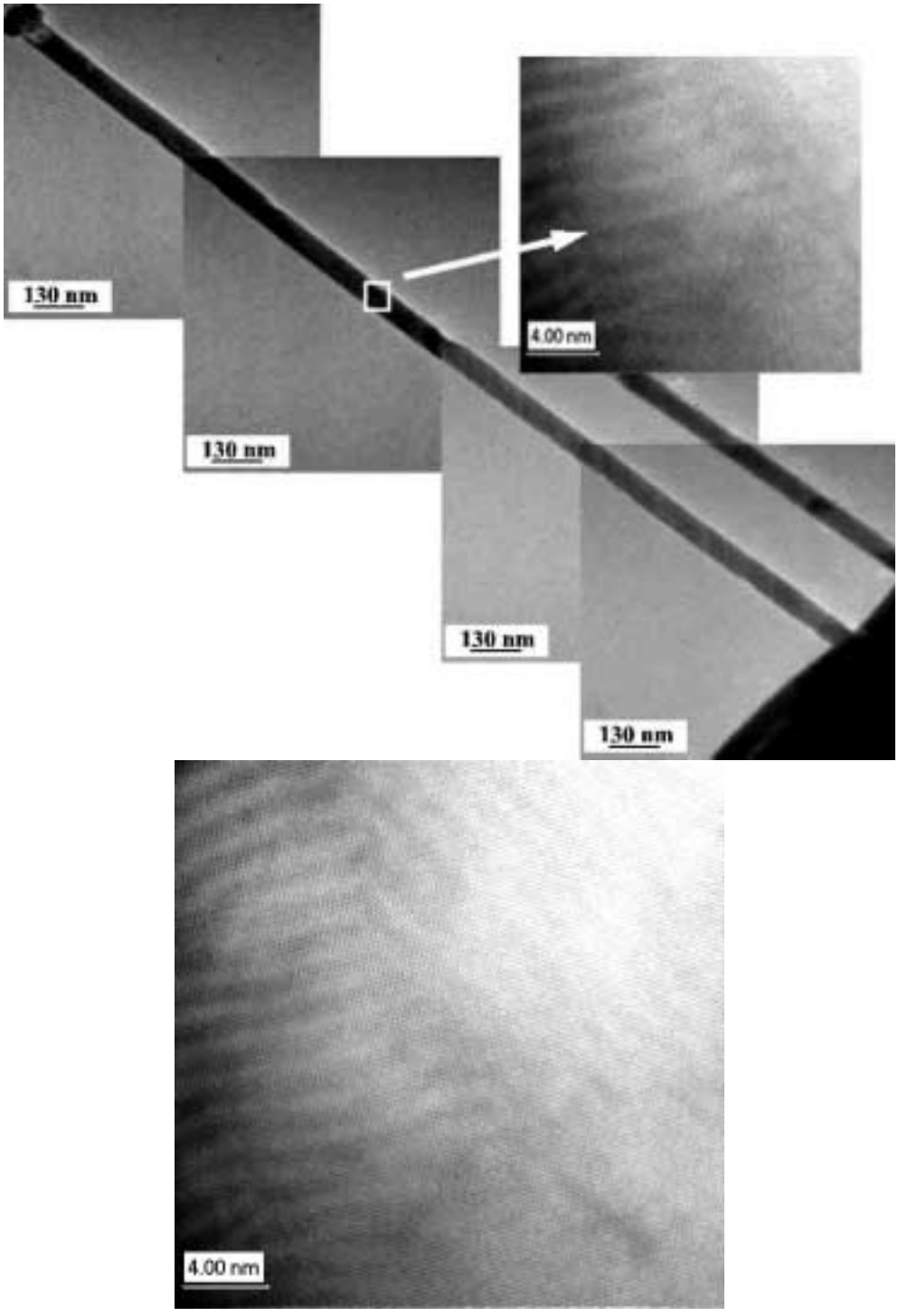

Figure 5.16: (top) Series of TEM images showing the homogeneous contour of a copper nanowire. (bottom) Magnified image showing the single-crystalline character of the wire at the atomic scale.

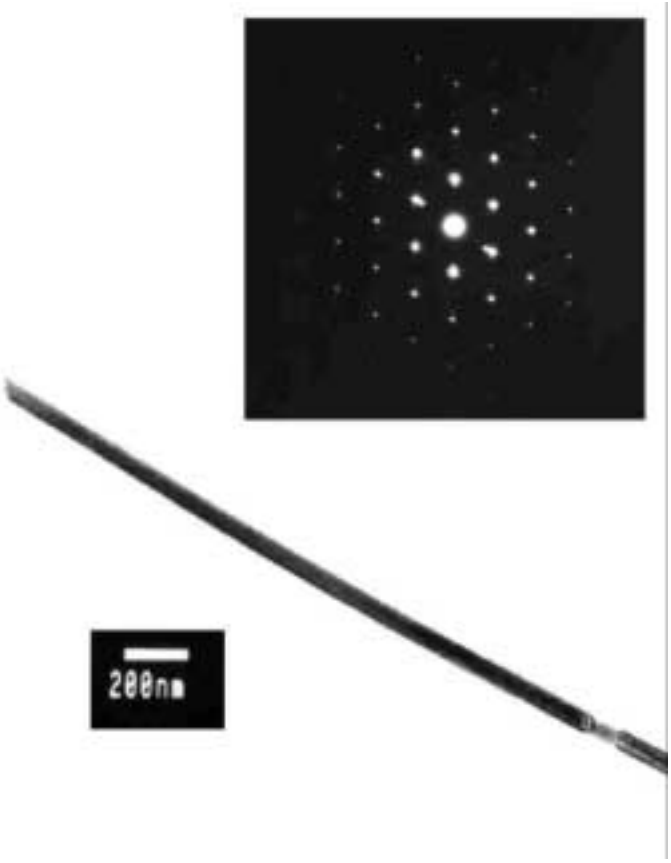

Figure 5.17: TEM micrograph of a single-crystalline section of a 70 nm diameter copper nanowire. The $\langle 111 \rangle$ electron-diffraction pattern gives evidence for the single-crystalline structure. Scale bar: 200 nm.

Fig. 5.17 shows another TEM image of a 60 nm diameter single-crystalline wire (deposition conditions: simple-salt electrolyte, T = 50 °C and $|\eta| = 45$ mV). The ED (see inset) gives evidence for single-crystalline structure [91].

The overview on Fig. 5.18 is a typical image obtained for the samples presented here. When moving the electron beam along several micrometers of the wire, in some cases, the diffraction patterns do not vary, showing that it consists of one crystal. In other cases, the diffraction pattern changes, indicating that the wires consist of long single-crystalline sections, simulating a bamboo-structure. Conceivably, the bamboo-like structure of the wires is partially due to twinning (see following section).

TEM investigations are in agreement with the indications obtained from our SEM observations on the morphology of the copper wires, showing that wires with diameters smaller than 200 nm grown at $|\eta| \leq 60$ mV at T = 50 °C possess a single-crystalline structure.

Figure 5.18: TEM image showing an array of copper nanowires of 45 nm diameter.

5.3.2.1 Twin formation and slips

All real crystals contain defects. Two typical defects of fcc structured crystals are twinning and slips. Both have been observed by TEM in the electrodeposited nanowires. Twinning is characterised by the partial displacement relative to the matrix of a considerable number of neighbouring crystal planes. A twin is obtained by rotating the matrix lattice 180 ° about a particular orientation, known as twin axis, such that the twin lattice is the mirror image of the matrix lattice [89].
In Fig. 5.19 (left) the twins are recognised by their reduced brightness, appearing as a straight band that extends across the whole nanowire width. The angle between the twin plane and the wire axis is 30 °. Twins can be created during the deposition process or may result from plastic deformation. A second mode of plastic deformation are slips. In a slip, one part of the crystal slides as a unit along an adjacent part. Fig. 5.19 (right) shows an example observed for a 100 nm diameter wire. In our case, they were probably produced when dissolving the polymer membrane and placing the wires on the TEM grid. Both slips and twins influence the mechanical properties of the wires.

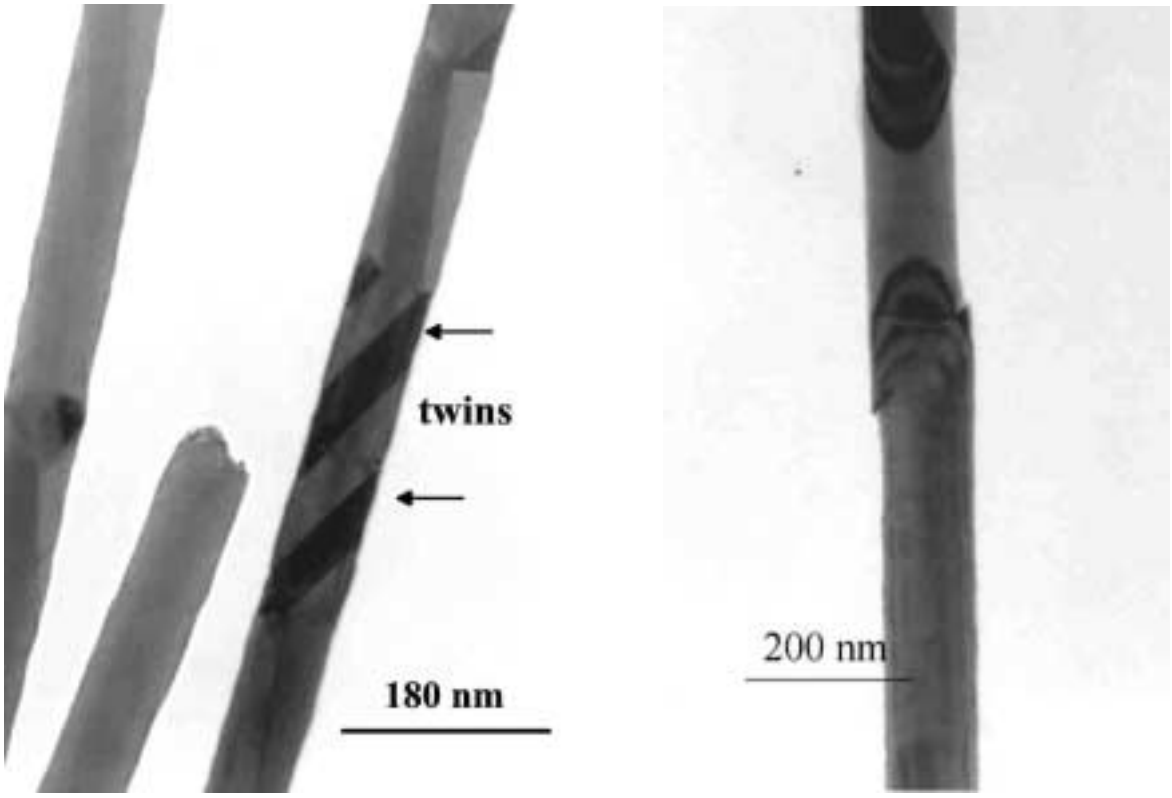

Figure 5.19: Lattice defects in single-crystalline copper nanowires. (Left) Twin structure in a 70 nm diameter wire, (right) slip in a 100 nm diameter needle.

5.3.2.2 Wire caps

When the deposition process is stopped during phase III (cf. Fig. 4.3), an indication for the crystalline structure of the needles is given by the shape of the caps, grown on the membrane surface. Fig. 5.20 displays two typical cases: faceted caps are related to single-crystalline needles (Fig. 5.20 left), whereas caps with round shape are formed if the needles are polycrystalline (Fig. 5.20 middle). While the caps displayed in Fig. 5.20 left and (middle) were obtained from the simple-salt solution, caps in Fig. 5.20 right were obtained from a commercial electrolyte. In this latter case, we can observe the smooth round shape resulting from the much smaller size of grains which form the caps, due to the influence of the commercial electrolyte (commented in section 5.1).

Some attention should be given to the faceted caps, obtained under electrodeposition conditions favouring single-crystalline growth. In Fig. 5.21 the morphology of several faceted caps is depicted:

The structures of the caps shown in Fig. 5.21 (left and center), show a five-fold

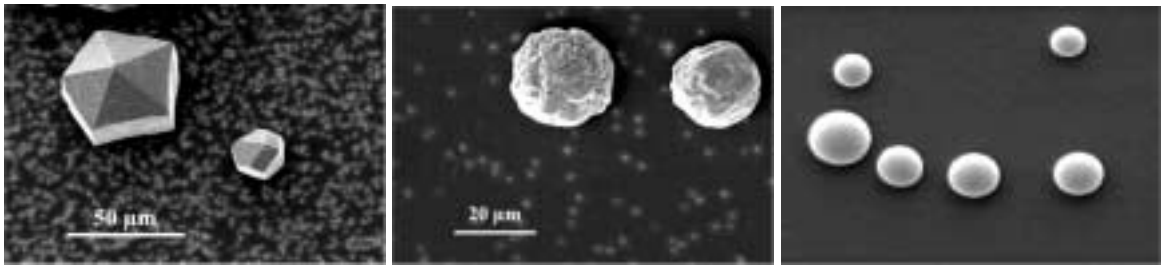

Figure 5.20: SEM images of (left) single- and (center) polycrystalline caps grown after the copper deposition has reached the surface of the polymeric membrane, using a simple-salt electrolyte. At the right, polycrystalline caps with smaller grain size. In this case a commercial electrolyte was employed.

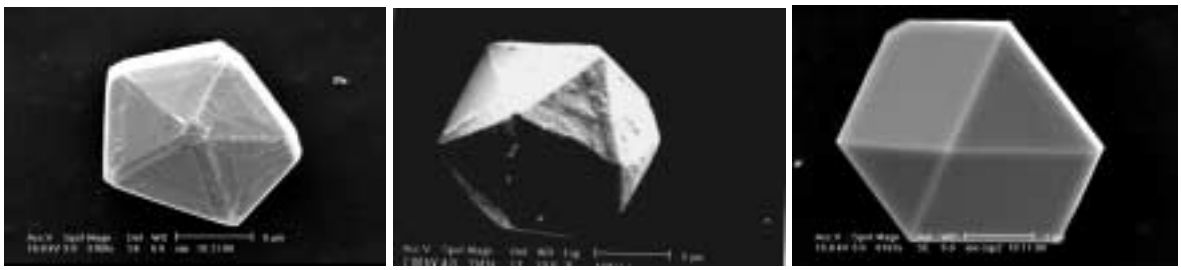

Figure 5.21: SEM images of faceted caps grown after the copper deposition has reached the surface of the polymeric membrane, using a simple-salt electrolyte.

symmetry, and are known as multiple twinned particles. The name was given in the sixties of the 20th century, by Sh. Ino, who studied the structure of small particles, formed in ultrahigh vacuum at the earlier stages of deposition of gold films on NaCl and KCl [92, 93, 94]. In [95] a five-fold symmetry in copper whiskers grown by reduction of copper iodide was also observed. Ino described the structure in Fig. 5.21 (left) as a truncated decahedron (decahedra with additional intermediate planes), consisting of five deformed tetrahedral subunits. As shown schematically in Fig. 5.22 left, a nucleus tetrahedron OABC is considered, and two tetrahedra of the same size as the nucleus, OACL and OABF, called primary twins of the nucleus tetrahedron are piled upon the two (111) surfaces of the nucleus. Finally, at the two (111) faces of the primary twins, OAF and OAL, two secondary twins are piled up. Theoretically, in this model, the union of these five tetrahedra causes a gap of $7^{\circ}\ 20'$, which should dissappear due to a lattice imperfection distributed within the whole particle [94]. This imperfections have been often observed in our SEM images.

Icosahedral particles (Fig. 5.21 center) consist of 20 deformed tetrahedral subunits. The deformation must be introduced in order to avoid gaps between the faces of adjoining subunits. The scheme is presented in Fig. 5.22 (right), indicating the tetrahedra nucleus OABC. The other 19 tetrahedra are piled up.
The morphology of the cap in Fig. 5.20 (right), corresponds to the cubic structure of copper.

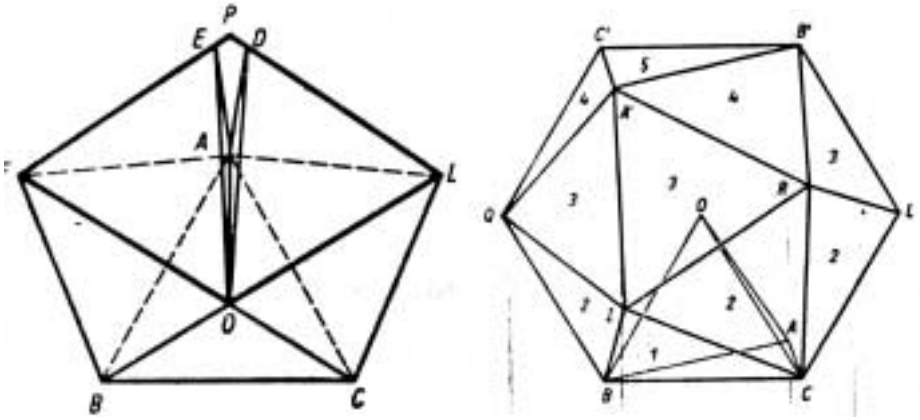

Figure 5.22: Schematic of the decahedra and icosahedral particles [93]

5.3.2.3 Texture

While ED patterns are obtained from individual nanowires, x-ray diffraction analysis gives us information from millions of needles still embedded in the polycarbonate membrane. To investigate possible textures of the wires, a STOE four-circle diffractometer with graphite monochromatized CoK_α radiation ($\lambda = 1.7902\ \mathring{A}$) was employed.

For a copper powder sample, the maximal intensities $I_o(h, k, l)$ are 100, 53 and 33 for the reflections (111) ($2\theta = 50.7°$) , (200) ($2\theta = 59.3°$) and (220) ($2\theta = 88.84°$), respectively [96]. Thus, a ratio (220)/(111) = 33/100 is expected for such a sample. The diffractogram of a single-crystalline sample, whose 60 nm diameter wires were deposited at 50 °C applying $|\eta| = 45$ mV, shows an extremely strong (220) reflection (Fig. 5.23 left). The ratio of the measured intensities of the (220) and the (111) reflections is by a factor of 10 larger than for a standard powder sample. In addition, the rocking curve of the (220) copper reflection is given in Fig. 5.23 right. While the (111) and the (100) reflection planes did not show any preferred orientation, we found

a strong texture for the (110) reflection planes. The maximum at $\omega = 44.2 \pm 0.3$ ° gives evidence for strongly preferred orientation of the diffracting planes parallel to the substrate surface i.e. perpendicular to the wire axis (deviations from $\omega = 44.4$ are measured because the sample could not be fixed completely parallel to the holder). Most striking is the narrow peak width or Full Width Half Maximum (FWHM = 0.6 °) indicating both a very high degree of orientation of the crystalline planes in the copper wires and also of the wires with respect to the membrane.

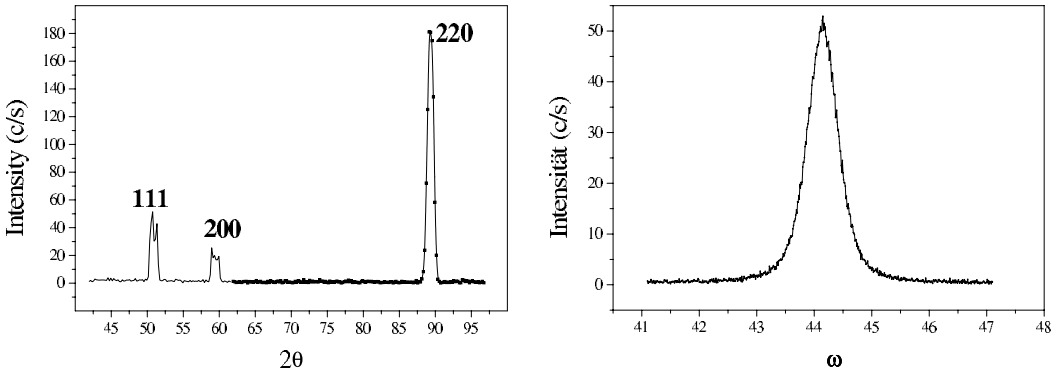

Figure 5.23: (left) θ-2θ diffractogram measured on 60 nm diameter copper nanowires, (right) Rocking curve on the (220) reflection, centered at $\omega = 44$ °. The FWHM is 0.6°.

Due to their small diameter, the wires fall by, due to their own weight, when the polymer membrane is dissolved (Fig 5.24). We used this fact in order to confirm the results on the texture of the wires. The diffractogram measured for the same sample after dissolving the polymer membrane in dichloromethane, did not show any preferred orientation. Besides, we prepared a polymer membrane and deposited the conductive layer on one side. Without depositing any wires, we recorded diffractograms of random orientation. Again the absence of a preferred orientation confirms our previous results, indicating a strong texture for the wires grown at $|\eta| = 45$ mV.

Similar measurements were made on the series of samples, presented in section 4.3.3. All samples were irradiated and etched under the same conditions. The density of pores is $4.6 \cdot 10^8$ ions/cm^2 and the pore diameter about 50 nm (see Fig. 3.10). Electrochemical growth took place at 50 °C at different overvoltages, and at room temperature at $|\eta| = 110$ mV (see Table 4.4).

In Fig. 5.25, the (220) reflections of the diffractograms of three samples deposited at different overvoltages, normalised with respect to (111), are presented. It is observed that the ratio (220)/(111) increases considerably for lower overvoltages. Reflections

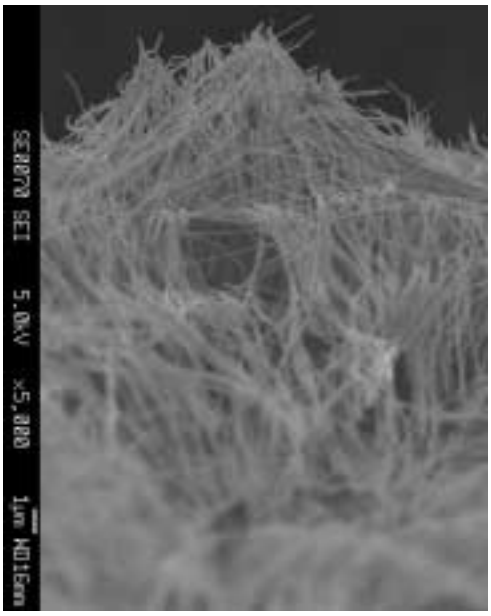

Figure 5.24: Overview of 50 nm diameter wires after dissolution of the polymer membrane.

(111) and (200) are not included since the ratio (200)/(111) is, with small variations, about 0.5 in all cases (see Table 5.1). Fig. 5.26 depicts the rocking curves on (220) for the same samples. On the other hand, in Fig. 5.27, the diffractogram shows the three reflections obtained for the sample *yyy*, deposited at $|\eta| = 110$ mV at room temperature. In this case, no preferential orientation is shown. No texture was either noticeable in the measured rocking curves (in χ and ω).

Values of the normalised intensity of the three main reflections, the texture coefficient (TC), and the FMWH of their corresponding rocking curve are presented in Table 5.1 for all four samples. As explained in section 5.2.3, a texture coefficient greater than 1 indicated a preferred orientation and all coefficients equal to one indicates that the sample consists of randomly orientated crystals.

The results show a strong $\langle 110 \rangle$ texture for all samples deposited at 50°C and voltages varying between $|\eta| = 42.5$ and 102 mV. The sample deposited at $|\eta| = 110$ mV at room temperature did not show any preferred orientation. For this sample, all TC are close to one, indicating a random distribution of orientations. These results support, on one side, the results obtained by TEM, which attributed a polycrystalline structure to the wires in sample *yyy*. On the other side, the results are in agreement with other works in the literature, which report a $\langle 110 \rangle$ texture for depositions from acid copper solutions at high temperatures [97]. Besides, a small increase of the texture

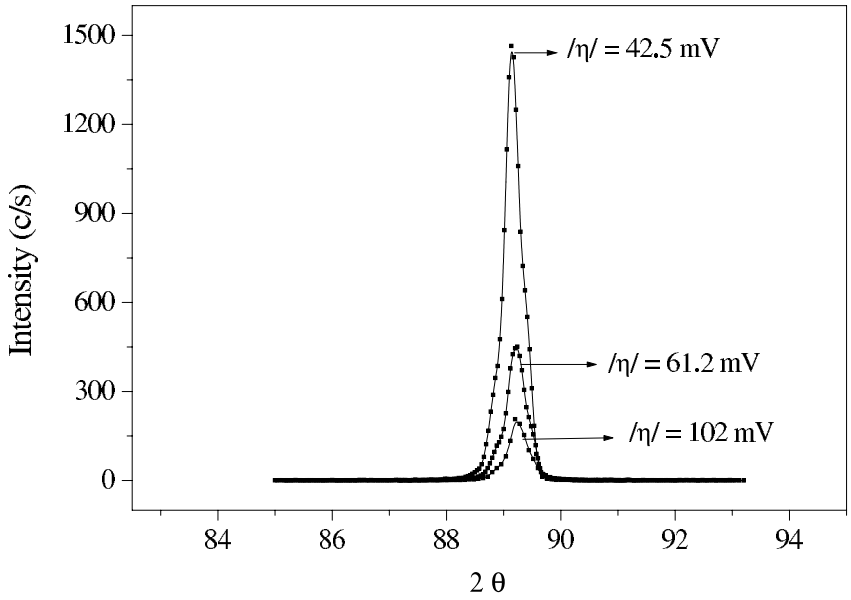

Figure 5.25: (220) reflection normalised with respect to (111) for samples deposited at three different overvoltages.

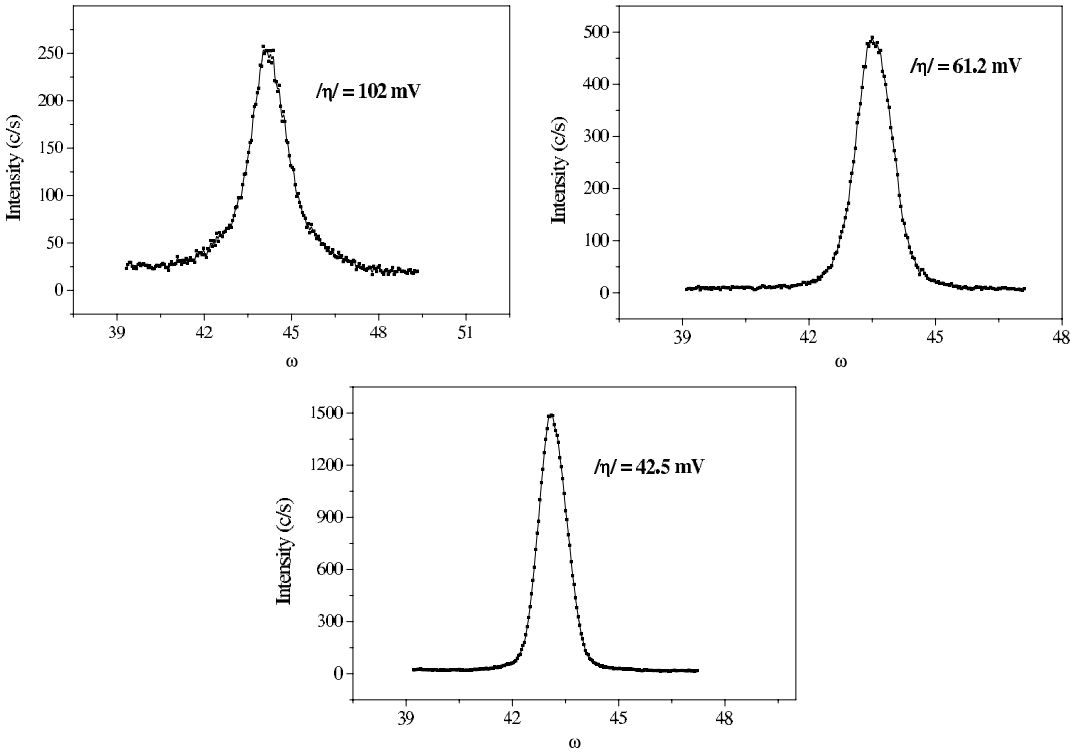

Figure 5.26: Rocking curve on the (220) reflection, centered at $\omega = 44$ ° for samples deposited at 50 °C and different overvoltages.

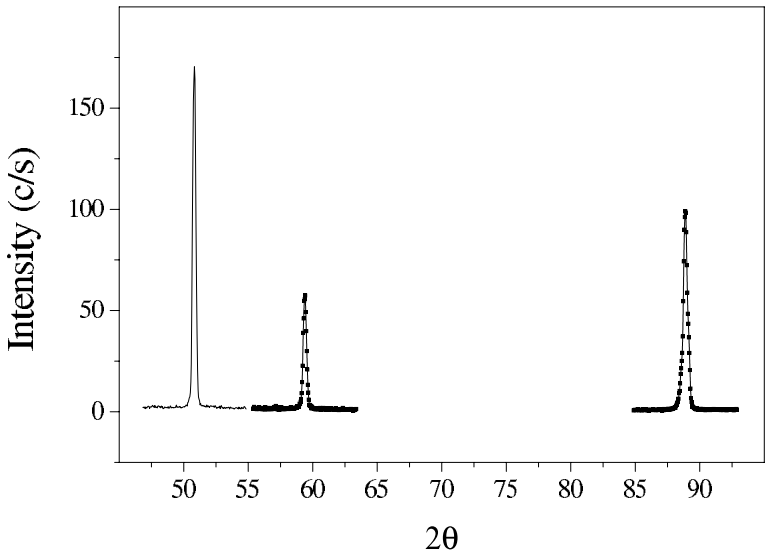

Figure 5.27: $\theta - 2\theta$ diffractogram measured on 50 nm diameter wires, deposited at room temperature and $|\eta| = 110$ mV.

Sample	$\|\eta\|\,(mV)$	T (°C)	Reflect	Normalised Intensity	FMWH (°)	TC
95.3	42.5	50	(111)	100	∞	0.06
95.3	42.5	50	(200)	43	∞	0.05
95.3	42.5	50	(220)	1500	1.1	2.88
96.3	61.2	50	(111)	100	∞	0.19
96.3	61.2	50	(200)	45	∞	0.16
96.3	61.2	50	(220)	475	1.5	2.64
98.3	102	50	(111)	100	∞	0.37
98.3	102	50	(200)	38	∞	0.27
98.3	102	50	(220)	208	1.3	2.35
yyy	110	RT	(111)	100	∞	1.12
yyy	110	RT	(200)	34	∞	0.72
yyy	110	RT	(220)	34	∞	1.15

Table 5.1: Values obtained for the samples, for which deposition took place at different overvoltages and temperatures.

coefficient of (220) is measured as the overvoltage, i.e., current density, decreases. No other texture was found in the range of potentials applied. To look for other reflections forming certain angles with the (110) planes is not possible due to the cylindrical geometry of the wires.

Note that the narrow FWHM gives, in addition, evidence for a good alignment of the pores perpendicular to the membrane surface. This property of our templates can be of great importance if homogeneous needle growth is required. Problems due to large angular distributions with tilt angles of more than 30 ° in commercially available membranes have been reported so far [72].

Chapter 6

Two methods for contacting copper nanowires

In order to investigate further properties of the nanowires, for example, electrical and magnetic, it is necessary to attach electrical contacts to single nanowires, and these contacts should be, in addition, low-ohmic. In this chapter we present two methods for contacting the copper nanowires. For the first one, large arrays of wires are produced by the template method as explained in chapters 3 and 4. Then, individual nanowires are selected by contacting them with lithographic techniques. The second method demonstrates a new possibility of creating single nanowires, that can be easily contacted for further studies. The technique is based on single-ion irradiation (technique available at the GSI, Darmstadt) and ion-track etching, in combination with electrochemical deposition.

6.1 Production of selective contacts by lithographic methods

6.1.1 Device fabrication

6.1.1.1 Experimental techniques

Optical lithography Optical lithography is the process of transferring geometric shapes on a mask to the surface of a substrate covered with a photosensitive polymer. Optical lithography, employed in industry for mass production, can fabricate structures as small as 0.2 μm. In this work, we used this technique to create metallic contacts

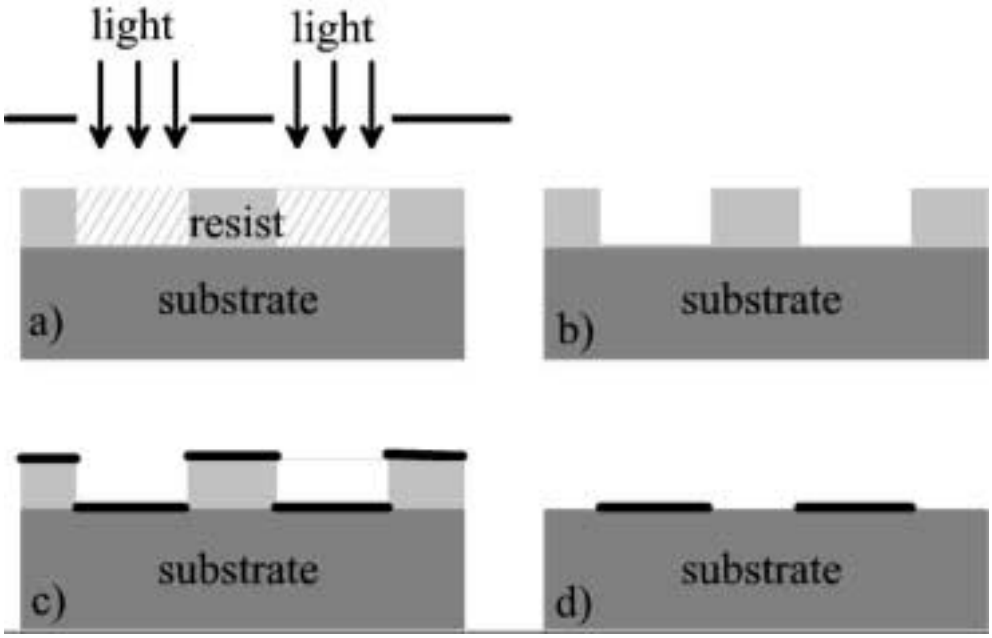

Figure 6.1: Optical lithography. a) light irradiation, b) development, c) metal evaporation, d) lift-off.

and bond pads. The minimum structure size that can be reached in the lab is $\sim 1\mu$m. To start the lithographic process, a layer of UV-sensitive photoresist is deposited on top of the substrate. By spin-coating, a homogeneous thickness and distribution of the resist on the whole sample is achieved. After baking, the sample is brought in contact with a mask and illuminated with UV-light. By using a suitable solvent, the resist can be selectively dissolved at the places where it has been illuminated. After metal deposition and lift-off, the pattern of the mask is transferred to the substrate.

Electron beam lithography Electron beam lithography (EBL) is a widely used technique in mesoscopic physics. It enables to produce structures in the submicrometer range in a very efficient way. In analogy to optical lithography, in EBL also a polymeric resist is spun on a substrate. Instead of using a mask, the electron beam is employed directly to write any structure on the sample. The polymeric chains, which form the resist are modified at the sites irradiated by the electrons, therefore the polymer can be subsequently dissolved from these positions. Again like in optical lithography, metal evaporation and lift-off transfer the pattern to the substrate. The electron beam is controlled by commercial software, thus allowing one to design a great variety of

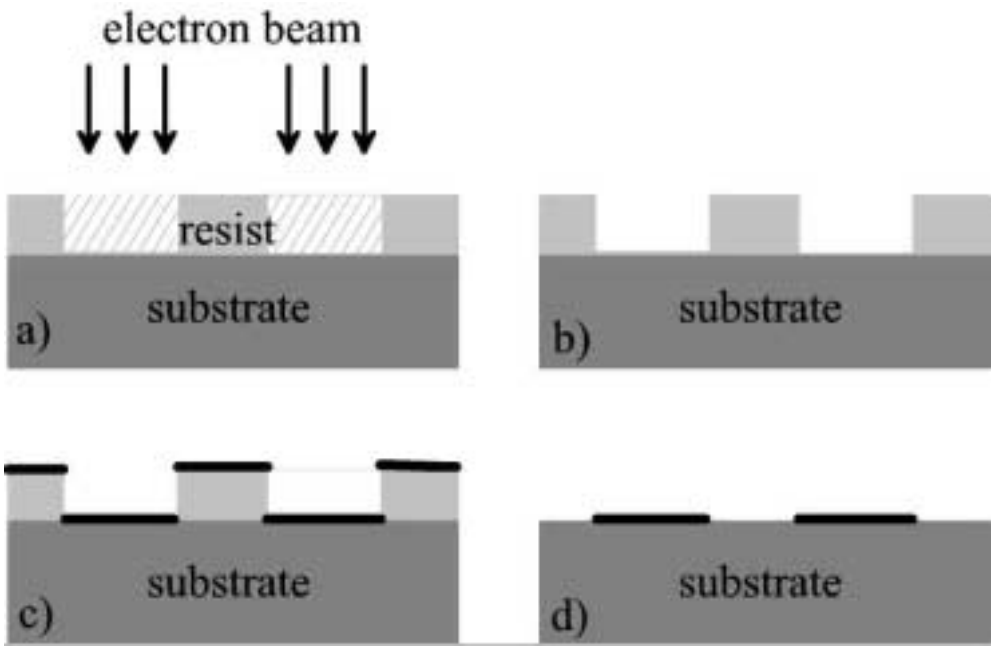

Figure 6.2: Electron beam lithography. a) electron exposure, b) development, c) metal evaporation, d) lift-off.

structures. The production is, thus, slower than by other techniques as UV- or x-ray lithography, for which the use of a mask allows a parallel mass production.

Evaporation of a metal Evaporation is a suitable method to deposit a thin homogeneous layer of metal on the surface of a material. In particular, it is suitable in the case of Au, Ni and Cr, metals of relevance for this work. This step is performed after each of the lithographic approaches employed in this work, EBL or OL. The evaporation takes place in a chamber under vacuum. The metals to be deposited were placed on holders consisting of a material of very high melting point, in our case tungsten, which are heated by an electrical current. The atoms are thus thermally emitted in all directions, and deposited as a thin film on the sample. The thickness of the deposited material is controlled within 0.3 nm and the evaporation rate can be also adjusted. The sample holder can be rotated and tilted.

6.1.1.2 Fabrication of the metallic contacts

The metal contacts were produced by two different processes, one employing exclusively optical lithography, and the second one combining both EBL and optical lithography. For the creation of microcontacts, it is of extreme importance that the substrates are free of any kind of contamination. Prior to their use, the substrates are carefully cleaned and the subsequent production process is performed in a "clean-room".

Optical lithography In this case, we used pieces of monocrystalline Si-wafers as substrates. The wafer surface was covered with a 400 nm SiO_2 layer by thermal oxidation and subsequently polished, becoming thus more suitable for the deposition of the wires and further processing steps. Then, in order to create the contacts to the wires and the bondpads, a layer of UV-sensitive photoresist (Shipley 1305) of about 0.5 μm of homogeneous thickness is spun onto the sample, and subsequently baked in an oven over 30 minutes at 90 °C. Then, the sample is pressed against a chromium mask. In Fig. 6.3 both the employed mask (a) as well as a detail of an individual contact (c) are depicted schematically. On each sample, an average of 10 times 10 contacts were created, being numbered as 1.1, 1.2, ... , 2.1, 2.2, ... ,10.10. After irradiation with UV-light over 12 seconds, the structure is developed for also 12 seconds. The developing process is stopped in water. At this point, we have to transfer the structure created on the photoresist to a metallic layer. Both a 3 nm NiCr and a 30-60 nm gold layer were evaporated on the sample as well as on the remainig resist. NiCr improves the adhesion between the sample and the gold, the gold was the metal chosen for the contacts and the bondpads.

After evaporation of the metal, the sample is immersed in boiling acetone. In this way, the rest of resist is dissolved, $lifting\ off$ the metal on its top (Fig. 6.1 d). As a result, we obtain metal contacts where the sample had been previously illuminated. SEM images in Fig. 6.3 b and d show an overview of the sample and of the contact after the lithographic process.

Combination of electron beam and optical lithography We employed pieces of GaAs as substrates, which were carefully cleaned prior to their use. Once the substrate is clean, a PMMA layer is spun on the substrate surface and baked. After that, the samples are transferred to the SEM, and the structures are written with the electron beam. The EBL structure pattern employed in this work is shown in Fig. 6.4 a. Before mounting the sample for metal evaporation, the structure is developed in MIBK (methylisobutylketon) during 50 seconds. Then, a layer consisting of 3 nm

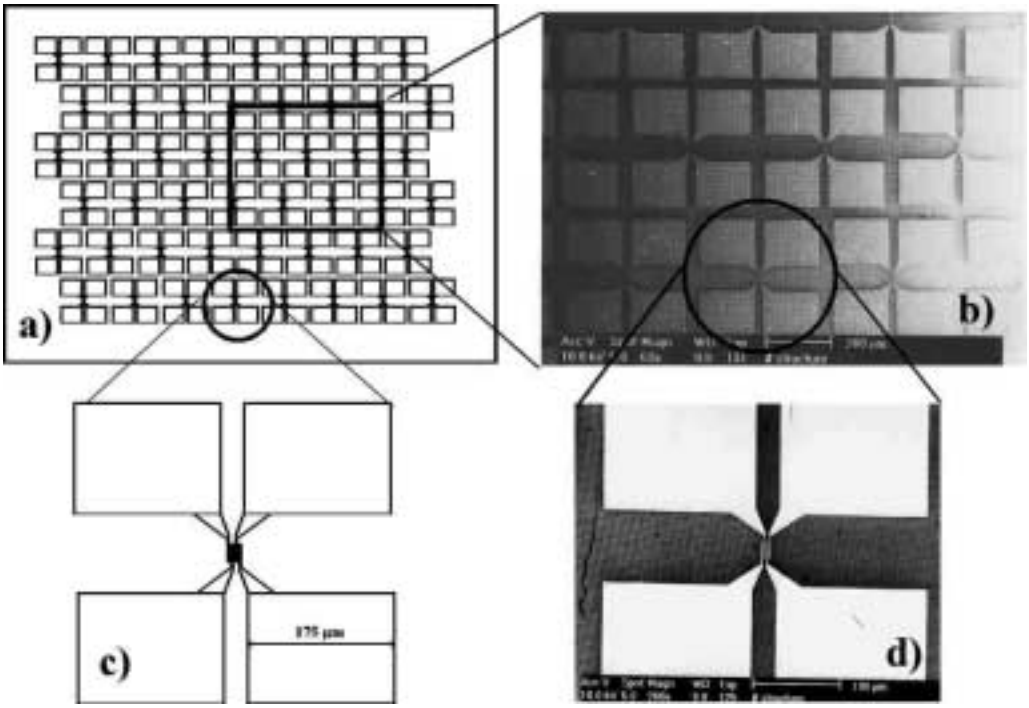

Figure 6.3: a) Schematic of the distribution of the structures created by optical lithography including contact fingers and bonding pads, b) SEM picture showing four of the contact structures, c) Schematic and d) SEM image of one individual contact structure. Each finger is 1 μm thick, the distance between two consecutive contacts is 2 μm, and the dimensions of the bond pads are 175 μm.

NiCr and 60 nm Au is evaporated. The resulting structure after the $lift\ off$ process is presented in Fig. 6.4 b. After production of the contacts and deposition of the wires (see next section), each sample is carefully observed with SEM, noting the positions of the structures which have successfully contacted wires. On those structures, bond pads are selectively created by optical lithography.

The two different processes have several advantages and disadvantages. Thus, for example, while by optical lithography we are able to create many structures in parallel, thus increasing the velocity of preparation of the samples, by EBL we are more flexible to design structures, and higher resolution is achieved. We mostly employed optical lithography because the number of lithographic steps together with the considerable number of processing steps to which the wires have to be exposed to (e.g. spinning the resist, baking in the oven, or boiling in acetone) is lower, and the time devoted to the preparation process of the samples is shorter. Since the distance between electrodes in which we were interested for the first measurements was above 1 μm, optical lithography did not result in a loss of resolution either.

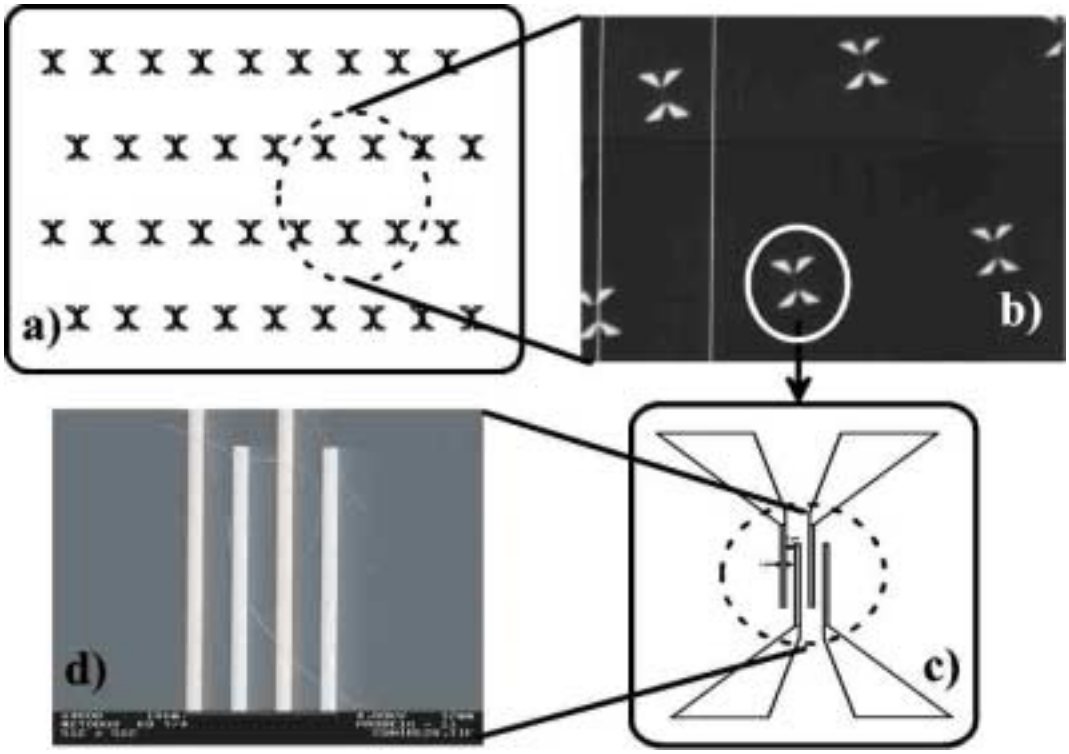

Figure 6.4: a) Schematic of the distribution of contact fingers created by electron beam lithography, b) SEM picture showing four of the contact structures, c) Detailed schematic of one structure. Each finger is 1 μm thick and the distance between two consecutive contacts is 2 μm, d) SEM image of the fingers.

6.1.1.3 Preparation of the wires

To contact the copper wires by lithographic methods, the wires should be polymer-free. For this purpose, the polymer membrane containing the wires is dissolved in dichloromethane, exchanging the solvent several times. In the case of wires of extremely small diameters (under 200 nm) and samples with a high areal density of wires ($5 \cdot 10^8$ wires/cm^2), polymer rests remain on the surface of the wires when they are still fixed to the copper bottom. In order to obtain free clean wires, they were detached from the bottom by placing the vessel in an ultrasonic bath. Centrifugation is applied to the resulting solution containing free wires. After 15 minutes at 2000 rpm, the wires are concentrated on the bottom of the centrifugation glass, as shown in Fig. 6.5 (left). Then, the solution above the wires is exchanged with a pipette and the glass is introduced with the new solution in the ultrasound bath. After this process, the

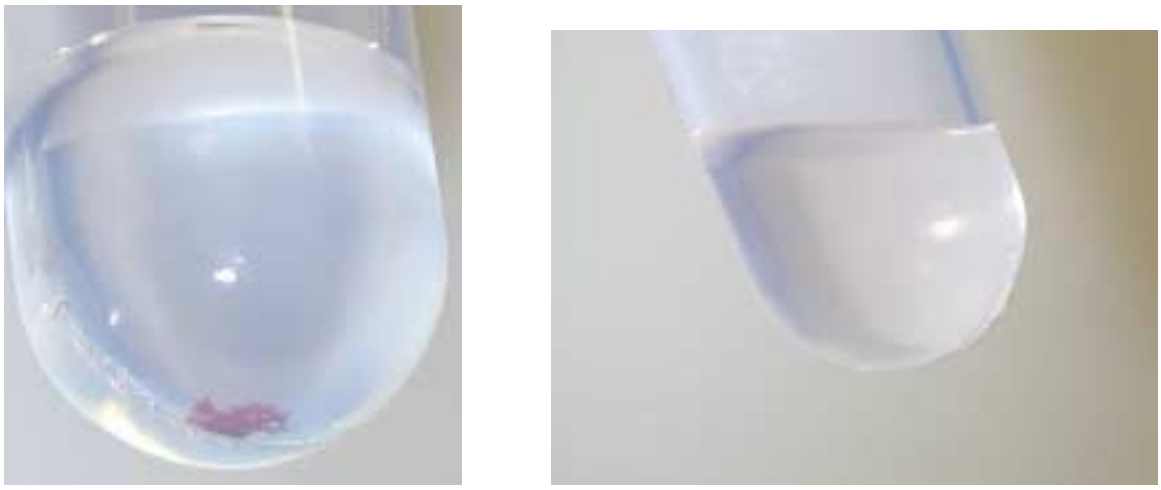

Figure 6.5: Pictures taken (left) after centrifugation and (right) after ultrasound.

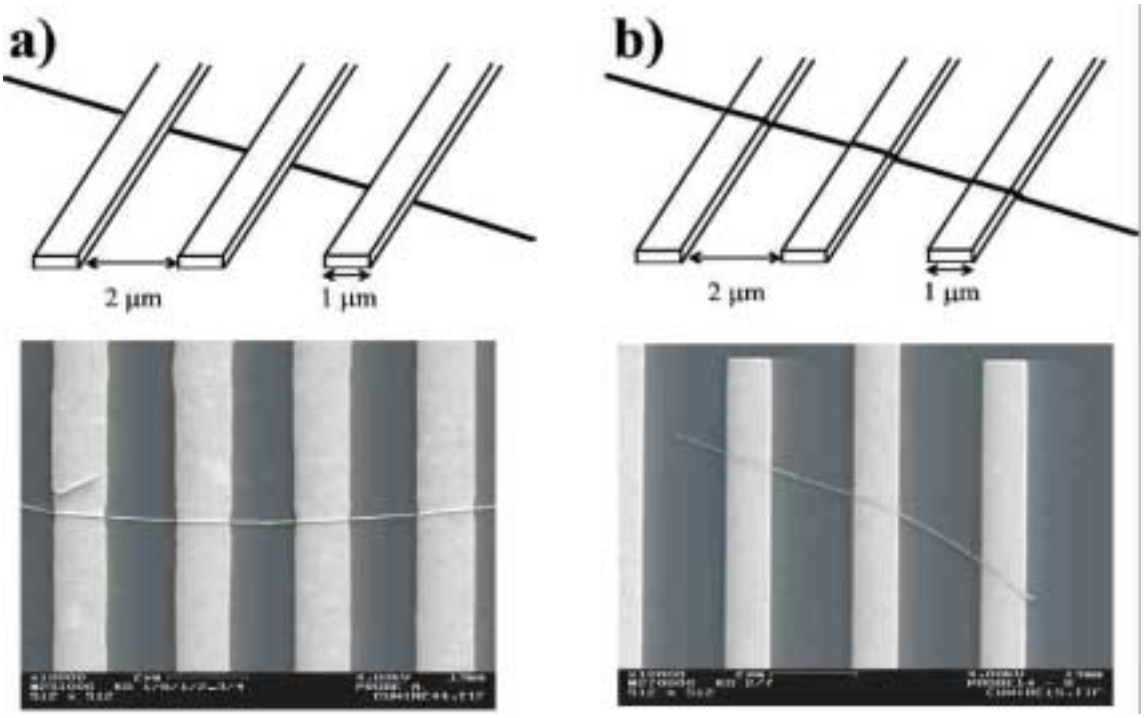

Figure 6.6: Two techniques to attach metallic contacts to the copper nanowires. a)electrodes are fabricated above the nanowires, b) the wires are deposited on the prefabricated contacts.

wires are homogeneously distributed in the solution, as depicted in Fig. 6.5 (right). By repeating this procedure several times, the wires are cleaned efficiently.

At this stage, the wires are prepared to be brought onto the substrate and contacted. We employed two methods in order to attach the wires to the gold contacts. When applying the first method (Fig. 6.6 a), the wires are first brought onto a SiO_2 substrate. For that purpose, some drops of the solution of dichloromethane containing the wires (Fig. 6.5) are deposited on the substrate. Then, the dichloromethane evaporates and an array of contacting structures consisting always of four fingers is fabricated on top. The wires, in this way, lie under the gold contacts. In the second method (Fig. 6.6 b), we create an array of contacting structures directly on a substrate, and then bring the wires on top of the contacts.

In both cases, the density of wires on the substrate was controlled by varying the concentration of wires in the solution and the number of drops deposited on the substrate.

6.1.2 Electronic set-up

After careful examination of the contacts by SEM, the chip is glued onto a chip-carrier, and the contacted wires are bonded ultrasonically with thin aluminium wires, thus becoming available to the external electronic. The sample is then inserted into a socket for further measurements.

Since the number of wires placed under two contacts was much higher than the number of wires contacted by four gold fingers, the measurements were performed in a two-point geometry, as presented in Fig. 6.7. We applied a constant voltage to the wires and we measured the current, by employing an I-V converter, with picoampere resolution. Voltage and current were continuously recorded. The electrical circuit is presented in Fig. 6.7.

First experiments were performed at room temperature to check the existence of contact between the wires and the gold pads. In some cases also low temperature measurements were performed. For this purpose, the sample holder was evacuated and filled with some exchange gas He to improve the heat exchange between sample and He. For temperatures at T = 4.2 K, the sample can be directly inserted in the liquid Helium container.

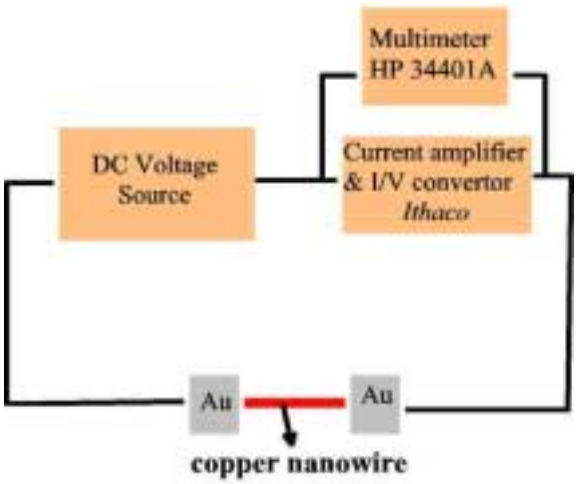

Figure 6.7: Electronic set-up for the I-V measurements on copper nanowires.

6.1.3 Measurements

Contacts As explained in section 6.1.1.3 the gold contacts can be created on top of the wires or, alternatively, the wires can be brought to a substrate on which the gold contacts have been previously fabricated (Fig. 6.6). When the wires were deposited on the prefabricated gold contacts (Fig. 6.6 b), we measured in all cases resistances of the order of GΩ. One reason for these high values is that the wires may touch the electrode only at some points, causing a high and indeterminate contact resistance. Another contribution to the high resistances may be the presence of an adsorbate layer between the gold contacts and the wires, which would avoid the existence of a good contact [98].
All curves shown in this section are therefore performed on samples where the copper wires are lying directly on the substrate, under the gold electrodes. This method provided a better contact between wires and the gold fingers, because the contact surface between the gold electrodes and the wires is very big in comparison to the diameter of the wires, and is well defined (Fig. 6.6 a). Moreover, when the wires lie directly on the substrate, they are completely straight avoiding the mechanical deformations caused when the wires lie on the gold fingers.

I/V characteristic of a 50 nm diameter copper wire Fig. 6.8 shows a SEM image of gold electrodes patterned on a 50 nm diameter copper nanowire. The electrodes are separated by 2 μm.

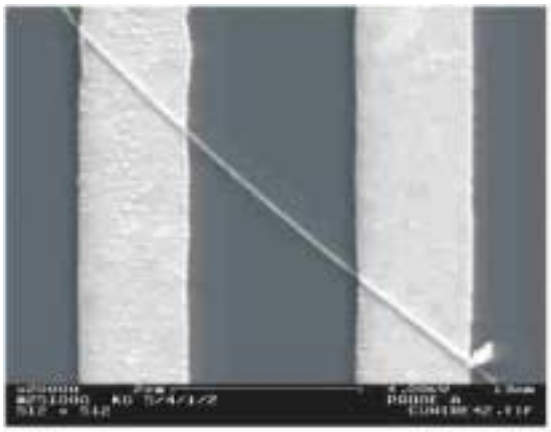

Figure 6.8: SEM image of Au electrodes patterned on a 50 nm diameter copper nanowire. The electrodes are separated by 2 μm.

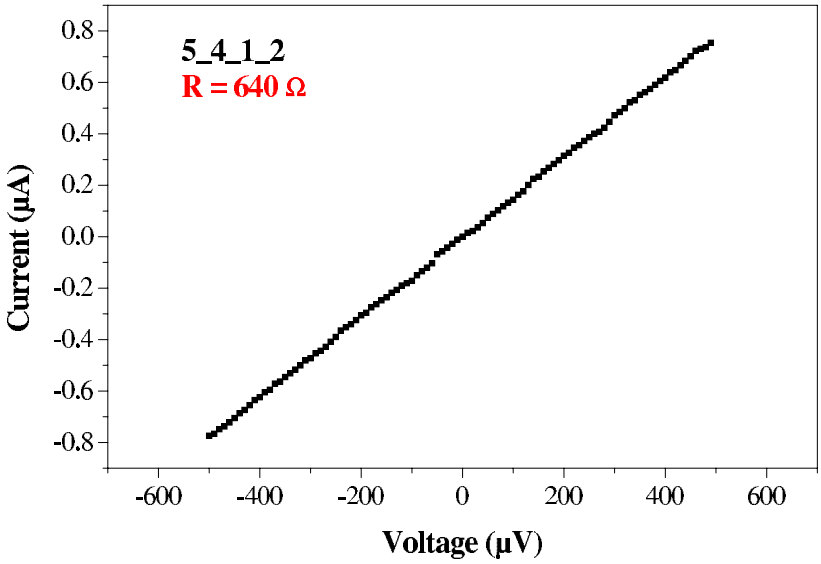

Figure 6.9: 2-probe I-V characteristic at room temperature of the wire depicted in Fig. 6.8.

The 2-probe I/V characteristic of the 50 nm diameter copper nanowire is displayed in Fig. 6.9. The curve shows a linear symmetric behaviour, corresponding to a resistance of 640 Ω. Though through this contact configuration ohmic resistance is much lower than when the wires are placed on the gold electrodes, the resistance is higher than expected when considering the bulk resistivity of copper at RT ($\rho = 1.7 \cdot 10^{-6}$ Ω cm). In this case, the resistance of a 2.4 μm long, 50 nm diameter copper wire should be $\sim$ 20 Ω, i.e. about 30 times smaller. There are several possible explanations for this

result:

- The contact resistance is high. Unfortunately, to check this assumption it is necessary to perform a 4-probe measurement and the wire only has two contacts but, as explained just above, due to the big and well defined contact surface existing between the gold fingers and the copper wires, the contact resistance is expected to be very low. For example, contact resistance values below 100 Ω have been reported by other authors [99].

- The resistivity of copper wires of small diameter is higher. This possibility is supported by other works [25, 100], in which the authors measured a higher resistivity than its bulk value for Au wires of 350 nm in diameter, and attributed it to a possible increase in surface scattering. For wires of such small diameters the surface/volume ratio is much higher, and a higher influence of the surface scattering of electrons can be expected.

- The resistance increases due to an oxidation of the wires. Since the measurements at RT were performed in air, a superficial oxidation of Cu to Cu_2O at room temperature, as well as further oxidation processes favoured by the high temperatures reached by the wire during the measurements (Joule heat), could explain an increase of resistance after a certain time. Due to the small dimensions of the wires, even small amounts of oxidation may have a large effect on the transport characteristics, in this case, on the resistance of the wire.

Oxidation of the copper wire A series of curves measured successively during several hours (Fig. 6.10), indicates a continuous increase of the resistance of the wire depicted in Fig. 6.8. Within several hours, the resistance increased from 640 Ω (curve shown above on a more expanded voltage scale) to several MΩ.

Due to the extremely high surface to volume ratio of these nanowires, it is very probable that oxidation has a marked effect (larger than on macroscopic structures) on the wire resistance. In our case the oxidation process may be favoured by a temperature increase of the wire as the electrical current flows through it, since the temperature of a 50 nm diameter copper wire could easily increase at a current of the order of 1 μA (Joule effect). Further experiments and additional analysis of the samples is needed after the I/V measurements to confirm their oxidation as well as to determine the type of oxide.

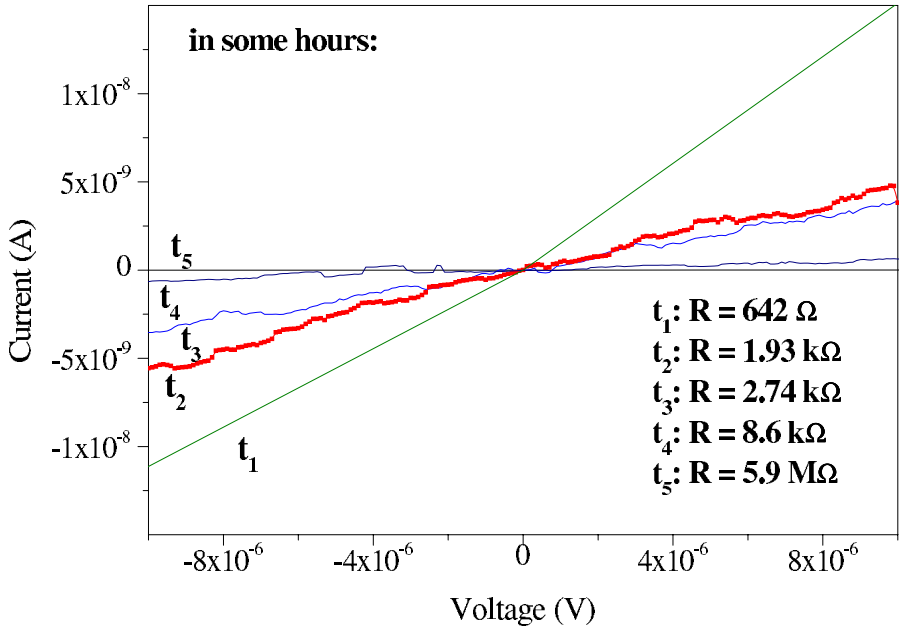

Figure 6.10: Series of I/V curves measured succesively for some hours on the wire shown in Fig. 6.8. The resistance increases progressively.

A large amount of data and results of investigations on the oxidation of copper at different temperatures and oxygen partial pressures can be found in the literature [101, 102, 103]. These results show, however, strong discrepancies, which can be in part explained by the big influence that sample and environment have on the corrosion behaviour of metals. Thus, for example, it is well known that the thickness and the distribution of the oxide film depend on the morphology and crystallinity of the sample, and that oxidation takes place preferentially at defects contained in the structures as well as at the grain boundaries of polycrystalline materials [101]. Therefore, an analysis of our samples would have to be performed in particular to characterise the oxidation process.

Generally, two components are usually formed during oxidation of copper in air, namely Cu_2O and CuO [104]. For oxidation of 80 nm thin copper films at $T \leq 300$ °C in air, correlations between the change in resistance and the kinetic process of oxidation have been reported in [104]. They found that Cu was first oxidized to Cu_2O at 200 °C, and then to CuO at 300 °C near the surface. The inward diffusion of oxygen proceeded gradually as a function of the annealing time. A 500 nm thick oxide layer was formed after annealing a copper film for four minutes in air at T = 350 °C [102]. Oxidation of copper at high temperatures is, in addition, a well known problem for the use of copper in the microelectronics industry, which has become more evident in the case of

smallest structures.

Results similar to our observations have been reported for Mo nanowires in [12]. After measuring a resistance higher by a factor of 10 of a 380-nm-diameter Mo wire two hours after preparation, and by a factor of 300 of a 480-nm-diameter wire 48 hours after preparation, they concluded that the surface of the Mo wire was converted by air oxidation to nonconductive MoO_x on the time scale of a few hours.

Non-linear characteristic After the increase of resistance, some hours after starting the measurements, the I/V characteristics measured on the same wire, applying several volts, are symmetric and non-linear, as depicted in Fig. 6.11.

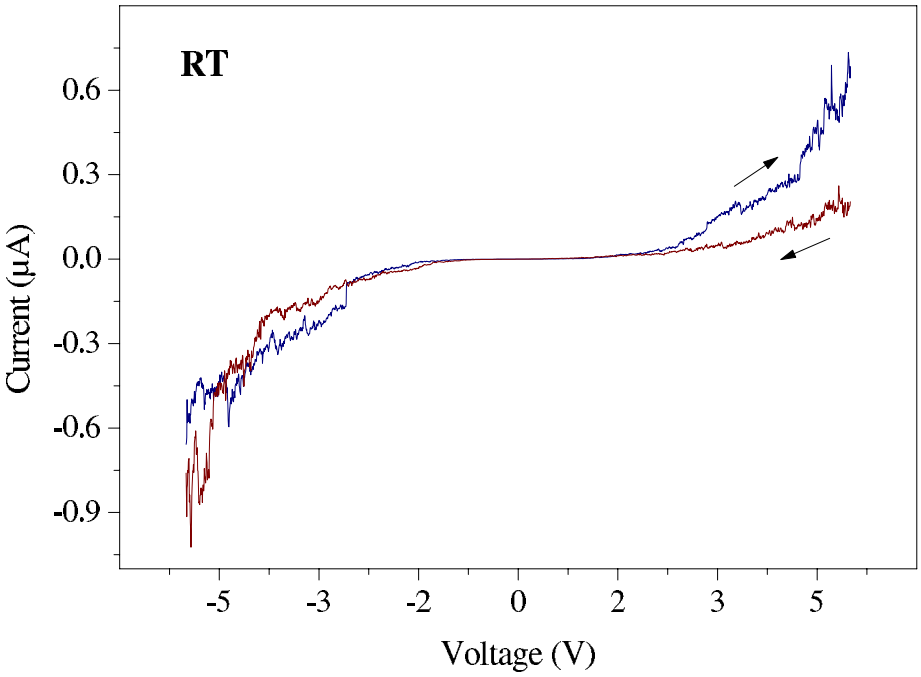

Figure 6.11: Nonlinear I/V characteristic of the 50 nm diameter wire shown in Fig. 6.11, measured after some hours. The arrows indicate the direction in which the voltage was scanned.

The curve can be preliminarily explained as the I/V characteristic of a metal-semiconductor-metal junction, which would correspond to two Schottky diodes which are placed back-to-back. If we assume that the copper wire is completely oxidized after some hours of measurements, and knowing that Cu_2O is an oxide semiconductor (type p), the electrode configuration on the copper wire as shown in Fig. 6.8 is equivalent to a metal-semiconductor-metal junction. (The semiconducting mechanism of Cu_2O is

described in detail in [105]).

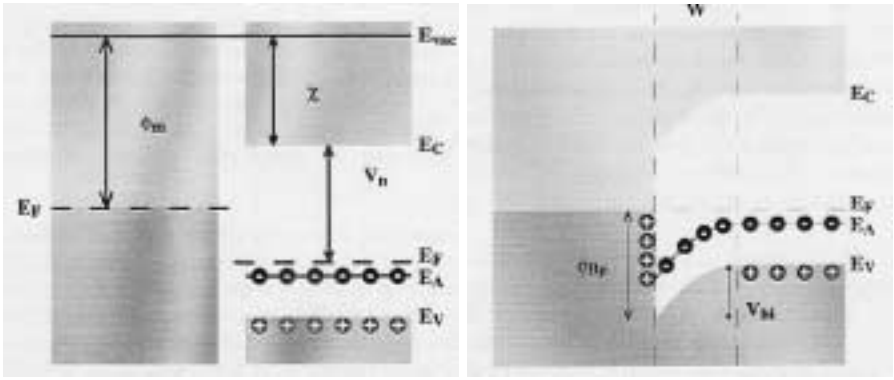

Figure 6.12: Situation of a Schottky barrier between a metal and a p-type semiconductor a) before contact, b) after contact.

The contact between a metal and a semiconductor surface is known as a Schottky barrier. Figure 6.12 shows the situation of a Schottky barrier of a metal and a p-type semiconductor. Before contact (Fig. 6.12 a), the Fermi level is higher in the metal. Therefore, after contact (Fig. 6.12 b), electrons will flow from the metal to the semiconductor. This causes a build-up of charges on both sides of the interface, resulting in an electrical field and a potential gradient, the so-called *band bending*. Finally, at the interface, in the so-called depletion region, there is a surplus of negative charge or uncompensated charge acceptors. The application of a forward bias (positive voltage applied to the p-type semiconductor and negative to the metal) compensates the band bending, thereby reducing the Schottky barrier and leading to the occurrence of a current. Reverse bias increases the barrier, leading to a current, whose value is independent of the applied voltage until a certain voltage value, called breakdown voltage, is reached. The value at which breakdown occurs depends on the characteristics of the semiconductor material.

When two Schottky diodes are placed back-to-back, the potential applied across the entire structure will be divided into two components, V_{for} on the forward biased diode and V_{rev} on the reverse. Since the current that flows through both juctions must be the same, and since the resistance of the forward biased diode is much smaller than the reverse, the net I/V characteristic will resemble the characteristic of the diode under reverse bias. For each polarity, one of the Schottky diodes will be reversed.

This behaviour is reflected in the curve shown in Fig. 6.11. The curve corresponds,

at positive as well as at negative applied voltages, to the I/V characteristic of a reverse biased diode, with a breakdown voltage of U $\geq$ 2 V. Since both Schottky contacts are in our case very similar, the curve is symmetric. Fig. 6.13 depicts the I/V characteristics of the MSM contact at two different temperatures, namely at room temperature and at 4.2 K. It is known that some Schottky contacts have positive and some have negative temperature coefficients. In the first case, this is due to impact ionization (avalanche breakdown) and in the second case to defect-assisted tunnelling through surface or bulk states [106]. The graphs illustrate that our samples behave in the second way, i.e., they possess a negative temperature coefficient, showing a decrease of the breakdown voltage at higher temperatures.

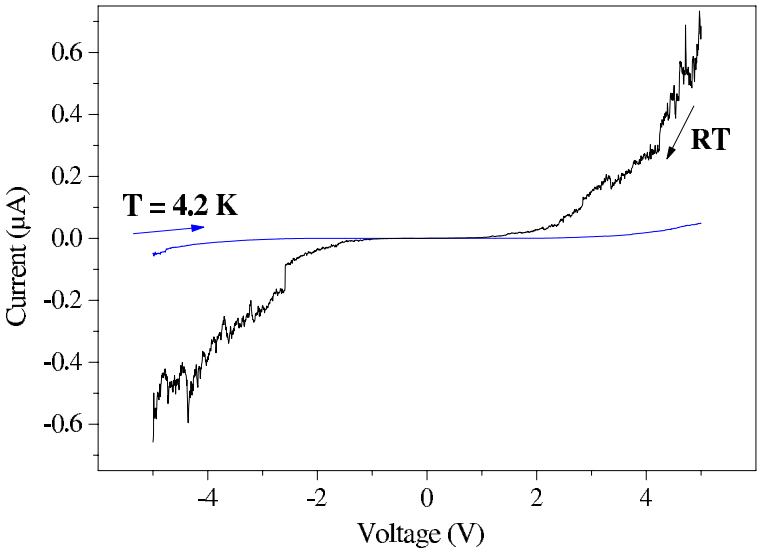

Figure 6.13: Nonlinear I/V characteristic of the 50 nm diameter wire, measured at two different T.

Further experiments will provide more information and will allow the performance of complementary measurements to confirm and complete these first results.

Appearance of the wire after the measurements The curve depicted in Fig. 6.14, illustrates the variation of the current when the applied voltage is varied between 9 and -9 V at 4.2 K. At U $\approx \pm 9$ V the current density is approximately ≈ 40 kA/cm^2. After several scans of the voltage, the current became very unstable and suddenly dropped to zero, indicating that the wire had failed. Fig. 6.15 shows the SEM image of the failed copper nanowire. The failure point is located at the center of the wire, as reported in earlier works for very thin wires [107].

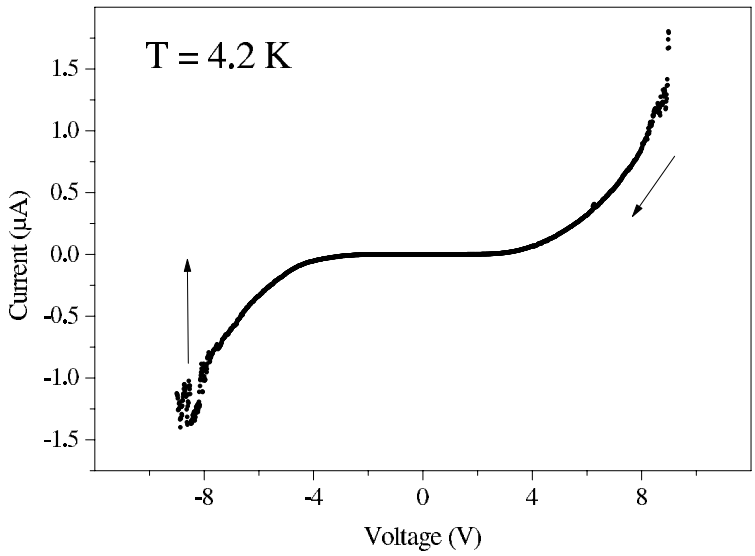

Figure 6.14: Non-linear I/V characteristic of the 50 nm diameter shown in Fig. 6.8 wire before breaking.

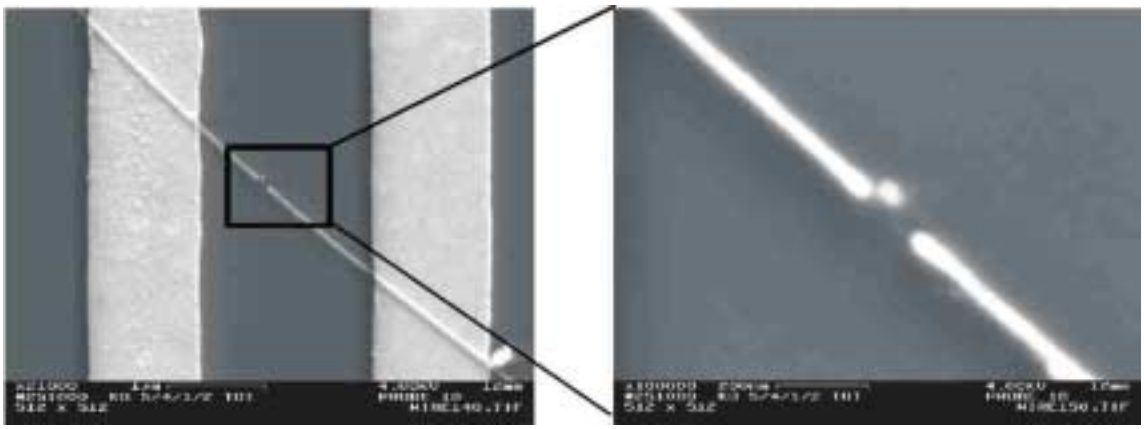

Figure 6.15: SEM image of the 50 nm diameter wire shown in Fig. 6.8 after the measurements.

I/V characteristic of a 60 nm diameter wire Fig. 6.16 shows a SEM image of a 60 nm copper wire contacted under two gold electrodes. The I/V characteristics at RT and at 4.2 K were measured within a short time, just after starting the mesaurements, and are presented in Fig. 6.17. At room temperature, the resistivity calculated for a 60 nm diameter wire of length 2.3 μm is by a factor of 10 bigger than expected for macroscopic copper. This result is an indication that, as in [12], when the measurements are performed within a short time, the wire shows metallic behaviour, i.e., it is not yet oxidised. Besides, it proves the low-ohmic character of the contact resistances.

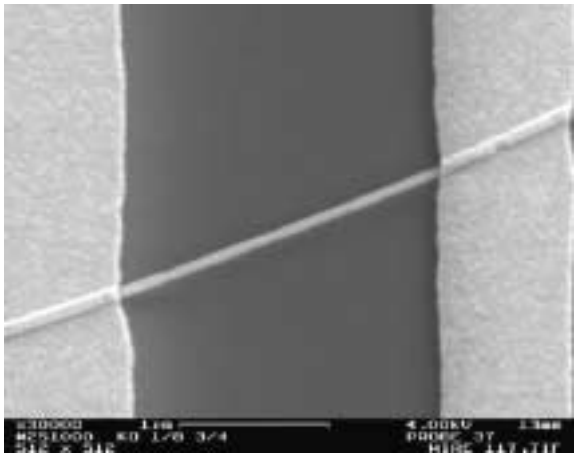

Figure 6.16: SEM image of Au electrodes patterned on a 50 nm diameter wire. The electrodes are located at a distance of 2 μm.

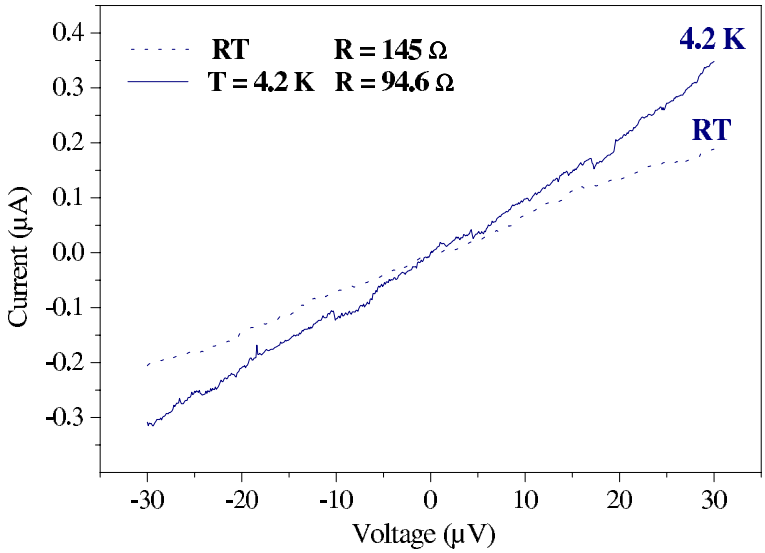

Figure 6.17: Linear I/V characteristics at RT and 4.2 K of the copper nanowire shown in Fig. 6.16.

Important is the dependence of the resistance on the temperature in comparison with the results shown in Fig. 6.13, measured for sample 5-4-1-2.

For copper oxide, the curves are non-linear and displaced towards lower voltages at higher T. In contrast to this fact, the copper wire, before oxidating, behaves metallic, its resistivity decreases at lower temperatures, and the curves are linear. This result shows that, if preventing oxidation, the contacting method is suitable for contacting nanowires in a reliable way.

6.1.4 Conclusions and outlook

It has been proved that the production of metallic contacts by lithographic methods on copper wires lying on a substrate is suitable for contacting nanowires. The contact surface between metal and wire has well defined and large dimensions, producing low-ohmic contacts. The experiments performed were necessary to find out the preparations indispensable for a sucessful contacting of the wires, as for example:

- to elucidate the procedure for the total dissolution of the polymeric membrane in order to obtain clean copper wires;
- to choose the best lithographic process and to find in each case the correspondent parameters for the lithographic steps;
- to find the best contact configuration: deposition of metallic contacts above the wires provides much lower contact resistances;
- to introduce the samples in vacuum or He atmosphere before the measurements;

After the appropriate conditions were found, first measurements have been performed, recording I/V characteristics of single copper nanowires of 50 nm diameter. Though the first curves showed the expected metallic behaviour (linear symmetric characteristics), an increase of the resistance after a certain time indicated a possible oxidation of the wires. The non-linear curves measured at higher voltages have been tentatively related to the semiconductor behaviour expected for copper oxide wires (metal-semiconductor contact). Finally, the wire was imaged by SEM after failure.

In order to perform systematic measurements of the transport properties of single nanowires, their oxidation should be prevented. Some degree of isolation of the structure from the environment (for example the use of a protective film) can be provided. The heating of the wire due to the Joule effect should be also controlled. Such measures would guarantee that the method is suitable to perform systematic measurements of the resistivity of copper as a function of several parameters as e.g. diameter, length, aspect ratio or crystallinity. Another possible experiment is the study of the maximum currents that can flow through wires of different characteristics (dimensions, crystallinity) before failure.

Measurements presented in this section were performed in the group of Prof. J.P. Kotthaus, at the Center for Nanoscience (CENS) at the Ludwig-Maximilians-University in Munich.

6.2 New contact method for single nanowires: electrodeposition in a single-pore membrane

Another possibility for contacting single nanowires is based on single-ion irradiation and chemical etching. The steps that have to be performed to create and contact a single copper nanowire are schematically indicated in Fig. 6.18. After creating a polymeric membrane with one single-pore in the middle, this pore can be electrochemically filled with several metals, e.g., copper. The deposition is prolonged until a cap with dimensions of several μm has grown on the top of the wire. Then, the wire is contacted by sputtering a conductive layer on the membrane surface.

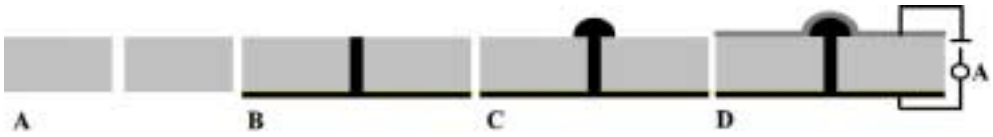

Figure 6.18: Schematic of the method employed to deposit and contact a single copper nanowire. a) Polymeric membrane created by single-ion irradiation and chemical etching, b) deposition of a conductive layer on one side of the membrane and electrochemical filling of the pore, c) growth of a cap, d) sputtering of a conductive layer on the cap.

6.2.1 Creation of a single-pore template

To produce single-pore membranes, we employed 30 μm thick polycarbonate foils. These samples were irradiated with individual heavy ions (e.g. Xe, Au, U) of several hundred MeV energy at the linear accelerator (UNILAC) of GSI. For single-ion irradiation, a mask with a 0.1 mm diameter aperture is placed in front of the sample, and the ion beam is defocused in such a way that $\sim$ 1 ion per second hits the sample. A semiconductor detector, placed just behind the sample, detects every ion passing through the foil and, by using an electrostatic chopper, the irradiation is stopped within 15 ms. With this method, samples can be irradiated with a selected number of ions ranging from 1 to several hundred.
After single-ion irradiation, the defect zone created along the ion trajectory can be preferentially dissolved in a suitable etchant. In the case of polycarbonate foils, pores

with diameters between 200 nm and 1 μm were obtained by etching the samples in 6N NaOH solution, containing 10 % vol. of methanol at T = 50 °C (Fig. 6.18 (A)).

6.2.2 Electrodeposition of a single wire

The procedure starts with the creation of a stable substrate for the growth of the wire, which provides in addition good contact with the exterior electrical circuit (Fig. 6.18(B). First, we sputtered a thin gold layer (thickness $\sim$ 100 nm) with an Edwards Sputter Coater S150 B on one side of the membrane. Then, the film was reinforced by depositing a thicker copper layer (thickness $\sim$ 20 μm) on its top. Copper was deposited galvanostatically at j = 50 mA/cm^2 at room temperature. The polymer foil was then mounted in a two-electrode electrochemical cell, schematically presented in Fig. 6.19.

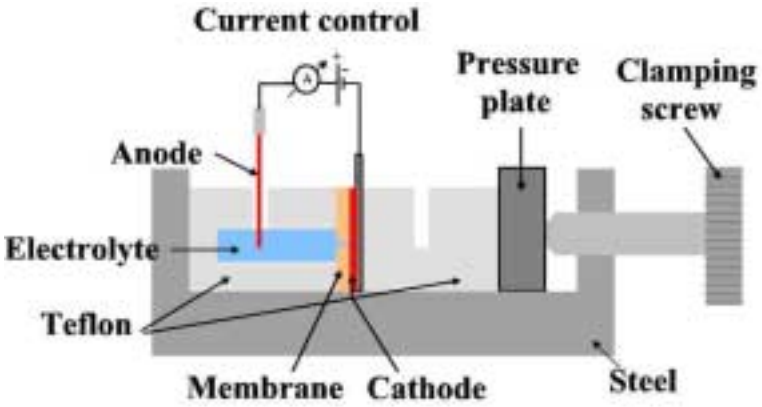

Figure 6.19: Schematic drawing of the cell employed for electrochemical deposition of single copper wires

The geometrical arrangement of the cell [108] in combination with the materials employed for its construction, provides a complete seal of the cell. This avoids losses of electrolyte, which may cause leackage currents during deposition. The conductive layer on the membrane surface acted as cathode and a macroscopic copper wire served as anode. The cell was filled with the same simple-salt electrolyte employed for the many-wire experiments, consisting of an aqueous solution containing 238 g/l $Cu_2SO_4 \cdot 5\ H_2O$ and 21 g/l sulphuric acid. The copper deposition in the pore was performed potentiostatically and at room temperature.

6.2.3 Measurements

6.2.3.1 Current-vs-time curves

Chronoamperometric curves recorded during the filling process are presented in Fig. 6.20 for various applied voltages $|\eta|$ between -100 and -120 mV. The data originate from the deposition of copper in individual 1 μm diameter pores and show the typical evolution as also observed for large ensembles of nanowires. The deposition was started only after the open-circuit voltage between cathode and anode had stabilized.

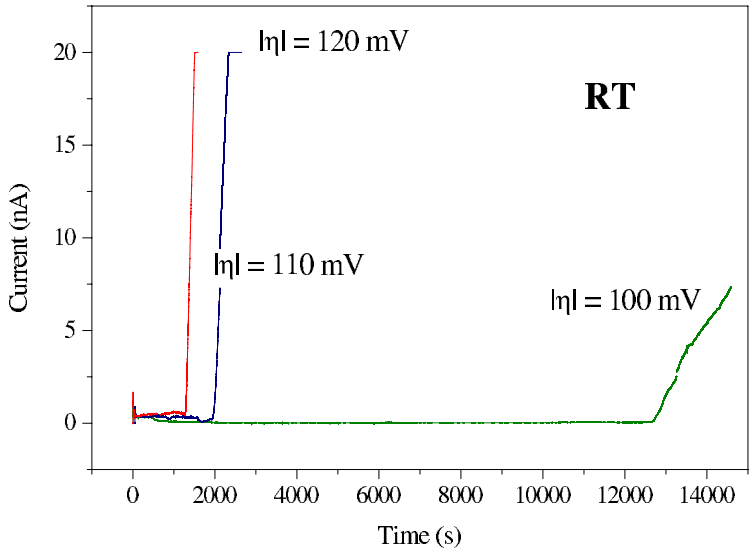

Figure 6.20: Current-vs-time curves for copper deposition in 1 μm diameter single-pore for different overvoltages applied.

When applying a potential, the current exhibits a sharp increase (I) that is ascribed to the charge of the electrical double layer. The reduction of Cu^{+2} ions directly located at the electrode surface creates a concentration gradient that causes a flux of ions towards the cathode. In this process, the decrease of current indicates the formation of the diffusion layer. During the growth of the copper wire in the pore, the current remained nearly constant (II). Then, when the wire reaches the polymer surface, deposition takes place out of the pore, forming a cap on top of the needles. Due to the increasing surface the current increases (III). We know from previous experiments that once the caps grow on the surface, the current continues to increase very slowly (IV), approaching the value necessary to deposit Cu at the same voltage on an electrode with the size of the polymer surface exposed to the electrolyte. For technical reasons, this part of the curve was not recorded. The I-t curves displayed in Fig. 6.20 reveal

these four distinct zones.
It is obvious that no difference is found between the shape of the curve for the many-pore and the single-pore systems. The qualitative behaviour is the same, inspite of the fact that when millions of pores are being filled, what we measure is an average effect. It is also shown that the higher the voltage applied between the electrodes, the higher is the current, i. e. shorter deposition times are needed (eq. 4.7), and the faster is the transition between growth of the wires and macroscopic growth on the polymer surface.
Fig. 6.21 shows the current-vs-time graph for the growth of a single 200 nm diameter nanowire. The current is in the range of pA.

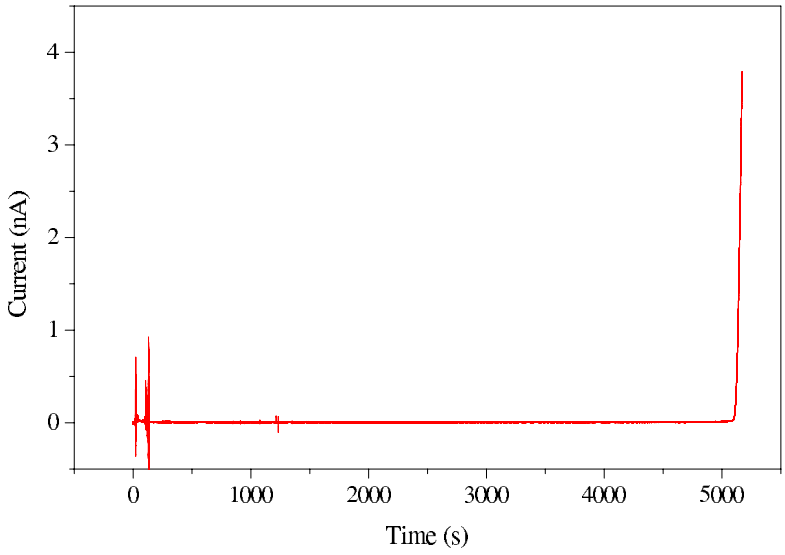

Figure 6.21: Current-vs-time curves for copper deposition in 200 nm diameter single-pore for $|\eta| = 120$ mV.

For every deposition, we calculated the integral of the current-vs-time curves between the beginning of the deposition and the transition to zone III, which coincided in every case with the charge given by Faraday's law for depositing 1 μm and 200 nm diameter copper wire, respectively. This result corroborates the diameter value expected from our etching experiments, as well as the assumption of 100 % current efficiency under the conditions employed in this experiment.

6.2.3.2 Caps

When the nanowire reached the upper membrane surface (Fig. 6.18(B)), the deposition process was continued for some time, in order to grow a copper cap of about 10 m in diameter (Fig. 6.18(C)). Caps of single nanowires grown at different overvoltages are shown in Fig. 6.22. The different morphology indicates that larger grain sizes are formed for lower voltages. This is in full agreement with the discussion in section 5.1.

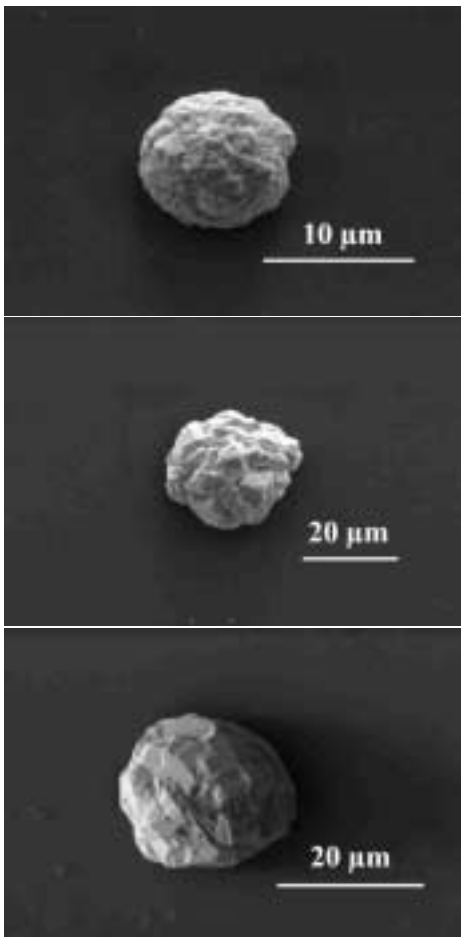

Figure 6.22: Caps grown on top of single copper wires at room temperature. Different morphologies were obtained at different overvoltages: a) deposited at -120 mV (scale bar: 10 μm), b) deposited at -110 mV (scale bar: 20 μm), c) deposited at -100 mV (scale bar: 20 μm).

6.2.3.3 Contacting

For electrical measurements, the cap and therefore the wire can easily be contacted by evaporating another metal layer (e.g. gold) on the membrane surface (Fig. 6.18(D)). Our technique eliminates the laborious procedure of selecting and contacting single wires necessary when using other methods, e.g., lithographic methods. Up to the present, it has been verified that, for samples presented in this chapter, there is contact between both sides of the membrane after deposition of the gold layer on top. Characteristic current-vs-voltage curves are planned to be measured when thinner wires are produced.

The resistance between cap and gold is expected to be negligible. Nevertheless, to prove this assumption and to check the reproducibility of the method, the contact resistance value can be obtained in an additional future experiment, in which copper could be deposited in single-pore membranes of different thicknesses. By measuring the resistance in each case, and plotting it as a function of the length, we obtain both the specific resistivity of the wire and, eventually, the value of the contact resistance. This method provides an excellent tool to measure resistivity as a function of several factors as e.g. crystallinity and diameter.

6.2.4 Conclusions and outlook

In this section we presented the first results on the deposition of a copper wire in a single-pore polymer membrane. A series of measurements has been performed at room temperature for overvoltages between -100 and -120 mV. Until now, wires as thin as 200 nm have been deposited. The curves show in all cases the four typical zones described also in the case of deposition in many-pore membranes, and the measured charge coincided in all cases with the one calculated from Faraday's law.
The next step would be to extend the method to even smaller diameters. Therefore, thinner membranes should be employed and the etching conditions have to be optimised. Caps deposited on top of the wires provide information about the crystallinity of the wire. In order to obtain single-crystalline copper nanowires, experiments at higher temperatures and lower overvoltages have to be performed.
As proposed also for the first method, series of measurements could be performed in order to investigate transport properties of single nanowires as a function of parameters such as diameter, aspect ratio, and crystallinity. By measuring the resistance as a function of the length, both specific resistance and the contact resistance between cap and gold layer can be obtained. Additionaly, the method provides the opportu-

nity of measuring electrical transport of wires embedded in a polymer. Since one of the objectives of the microelectronics industry, in order to achieve faster devices, is to find suitable materials with a low dielectric constant (mostly polymers) in which the copper structures are deposited (via filling), it would be interesting to deposit wires in different membranes and to study their electrical and mechanical properties while they are embedded in the polymer.

Chapter 7

Summary

Poly- and single-crystalline copper nanowires were produced by electrochemical deposition in etched ion-track membranes. Their structure and morphology was characterised by scanning electron microscopy, transmission electron microscopy and x-ray diffraction. Two techniques were tested to contact nanoneedles for electrical transport measurements.

Membranes with cylindrical pores were created by heavy-ion irradiation and chemical etching. We irradiated 30 μm thick polycarbonate foils with swift heavy ions. Fluences between one single ion on the whole membrane and 10^9 ions/cm^2 were used. In a chemical etching process, the latent tracks of the ions were enlarged to pores with diameters between 30 and 500 nm. A maximal aspect ratio (i.e. length over diameter) of 10^3 has been attained. Pores larger than 100 nm exhibit cylindrical geometry. For smaller pores, a variation in diameter of up to 30% along their length was observed. In order to produce cylindrical wires with diameters as small as several nm, thinner membranes have to be employed and, eventually, sensitisation of the ion tracks by exposure to UV-light should be performed before etching.

Potentiostatic deposition of copper in pores with large (several hundred nm) and small (several ten nm) diameter pores have been investigated using a two-electrode electrochemical cell. We presented the results of a systematic study aimed at determination of the optimal DC deposition parameters (overvoltage, temperature, and electrolyte solution) required for single-crystalline growth.

It is known that during electrochemical growth of the copper needles, two mechanisms occur simultaneously: i) growth of existing nuclei and ii) formation of new grains. The two processes compete with each other and are influenced by several factors (e.g, cathode overvoltage, surface diffusion, and concentration of ad-atoms). For the cre-

ation of single-crystals the first process should dominate. In this work, wires of three different samples deposited at the same current density and different temperatures from a commercial bath were observed by SEM. At room temperature, fine-grained polycrystalline wires were created. At 40 °C, the needles were still polycrystalline but with larger grains. Finally, at 60 °C, facets on the tip, corresponding to the cubic structure of Cu, indicated single-crystallinity. Since the increased temperature leads to a decrease of the cathode overvoltage, to a lower concentration of ad-atoms, and to an increase of the surface diffusion, the present studies show that these three factors favour the growth of already existing nuclei and, therefore, the deposition of single-crystals rather than the nucleation. Low overvoltages favoured also the growth of existing nuclei.

For wires with diameter smaller than 200 nm deposited from a simple-salt electrolyte, the single-crystallinity indicated by SEM was confirmed by TEM imaging and electron diffraction. Thus, from our results we can affirm that nanowires deposited at high temperatures (50 °C) and overvoltages lower than 60 mV possess a single-crystalline structure. Polycrystalline wires were obtained from depositions at room temperature or at higher overvoltages. Typical defects of single-crystals as twins and slips were also observed. X-ray diffraction experiments revealed that the single-crystalline wires created under the conditions mentioned above possess a $\langle 220 \rangle$ preferred orientation.

In addition, for deposition conditions favouring the growth of single-crystals, the recorded current-vs-time curves pointed to the homogeneity of the copper growth. The experimentally determined and the theoretically predicted charge were in good agreement within the experimental error. This was not the case for higher temperatures and lower overvoltages when the pores were either partially filled or the wires had different heights.

For deposition at low overvoltages (under 120 mV) at temperatures between room temperature and 50 °C, single-crystalline as well as polycrystalline wires exhibit the same smooth and homogeneous contour as the wall of the pores of the template. This is the result of a good quality of the etched ion tracks as well as the suitable deposition conditions which avoid that the current density reaches the diffusion limitation, and that side reactions as hydrogen evolution take place.

Aiming at measuring the electrical properties of nanowires, two different techniques for contacting the wires have been presented. In the first one, from large ensembles of wires (10^6 -10^8) individual needles were selected and contacted by lithographic techniques. It has been proven that, by fabricating the metallic contacts on top of the copper wires lying on a substrate, the contact surface between metal and wire has

well-defined and large dimensions, and low-ohmic contacts were obtained. Nevertheless, oxidation of the wires should be prevented and heating of the wire due to the Joule effect should be controlled. These problems could be avoided by using noble-metal wires.
An attractive alternative is given by the second method, which enables the contact of single wires still embedded in the template. For that, we produced membranes with one single pore and deposited copper until a cap with a size of several μm was grown on top of the wire. For electrical measurements, the cap and therefore the wire can easily be contacted by evaporating another metal layer (e.g. gold) on the membrane surface. The resistance between cap and gold is expected to be negligible. This technique has the advantage that the laborious procedure of cleaning, selecting and contacting the wire is not necessary. Besides, it enables to measure transport properties of the wires embedded in different polymers.

In the future, it should be very interesting to perform further studies on poly- and single-crystalline copper needles. We expect that the physical and chemical properties of nanowires depend on their morphology and crystallinity. For example, it is known that the electron transport and also corrosion are greatly influenced by the presence of grain boundaries. Based on the above mentioned contacting methods, transport properties through single nanowires can be studied as a function of the wire crystallinity, diameter and aspect ratio. Important information can be obtained concerning e.g. maximally possible current densities or maximum current and time this current flows before failure. Finally it should even become possible to test quantum effects if the wire dimensions reach the nanometer scale.

Bibliography

[1] Gerd Bachmann. Zukunftschancen durch Nanotechnologie. *Phys. Bl.*, 55:57–61, 1999.

[2] R. W. Keyes. Miniaturisation of electronics and its limits. *IBM J. Res. Develop.*, 44:84–88, 2000.

[3] R. Spohr. *Ion tracks and microtechnology.* Vieweg Verlagsgesellschaft, Braunschweig, 1990.

[4] M. Datta and D. Landolt. Fundamental aspects and applications of electrochemical microfabrication. *Electrochimica acta*, 45:2535–2558, 2000.

[5] C. Trautmann. Observation and chemical treatment of heavy-ion tracks in polymers. *Nucl. Instr. and Meth. in Phys. Res. B*, 105:81–85, 1995.

[6] A. Huczko. Template-based synthesis of nanomaterials. *Appl. Phys. A*, 70:365–376, 2000.

[7] C. R. Martin. Nanomaterials: A membrane–based synthetic approach. *Science*, 266:1961–1966, 1994.

[8] G. E. Possin. A method for forming very small diameter wires. *Rev. Sci. Instrum.*, 41:772–774, 1970.

[9] S. K. Chakarvarti and J. Vetter. Morphology of etched pores and microstructures fabricated from nuclear track filters. *Nucl. Instr. and Meth. in Phys. Res. B*, 62:109–115, 1991.

[10] P. C. Searson, R. C. Cammarata, and C. L. Chien. Electrochemical processing of metallic nanowire arrays and nanocomposites. *Journal of Electronic Materials*, 24:955–960, 1995.

[11] X. Duan, Y. Huang, Y. Cui, J. Wang, and C. M. Lieber. Indium phosphide nanowires as building blocks for nanoscale electronic and optoelectronic devices. *Nature*, 409:66–69, 2001.

[12] M. P. Zach, K. H. Ng, and R. M. Penner. Molybdenum nanowires by electrodeposition. *Science*, 290:2120–2123, 2000.

[13] C. Z. Li and N. J. Tao. Quantum transport in metallic nanowires fabricated by electrochemical deposition/dissolution. *Appl. phys. Lett.*, 72:894–896, 98.

[14] S. Liu, J. Yue, and A. Gedanken. Synthesis of long single-crystalline nanowires from AgBr nanocrystals. *Adv. Mater.*, 13:656–658, 2001.

[15] S. Liu and J. Zhu. Carbon nanotubes filled with long continuous cobalt nanowires. *Appl. Phys. A*, 70:673–676, 2000.

[16] A. M. Morales and C. M. Lieber. A laser ablation method for the synthesis of crystalline-semiconductor nanowires. *Science*, 279:208–211, 1998.

[17] Y.-H. Lee, Y.-T. Jang, D.-H. Kim, J.-H. Ahn, and B.-K. Ju. Realisation of gated field emitters for electrophotonic applications using carbon nanotube line emitters directly grown into submicrometer holes. *Adv. Mater.*, 13:479–482, 2001.

[18] D. N. Dadydov, P. A Sattari, D. Almawlawi, A. Osika, T. S. Haslett, and M. Moskovits. Field emitters based on porous aluminum oxide templates. *J. Appl. Phys.*, 86:3983–3987, 1999.

[19] G. Fasol. Nanowires: Small is beautiful. *Science*, 280:545–546, 1998.

[20] S. Dubois, A. Michel, J. P. Eymery, J. L. Duvail, and L. Piraux. Fabrication and properties of arrays of superconducting nanowires. *J. Mater. Res.*, 14:665–671, 1999.

[21] S. Dubois, C. Marchal, J. M. Beuken, L. Piraux, J. L. Duvail, A. Fert, J. M. George, and J. L. Maurice. Perpendicular giant magnetoresistance of NiFe/Cu multilayered nanowires. *Appl. Phys. Lett.*, 70:396–398, 1997.

[22] J. I. Pascual, J. Mendez, J. Gomez-Herrero, A. M. Baro, N. Garcia, U. Landman, W. D. Luedtke, E. N. Bogachek, and H. P. Cheng. Properties of metallic nanowires: From conductance quantization to localisation. *Science*, 267:1793–1795, 1995.

[23] Electrochemical microfabrication. *IBM J. Res. Devel.*, 42:1–60, 1998.

[24] J. Jorne. Challenges in copper interconnect technology: Macro-uniformity and micro-filling power in copper electroplating of wafers. *Semiconductor Fabtech - 11th Edition*, pages 267–271.

[25] C. Durkan and M. E. Welland. Size effects in the electrical resistivity of polycrystalline nanowires. *Phys. Rev. B*, 61:14215–14218, 2000.

[26] A. Correia, J.-L. Costa-Kraemer, Y. W. Zhao, and N. Garcia. Non-linear contribution to intensity-voltage characteristics of gold nanowires. *Nanostructured materials*, 12:1015–1020, 1999.

[27] R. C. Furneaux, W. R. Rigby, and A. P. Davidson. The formation of controlled–porosity membranes from anodically oxidized aluminium. *Nature*, 337:147–149, 1989.

[28] B. E. Fischer and R. Spohr. Teilchenspuren in der Mikrotechnik. II. Anwendungsbeispiele. *Naturwissenschaften*, 75:117–122, 1988.

[29] P. P. Nguyen, D. H. Pearson, R. J. Tonucci, and K. Babcock. Fabrication and characterization of uniform metallic nanostructures using nanochannel glass. *J. Electrochem. Soc.*, 145:247–251, 1998.

[30] T. Thurn-Albrecht, J. Schotter, G. A. Kaestle, N. Emley, T. Shibauchi, L. Krusin-Elbaum, K. Guarini, C. T. Black, M. T. Tuominen, and T. P. Russell. Ultrahigh-density nanowire arrays grown in self-assembled diblock copolymer templates. *Science*, 290:2126–2129, 2000.

[31] C. Trautmann, W. Brueckle, R. Spohr, J. Vetter, and N. Angert. Pore geometry of etched ion tracks in polyimide. *Nucl. Instr. and Meth. in Phys. Res. B*, 111:70–74, 1996.

[32] C. J. Brumlik, V. P. Menon, and C. R. Martin. Template synthesis of metal microtubule ensembles utilizing chemical, electrochemical and vacuum deposition techniques. *J. Mater. Res.*, 9:1174–1183, 1994.

[33] K. B. Jirage, J. C. Hulteen, and C. R. Martin. Nanotubule–based molecular–filtration membranes. *Science*, 278:655–658, 1997.

[34] B. B. Lakshmi, C. J. Patrissi, and C. R. Martin. Sol–gel template synthesis of semiconductor oxide micro– and nanostructures. *Chem. Mater.*, 9:2544–2550, 1997.

[35] Z. Zhang, J. Y. Ying, and M. S. Dresselhaus. Bismuth quantum-wire arrays fabricated by a vacuum melting and pressure injection process. *J. Mater. Res.*, 13:1745–1748, 1998.

[36] C. A. Huber, T. E. Huber, M. Sadoqi, J. A. Lubin, S. Manalis, and C. B. Prater. Nanowire array composites. *Science*, 263:800–802, 1994.

[37] D. Dobrev, J. Vetter, N. Angert, and R. Neumann. Electrochemical growth of copper single crystals in pores of polymer ion–track membranes. *Appl. Phys.*, A 69:233–237, 1999.

[38] M. J. Tierney and C. R. Martin. Transparent metal microstructures. *J. Phys. Chem.*, 93:2878–2880, 1989.

[39] W. D. Williams and N. Giordano. Fabrication of 8 nm metal wires. *Rev. Sci. Instrum.*, 55:410–412, 1984.

[40] W. Kautek, S. Reetz, and S. Pentzien. Template electrodeposition of nanowire arrays on gold foils fabricated by pulsed–laser deposition. *Electrochim. Acta*, 40:1461–1468, 1995.

[41] D. Dobrev, J. Vetter, N. Angert, and R. Neumann. Periodic reverse current electrodeposition of gold in an ultrasonic field using ion–track membranes as templates: growth of gold single–crystals. *Electrochim. Acta*, 45:3117–3125, 2000.

[42] R. M. Penner and C. R. Martin. Preparation and electrochemical characterization of ultramicroelectrode ensembles. *Anal. Chem.*, 59:2625–2630, 1987.

[43] T. M. Whitney, J. S. Jiang, P. C. Searson, and C. L. Chien. Fabrication and magnetic properties of arrays of metallic nanowires. *Science*, 261:1316–1319, 1993.

[44] C. Schoenenberger, B. M. I. van der Zande, L. G. J. Fokkink, M. Henny, C. Schmid, M. Krueger, A. Bachtold, A. Huber, H. Birk, and U. Staufer. Template synthesis of nanowires in porous polycarbonate membranes: Electrochemistry and morphology. *J. Phys. Chem.*, B 101:5497–5505, 1997.

[45] D. Dobrev, J. Vetter, N. Angert, and R. Neumann. Growth of iron single-crystals in the etched ion tracks of polymer foils. *Appl. Phys. A*, 72:729–733, 2001.

[46] D. Al-Mawlawi, C. Z. Liu, and M. Moskovits. Nanowires formed in anodic oxide nanotemplates. *J. Mater. Res.*, 9:1014–1018, 1994.

[47] C. A. Foss, Jr., G. L. Hornyak, J. A. Stockert, and C. R. Martin. Optical properties of composite membranes containing arrays of nanoscopic gold cylinders. *J. Phys. Chem.*, 96:7497–7499, 1992.

[48] M. Saito, T. Kano, T. Seki, and M. Miyagi. Microwire arrays for infrared polarizers. *Infrared Phys. Technol.*, 35:709–714, 1994.

[49] A. Blondel, J. P. Meier, B. Doudin, and J. Ph. Ansermet. Giant magnetoresistance of nanowires of multilayers. *Appl. Phys. Lett.*, 65:3019–3021, 1994.

[50] L. Piraux, J. M. George, J. F. Despres, C. Leroy, E. Ferain, R. Legras, K. Ounadjela, and A. Fert. Giant magnetoresistance in magnetic multilayered nanowires. *Appl. Phys. Lett.*, 65:2484–2486, 1994.

[51] V. P. Menon, J. Lei, and C. R. Martin. Investigation of molecular and supermolecular structure in template–synthesized polypyrrole tubules and fibrils. *Chem. Mater.*, 8:2382–2390, 1996.

[52] D. Dobrev, J. Vetter, and R. Neumann. Growth of potassium iodide single–crystals using track membranes as templates. *Nucl. Instr. and Meth.*, B 146:513–517, 1998.

[53] N. Angert and C. Trautmann. Swift heavy ion tracks in materials. *Proceedings of the 7th International Symposium on Advanced Nuclear Energy Research Recent Progress in Accelerator Beam Application (March 18-20, 1996, Takasaki, Japan).*

[54] H. Bethe. Zur Theorie des Durchgangs schneller Korpuskular Strahlen durch Materie. *Ann. Physik*, 5:325–400, 1930.

[55] F. Bloch. Zur Bremsung rasch bewegter Teilchen beim Durchgang durch Materie. *Ann. Physik*, 16:285–320, 1933.

[56] E. C. H. Silk and R. S. Barnes. *Philos. Mag.*, 4:970, 1959.

[57] J. Vetter, R. Scholz, and N. Angert. Investigation of latent tracks from heavy ions in GeS crystals by high resolution TEM. *Nucl. Instr. and Meth.*, B 91:129–133, 1994.

[58] C. Traeholt, J. Wiesner, H.-W. Zandbergen, H. Fuess, G. Wirt, and J.-G. Wen. High resolution electron microscopy of heavy-ion induced defects in superconducting bi-2212 thin films in relation to their effect on Jc. *Physica C: Superconductivity*, 268:161–172, 1996.

[59] A. Barbu, A. Dunlop, and D. Lesueur And. R. S. Averback. *Europhys. Lett*, 15:37, 1991.

[60] R. Neumann. Scanning probe microscopy of ion-irradiated materials. *Nucl. Instr. and Meth. in Phys. B*, 151:42–55, 1999.

[61] F. Ohnesorge and R. Neumann. Scanning force microscopy corrected for nm-scale sample elasticity on single latent heavy-ion tracks in polymers. *Europhys. Lett.*, 50:742–748, 2000.

[62] T. Steckenreiter. Charakterisierung von Spuren energiereicher Ionen in Polymeren, 1997. Doctoral thesis.

[63] D. Dobrev, J. Vetter, R. Neumann, and N. Angert. Conical etching and electrochemical metal replication of heavy-ion tracks in polymer foils. *J. Vac. Sci. Technol. B*, 19:1385–1387, 2001.

[64] P. Apel, Y. E. Korchev, Z. Siwy, R. Spohr, and M. Yoshida. German patent (2000) reg. nr 10044565.9. Verfahren zum Aetzen mindestens einer Ionenspur zu einer Pore in einer Membran und elektrolytische Zelle zur Praeparierung einer solchen, 2000.

[65] R. L. Fleischer, P. B. Price, and R. M. Walker. *Nuclear Tracks in Solids*. University of California Press, 1975.

[66] C. Trautmann, S. Bouffard, and R. Spohr. Etching threshold for ion tracks in polyimide. *Nucl. Instr. and Meth. in Phys. Res. B*, 116:429–433, 1996.

[67] B. E. Fischer and R. Spohr. Production and use of nuclear tracks: imprinting structure on solids. *Rev. Mod. Phys.*, 55:907–948, 1983.

[68] N. Reber, A. Wolf, H. Omichi, M. Tamada, M. Yoshida, and R. Spohr. Thermal switching of grafted single ion tracks. *Nucl. Instr. and Meth. in Phys. B*, 105:275–277, 1995.

[69] M. E. Toimil Molares, J. Broetz, V. Buschmann, D. Dobrev, R. Neumann, R. Scholz, I. U. Schuchert, C. Trautmann, and J. Vetter. Etched heavy ion tracks in polycarbonate as template for copper nanowires. *In print. Nucl. Instr. and Meth. in Phys. B*, 000:000–000, 2001.

[70] E. Ferain and R. Legras. Pore shape control in nanoporous particle track etched membrane. *Nucl. Instr. and Meth. in Phys. Res. B*, 174:116–122, 2001.

[71] P. Apel. Private communication.

[72] V. P. Menon and C. R. Martin. Fabrication and evaluation of nanoelectrode ensembles. *Anal. Chem.*, 67:1920–1928, 1995.

[73] Carl H. Hamann and Wolf Vielstich. *Elektrochemie*. Verlag Chemie, Weinheim, 3. edition, 1998.

[74] Allen J. Bard and Larry R. Faulkner. *Electrochemical methods*. John Wiley & Sons, New York, 1980.

[75] K. J. Vetter. *Elektrochemische Kinetik*. Springer–Verlag, Berlin, 1961.

[76] D. Dobrev, J. Vetter, and N. Angert. Electrochemical preparation of metal microstructures on large areas of etched ion track membranes. *Nucl. Instr. and Meth.*, B 149:207–212, 1999.

[77] J.-Cl. Puippe and F. Leaman. *Theory and Practice of Pulse Plating*. Surface Finishers Soc., Orlando, 1986.

[78] F. A. Lowenheim. *Modern Electroplating*. Wiley, New York, 1974.

[79] I. U. Schuchert. Elektrochemische Untersuchungen zur Abscheidung und zum Korrosionsverhalten von Kupfermikrostrukturen, 2000. Doctoral thesis.

[80] D. Barkley and H. Dong. Oral presentation at the 2001 International Meeting in San Francisco (Electrochemistry Society and International Socienty of Electrochemistry). Abstract.

[81] C. Schmidt. Struktur und Eigenschaften von Kupferschichten bei der Abscheidung mit hohen Stromdichten. *Galvanotechnik*, 82:3800–3818, 1991.

[82] Gmelin. *Handbuch der Anorganischen Chemie, 8. Edition*, chapter 60 Kupfer. Verlag Chemie, Weinheim, 1960.

[83] A. C. Fisher. *Electrode Dynamics*. Oxford University Press, Oxford, 1996.

[84] Christian Amatore. *Physical electrochemistry*, chapter 4: Electrochemistry at ultramicroelectrodes, pages 131–208. Marcel Dekker, Inc., New York, 1995. Hrsg.: I. Rubinstein.

[85] K. Aoki. Theory of ultramicroelectrodes. *Electroanalysis*, 5:627–639, 1993.

[86] E. Budevski, G. Staikov, and W. J. Lorenz. *Electrochemical Phase Formation and Growth*. VCH, Weinheim, 1996.

[87] H. Doi Y. Fukunaka and Y. Kondo. Structural variation of electrodeposited copper film with the addition of an excess amount of sulfuric acid. *J. Electrochem. Soc.*, 137:88–93, 1990.

[88] D. B. Williams and C. B. Carter. *Transmission Electron Microscopy (A Text Book for Materials Science).* Plenum Press, New York, 1996.

[89] C. Kittel. *Introduction to Solid State Physics.* John Willey and Sons, Canada, 1976.

[90] Deposition and images peformed by J. Vetter.

[91] M. E. Toimil Molares, V. Buschmann, D. Dobrev, R. Neumann, R. Scholz, I. U. Schuchert, and J. Vetter. Single–crystalline copper nanowires produced by electrochemical deposition in polymeric ion track membranes. *Adv. Mater.*, 13:62–65, 2001.

[92] S. Ino and S. Ogawa. Multiply twinned particles at earlier stages of gold film formation on alkalihalide crystals. *J. Phys. Soc. Japan*, 22:1365–1374, 1967.

[93] S. Ino. *J. Phys. Soc. Japan*, 21:346–362, 1969.

[94] S. Ogawa and S. Ino. *Advances in Epitaxy and Endotaxy. Chapter.4: Particular Structures of Thin Epitaxial Crystals. Multiple Twinned Particles.*

[95] A. Nohara and T. Imura. Fivefold twinned small copper crystals grown by reduction of CuI. *J. Phys. Soc. Japan*, 27:793, 1969.

[96] Maximal intensities for Cu powder sample obtained from the JCPDS Data base, Copyright (C) 1996.

[97] X. Ye, M. De Bonte, J. P. Celis, and J. R. Roos. Role of overpotential on texture, morphology and ductility of electrodeposited copper foils for printed circuit board applications. *J. Electrochem. Soc.*, 139:1592–1600, 1992.

[98] J. Muster, G.T. Kim, V. Krstic, J. G. Park, Y. W. Park, S. Roth, and M. Burghard. Electrical transport through individual vanadium pentoxide nanowires. *Adv. Mater.*, 12:420–424, 2000.

[99] A. Bachtold. *Proceedings of the XII th International Winterschool on electronic properties of novel materials. Edited by H. Kuzmani, J. Fink, M. Mehring and S. Roth, 65 (AIP- New York 1998)*, 1998.

[100] P. A. Smith, C. D. Nordquist, T. N. Jackson, and T. S. Mayer. Electric-field assisted assembly and alignment of metallic nanowires. *Appl. Phys. Lett.*, 77:1399–1401, 2000.

[101] Gmelin. *Handbuch der Anorganischen Chemie.* Chapter 60. Teil A. Verlag Chemie, Weinheim, 1955.

[102] P. J. Ding, W. A. Lanford, S. Hymes, and S. P. Murarka. Effects of the addition of small amounts of Al to copper: Corrosion resistivity, adhesion, morphology, and diffusion. *J. Appl. Phys.*, 75:3627–3631, 1994.

[103] H. K. Liou, J. S. Huang, and K. N. Tu. Oxidation of Cu and Cu_3Ge thin films. *J. Appl. Phys.*, 77:5443–5445, 1995.

[104] J. Li, J. W. Mayer, and E. G. Colgan. Oxidation and protection in copper and copper ally thin films. *J. Appl. Phys.*, 70:2820–2827, 1991.

[105] Gmelin. *Handbuch der Anorganischen Chemie.* Chapter 60. Teil D. Verlag Chemie, Weinheim, 1955.

[106] S.M. Sze. *Physics of Semiconductor Devices.* Wiley, New York, 1981.

[107] C. Durkan and M. E. Welland. Analysis of the failure mechanisms in electrically stressed gold nanowires. *Ultramicroscopy*, 84:125–133, 2000.

[108] Cell designed in the group of P. Apel in Dubna, 1999.

Acknowledgements

At this point I would like to sincerely thank all the people who have contributed to this work.

— Prof. Dr. R. Neumann for the possibility of working in his group and for supervising this thesis. Furthermore, for his support during my doctoral work as well as for the possibility to attend very interesting seminars and conferences.

— Dr. C. Trautmann for all her help and guidance during these years and also for her interest and kindness reading and correcting this and other manuscripts.

— Dr. D. Dobrev and Dr. J. Vetter for the introduction to the interesting topic of electrochemical deposition in etched ion track membranes. I would like to thank Dr. D. Dobrev for the helpful discussions and for his advices to the work, and Dr. J. Vetter for his contribution to the characterisation of the wires by transmission electron microscopy. Further, I thank Dr. R. Spohr for his advices and ideas.

— Dr. C. Trautmann, Dr. J. Vetter and A. Wolf, for the explanations about heavy ion irradiation at X0.

— Dr. I. Schuchert for the good times in the laboratory and many fruitful discussions. Also for her patience guiding a physicist to learn more about chemistry.

— Dr. Z. Siwy for her enthusiastic collaboration concerning the measurements on electrodeposition in single-pore membranes and for her friendly support.

— To all other members and ex-members of the Materials Research Group for all scientific and non-scientific discussions and for the good atmosphere during the work.

— I would like to express my thanks to Dr. J. Broetz from the Darmstadt University of Technology for the collaboration with the x-ray diffraction measurements, and to Dr. V. Buschmann and Dr. R. Scholz from the TU-Darmstadt and the Max-Planck Institute for Microstructure Physics in Halle, respectively, for their help with the TEM measurements.

— I also thank Prof. Dr. J. Kotthaus for the possibility to work for some weeks in his group at the Center for Nanoscience (CENS) at the Ludwig-Maximilians-University in Munich, Dr. R. Blick for encouraging the experiments and for his enthusiasm about making electrical contacts to the copper nanowires. Many thanks to E. Hoehberger for the long and interesting times in the clean-room and all explanations about lithographic processing, and C. Schaeflein for his participation in the measurements.

— A 1-year scholarship from the Deutscher Akademischer Austausch Dienst (DAAD) at the beginning of the thesis is gratefully acknowledged.

— I thank Paul and my mother for their friendship and support during these years.

THANKS!